Multiscale Computational Modeling of Brittle and Ductile Materials under Dynamic Loading

Karamnejad, Amin

DOI
10.4233/uuid:95a303ae-565c-41e9-91a7-0dea4d4207a1

Publication date
2016

Document Version
Final published version

Citation (APA)
Karamnejad, A. (2016). *Multiscale Computational Modeling of Brittle and Ductile Materials under Dynamic Loading*. [Dissertation (TU Delft), Delft University of Technology]. https://doi.org/10.4233/uuid:95a303ae-565c-41e9-91a7-0dea4d4207a1

Multiscale Computational Modeling of Brittle and Ductile Materials under Dynamic Loading

Amin KARAMNEJAD

Multiscale Computational Modeling of Brittle and Ductile Materials under Dynamic Loading

Proefschrift

ter verkrijging van de graad van doctor
aan de Technische Universiteit Delft,
op gezag van de Rector Magnificus prof. ir. K.C.A.M. Luyben,
voorzitter van het College voor Promoties,
in het openbaar te verdedigen op
donderdag 22 december 2016 om 12:30 uur

door

Amin KARAMNEJAD

Master in Mechanical Engineering,
Iran University of Science and Technology
geboren te Larestan, Iran

Dit proefschrift is goedgekeurd door de
Promotor: Prof. dr. ir. L. J. Sluys

Samenstelling promotiecommissie:

Rector Magnificus	voorzitter
Prof. dr. ir. L. J. Sluys	Technische Universiteit Delft, promotor

Onafhankelijke leden:

Prof. dr. ir. A. Scarpas	Technische Universiteit Delft
Prof. dr. ir. A. S. J. Suiker	Technische Universiteit Eindhoven
Prof. dr. ir. L. Noels	University of Liège, België
Dr. ir. J. Weerheijm	Technische Universiteit Delft
Dr. ir. F. P. van der Meer	Technische Universiteit Delft
Dr. ir. V. Kouznetsova	Technische Universiteit Eindhoven

ISBN 978-94-6186-760-5

To My Parents

Summary

Macroscopic behavior of heterogeneous materials depends on the behavior of their microstructures and the interaction between different phases. In such materials, the damaging process occurs at different length scales and time scales. Under dynamic loading conditions, rate dependency of the materials, large deformations and strains, micro inertia forces and wave reflection and refraction at the interfaces of different phases in the heterogeneous material are involved in the macroscopic response and should be taken into account.

The computational homogenization method enables to derive the overall behavior of heterogeneous materials from their local-scale response. In this method, a representative volume element (RVE) is assigned to a macroscopic material point and the constitutive law for the macroscopic model at that point is obtained by solving a boundary value problem for the RVE. However, the standard computational homogenization scheme cannot be used when strain localization occurs and does not account for dynamic effects at the local-scale. Furthermore, in the computational homogenization scheme, at each iteration, a boundary value problem should be solved for RVEs associated to the integration points of macroscopic elements which leads to high computational cost. When the problem is nonlinear (material and/or geometrical nonlinearities), the computational cost may become more than used for direct numerical simulation (DNS).

This study aims at developing computational and numerical homogenization schem- es which account for strain localization, dynamic effects at the local-scale and large deformations and strains. Furthermore, strategies are presented to decrease the computational cost while preserving accuracy. Different heterogeneous structures consisting of quasi-brittle materials, hyperelastic materials and polymer materials are studied and proper homogenization schemes are presented.

A computational homogenization scheme is developed to model failure in heterogeneous quasi-brittle materials under dynamic loading. In this scheme, the heterogeneous material with strain localization is replaced by a macro-scale model with a cohesive crack and a meso-scale model with diffuse damage. The constitutive law for the macroscopic bulk material is determined using standard computational homogenization. The cohesive law for the macroscopic crack is obtained using a continuous-discontinuous computational homogenization scheme which is based on a failure zone averaging technique. At the macro-scale a dynamic analysis is performed and the meso-scale model is solved as a static problem. The effect of the crack opening rate on the macroscopic cohesive law is taken into account by relating the material properties of the meso-scale model to the macro-crack opening rate. For the dynamic problems, it is shown that when the macroscopic length scale, which is related to the macroscopic wave length, is significantly larger than the meso-scale length scale, inertia forces at the meso-scale model are negligible. However, when the macroscopic characteristic length is comparable with the meso-scale length scale, inertia forces at the meso-scale result in wave dispersion and no longer can be neglected. In order to account for the inertia forces at the meso-scale model, a dispersion tensor is computed from the RVE problem with which the inertia forces at the meso-scale model can be obtained. The inertia forces at meso-scale model appear as additional body force in the macro-scale model.

A new computational homogenization scheme is developed to model heterogeneous incompressible hyperelastic materials undergoing large deformations. The model is bas- ed on a computational continua formulation which assumes that the macro-scale model consists of disjoint unit cells. Computational procedures to obtain the macroscopic quantities from the RVE problem solution are presented. It has been shown that the computational time for the proposed homogenization scheme is lower than for standard computational homogenization.

A numerical homogenization scheme is also developed to model glass particle-tough- ened polymer materials under dynamic loading. A constitutive law for the polymer materials is developed. It is assumed that the behavior of the heterogeneous material is governed by the same constitutive law as the polymer material with unknown material parameters. A homogenization scheme is presented to obtain the unknown material parameters by solving the RVE problem. The proposed homogenization scheme can be used after shear bands occur in the polymer matrix where the standard computational homogenization scheme is not valid.

The proposed homogenization schemes are validated against DNS and objectivity of the schemes with respect to the RVE size is demonstrated.

Samenvatting

Het macroscopisch gedrag van heterogene materialen is afhankelijk van het gedrag van hun microstructuren en de interactie tussen verschillende fasen. In dergelijke materialen vinden schade-processen plaats op verschillende lengte- en tijdschalen. Onder dynamische belastingcondities zijn de snelheidsafhankelijkheid van de materialen, grote deformaties, micro-traagheidskrachten en golfreflectie en -refractie op de grensvlakken tussen verschillende fasen in het heterogene materiaal van belang voor de macroscopische respons.

Numerieke homogenisatie is een methode om het gedrag van heterogene materialen af te leiden uit hun reactie op lokale schaal. Met deze methode wordt een representatief volume element (RVE) toegekend aan een macroscopisch materiaalpunt waarna de constitutieve vergelijking voor het macroscopisch model in dat punt wordt verkregen door een randvoorwaardeprobleem op te lossen voor het RVE. Echter, het gangbare numerieke homogenisatieschema kan niet worden gebruikt wanneer de deformatie lokaliseert en het schema houdt geen rekening met dynamische effecten op de lokale schaal. Daarnaast moet er bij iedere iteratie in het schema een randvoorwaardeprobleem worden opgelost voor ieder RVE dat geassocieerd is met een integratiepunt van een macroscopische element, wat leidt tot lange rekentijden. Wanneer het vraagstuk niet-lineair is (materiaal en/of geometrische niet-lineairiteiten) kan de rekentijd langer worden dan voor directe numerieke simulaties (DNS).

Deze studie heeft als doel het ontwikkelen van numerieke homogenisatieschema's die rekening houden met lokalisatie van deformatie, dynamische effecten op de lokale schaal en grote deformaties en rekken. Strategieën om de rekentijd te reduceren met behoud van nauwkeurigheid worden ook voorgesteld. Verschillende heterogene materiaalstructuren zoals quasi-brosse materialen, hyperelastische materialen en polymeren worden bestudeerd en geschikte homogenisatieschema's worden gepresenteerd.

Een numeriek homogenisatieschema is ontwikkeld om het falen te modelleren van heterogene quasi-brosse materialen onder dynamische belasting. In dit stelsel wordt het heterogene materiaal met gelokaliseerde deformatie vervangen door een macroscopisch model met een cohesieve scheur en een mesoscopisch model met diffuse schade. De constitutieve vergelijking voor het macroscopische materiaal wordt bepaald door gebruik te maken van standaard numerieke homogenisatie. De vergelijking voor de cohesieve scheur volgt uit een continue-discontinue numerieke homogenisatie welke gebas- eerd is op middeling van de gefaalde zone. Dynamische analyse wordt toegepast op de macroscopische schaal en het mesoscopisch model wordt opgelost als een statisch vraagstuk. Er wordt rekening gehouden met het effect van de snelheid van scheuropening op het macroscopische model door de materiaaleigenschappen van het mesoscopisch model te relateren

aan de snelheid van scheuropening op de macroscopische schaal. Voor dynamische vraagstukken wordt aangetoond dat wanneer de macroscopische lengte schaal, welke is gerelateerd aan de macroscopische golflengte, significant groter is dan de mesoscopische lengte schaal de traagheidskrachten op de mesoscopische schaal verwaarloosbaar zijn. Echter, wanneer de karakteristieke lengte van de macroscopische schaal vergelijkbaar is met de lengte van de mesoscopische schaal, resulteren traagheids- krachten op de mesoscopische schaal in een fenomeen zoals golfverstrooiing dat niet langer verwaarloosd kan worden. Om rekening te houden met de traagheidskrachten op het model van de mesoscopische schaal wordt een dispersietensor berekend met het RVE randvoorwaardeprobleem, waarmee de traagheidskrachten op het model van de mesoscopische schaal kunnen worden verkregen. De traagheidskrachten op de mesoscopische scha- al worden vertaald naar een additionele kracht in het model op de macroscopische schaal.

Een nieuw numeriek homogenisatieschema is ontwikkeld om heterogene onsamendrukbare hyp- erelastische materialen te modelleren welke grote deformaties ondergaan. Het model is gebaseerd op een numerieke continua formulering welke aanneemt dat het model van de macroscopische schaal bestaat uit disjuncte eenheidscellen. Numerieke procedures worden gepresenteerd om de macroscopische grootheden te verkrijgen uit de oplossing van het RVE vraagstuk. Er wordt aangetoond dat de rekentijd voor het voorgestelde homogenisatieschema korter is dan voor het standaard homogenisatieschema.

Een numeriek homogenisatieschema is ook ontwikkeld om glasdeeltjes-geharde polymeren te modelleren onder dynamische belasting. Een constitutieve vergelijking voor de polymeren is afgeleid. Er is aangenomen dat het gedrag van het heterogene materiaal wordt bepaald door dezelfde constitutieve vergelijking als het polymeer met onbekende materiaalgrootheden. Een homogenisatieschema is voorgesteld om de onbekende materiaalgrootheden te verkrijgen door middel van het oplossen van het RVE vraagstuk. Het voorgestelde homogenisatieschema kan worden gebruikt nadat deformatiezones optreden in de matrix bestaande uit het polymeer, waarvoor het standaard numerieke homogenisatieschema niet geldig is.

De voorgestelde homogenisatietechnieken zijn gevalideerd met DNS en de objectiviteit van de schema's ten opzichte van de grootte van het RVE is aangetoond.

Contents

1

Introduction

1.1. Multi-scale modeling of heterogeneous materials

Mixing different materials in order to obtain a better strength to weight ratio and desired material properties is being considered for the design of complex engineering structures for many years. These heterogeneous materials have vast applications in many industries including civil engineering, aerospace engineering, defense, biomechanical engineering and sports. For example, the reinforcement of automobile tires by adding particles and fibers or rubber/glass particle toughened polymer blends in defense and impact resistant structures.

Optimal design of these heterogeneous materials requires a good understanding of the global behavior of the material, the local behavior of each ingredient and the relation between the global and local responses. Heterogeneities of these materials give rise to difficulties in the design process. For instance, damage processes in heterogeneous materials occur at different spatial and temporal scales which makes the analysis more complex. When a structure is subjected to dynamic loading, for example in defense structures, geometrical nonlinearities due to large deformations and large strains, wave dispersion effects and complex damage mechanisms make the design procedure more difficult.

Modeling heterogeneous materials using a direct numerical simulation (DNS) in which detailed heterogeneities are modeled directly at the macro-scale may give accurate results but this method needs enormous computational efforts and is, in most cases, not practical.

Multi-scale methods provide proper tools to model heterogeneous materials. In the multi-scale methods, macroscopic behavior of the heterogeneous material is obtained by averaging the local-scale properties. Multi-scale methods include concurrent methods and homogenization-based methods. Concurrent methods can be divided into domain decomposition methods [14, 32, 42, 43, 46] and variational multi-scale methods [47]. Homogenization-based methods can be categorized into mathematical homogenization methods, numerical homogenization methods and computational homogenization methods. Mathematical homogenization methods are based on the mathematical asymptotic homogenization theory [52, 62]. In numerical homogenization methods which are also known as unit cell methods, a constitutive law is assumed for the macro-scale model and the unknown parameters for the constitutive law are determined by fitting the data obtained from a micro sample analysis [7, 67]. Unit cell methods have been extended for higher order continuum models by several authors, e.g. Forest et al. [25] has developed homogenization procedures for a periodic linear elastic Cosserat medium. In computational homogenization methods [20, 30, 75], a representative volume element (RVE) is associated to each material point. In this method, macroscopic deformations are used to prescribe boundary conditions on the RVEs and macroscopic behavior is obtained from solutions of the boundary value problems for the RVEs. A sample volume can be defined as an RVE if the homogenized properties do not change with the size of the sample volume.

In the computational homogenization scheme, the macroscopic stress field is assumed to be constant over the RVE. However, when strain localization occurs, for example in the form of shear bands or microcracks, this assumption is not valid. Figure 1.1 shows averaged stress versus averaged strain curves for heterogeneous samples with a localized deformation pattern for different sizes. The averaged quantities are computed over the whole sample domain. As it can be observed in figure 1.1, the results are similar in the linear regime but the results for the different sample sizes are different in the post-peak softening regime. This is due to the fact that when strain localization occurs, the localized area does not automatically scale with sample size and the homogenized properties change with the sample volume size [31]. Therefore, based on the aforementioned definition of an RVE, it can be concluded that RVE can only be defined for the linear and hardening regime.

Many researchers have worked on this issue to account for strain localization at the local-scale. A second-order computational homogenization scheme has been developed in [41] to model softening materials. In this method, the macroscopic deformation tensor and its gradients are used to prescribe the boundary conditions on the RVE. Oliver et. al. [56] have developed a multi-scale approach for modeling propagating fracture which is based on a continuum setting for the fracture at both scales and a standard format of the computational homogenization procedure. Introducing a failure zone averaging scheme, Nguyen et. al. [53] have defined an RVE for strain localization problems. Furthermore, a discontinuous computational homogenization scheme is developed in [54] based on the failure zone averaging scheme which can be used to model cohesive cracking in heterogeneous materials. In [55], a continuous-discontinuous computational homogenization scheme is developed in which the discontinuous scheme is used together with the standard homogenization scheme.

However, using computational homogenization methods may lead to high computational costs. In the computational homogenization method, when material behavior is linear, the RVE problem can be solved only once which makes

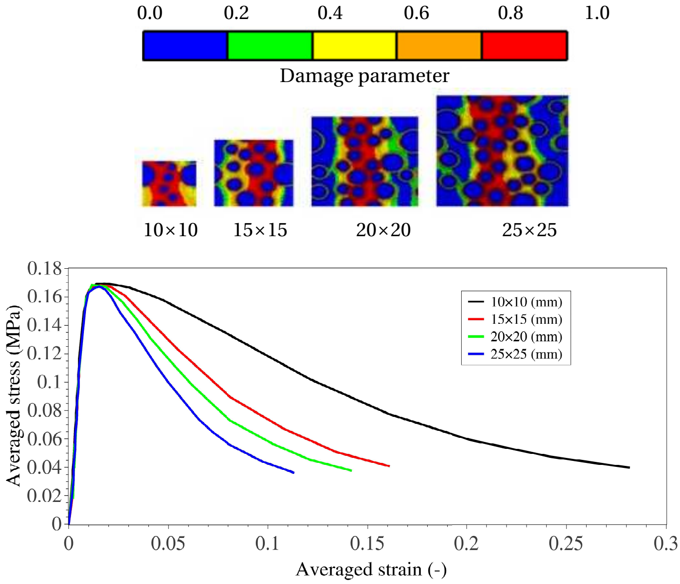

Figure 1.1: Averaged stress versus averaged strain for the localized heterogeneous samples with different sizes

the method computationally effective. However, when the constitutive relations of the micro-/meso-structures are nonlinear and history dependent, for each iteration of the macro-scale model problem solution, a boundary value problem needs to be solved for the RVEs associated to the macroscopic elements integration points. Therefore, in some cases, using the computational homogenization scheme may become computationally costlier than direct numerical simulations (DNS). This may become worse when geometrical nonlinearity is also included. One way to decrease the computational cost is to use the homogenization scheme only for the critical regions (for example regions where strain localization occurs). Parallel computing can also be used to reduce the computational time. Furthermore, model order reduction methods [8] can be applied to reduce the number of degrees of freedom for both macro-scale model and RVE problem. Using the model reduction method requires calculation of eigenvalues and eigenvectors for the problem which can be also computationally expensive. Alternatively, one can also decrease the number of RVE problems by choosing a coarse mesh for the macro-scale model. However, when the macro-scale model is subjected to large deformation gradients or the micro/meso structures are relatively large compared to the macroscopic model, using a standard first-order homogenization scheme with a very coarse macroscopic mesh, results in inaccurate solutions. Since in the first-order homogenization theory, the macroscopic strain is assumed to be constant over the RVE it yields inaccurate solutions in these cases. Higher order homogenization theory [41] and gradient elasticity models [2, 15, 29] can take micro/meso-model deformation gradients into account. However, higher-order homogenization methods introduce higher-order boundary conditions and gradient elasticity methods add additional degrees of freedom to the formulation. As a result, using these methods will increase the computational cost. Therefore, Fish and Kuznetsov [24] developed a computational continua model which considers the coarse-scale domain to consist of disjoint unions of computational unit cells. The advantages of this model are that it does not add higher-order boundary conditions and additional degrees of freedom to the problem.

For dynamic problems, local inertia effects may also affect the macroscopic response. Figure 1.2 depicts a heterogeneous body subjected to a pulse. Due to the heterogeneity of the structure, reflection and refraction of the wave between interfaces of different phases may occur which leads to wave dispersion. In a multi-scale model, dynamic effects at the local-scale should be taken into account in order to model these dispersion effects. On the other hand, performing a dynamic analysis for the RVE problem causes spurious wave reflections at the RVE boundaries (figure 1.2). This makes the multi-scale modeling of dynamic problems considerably more complex.

Multi-scale modeling for wave propagation problems is studied by many researchers. A two-field multi-body method is developed by Perales et. al. [58] to obtain fracture properties of heterogeneous materials under dynamic loading. Souza et. al. [70, 71, 73] have developed a multi-scale model for heterogeneous viscoelastic materials by considering the same form of constitutive equations at the local-scale model and the global-scale model. Furthermore, they have developed a scheme for transition of the micro-crack to the macro-crack in which the eXtended Finite Element Method (XFEM) [50] is used at the global-scale to model macro cracking and the cohesive zone method is used at the local-scale for modeling micro cracks [72]. Pham et. al. [59] have developed a transient computational homogenization scheme by enriching description of the micro–macro kinematics and a generalized Hill–Mandel condition to ensure a consistent solution of the balance of linear momentum at both scales. Wave dispersion phenomena can be modeled using gradient elasticity models [2, 15, 29] in which the classical equations of elasticity are extended by adding higher order spatial derivatives of strain, stress and/or acceleration. However, these models introduce additional length scales in the constitutive equations which need to be identified. Another drawback of the gradient elasticity models is that they cannot easily be implemented in the standard finite element formulation and a C^1 continuity formulation is required. Wang and Sun [77] have developed a model including micro-inertia for heterogeneous materials under dynamic loading. Using dynamic equations of motion at the local-scale together with the averaging theorem for the local-scale stress and strain and local-scale work, the macroscopic strain energy and macroscopic kinetic energy are obtained which contain micro-inertia terms. The Hamilton's principle is used to obtain macroscopic equations of motion in which micro-inertia appears as effective extra body forces. Dispersion effects are modeled using a higher order homogenization method in [12, 21, 22]. Fish [23] developed a multi-scale scheme in which the asymptotic expansions of displacement, inertia, and weight functions are used to derive global-scale and local-scale equations of motion. Local-scale inertia effects are taken into account as an inertia induced eigen strain. Local-scale inertia effects lead to additional body forces at the global-scale which is represented using a so-called dispersion tensor. This dispersive model is compatible with standard C^0 continuity finite element formulations and higher order boundary conditions are not required.

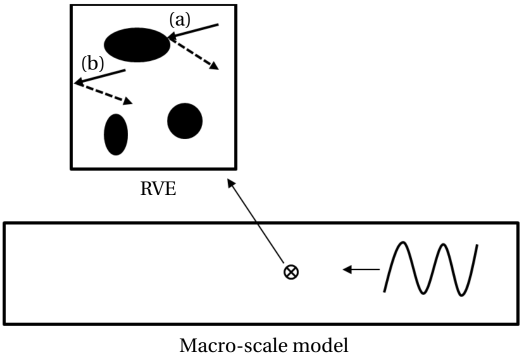

Figure 1.2: Wave propagation in the multi-scale model: (a) wave reflection at interface of different materials causes wave dispersion, (b) spurious reflections from the RVE boundaries

As mentioned before, under dynamic loading condition, structures can also undergo large deformations and strains. Most of the works using multi-scale methods, consider small deformations at both macro-scale and micro-/meso-scale. There are also a number of works in which large deformations and large strains are investigated. Bolzon et. al. [9] and Moraleda et. al. [51] presented a hyperelastic constitutive model for compressible materials under large deformations by homogenizing the strain energy density function of periodic porous elastomers. Ponte Castañeda and Tiberio [60] presented a second-order homogenization approach for particle reinforced rubbers. The implementation of a 3D numerical model using this second-order homogenization method is performed by Bouchart et. al. [10]. Yvonnet et. al. [78] developed a computational homogenization scheme to calculate heterogeneous hyperelastic materials which use a database of the effective strain energy density function. Each value of the database is computed by solving a boundary value problem for the RVE and a continuous potential is obtained using an interpolation scheme during solving the macro-scale model.

According to the above discussion, a multi-scale model for heterogeneous materials under dynamic loading should account for strain localization, dynamic effects at the local-scale and large deformations and strains. The computational cost of the multi-scale scheme is also a challenging issue that should be considered. Developing comprehensive multi-scale methods which consider these issues is the aim of this study.

1.2. Scope and outline

In this study multi-scale methods are developed to model ductile and brittle heterogeneous materials under dynamic loading. The multi-scale methods developed in the manuscript are based on computational homogenization and numerical homogenization methods. A wide range of materials are considered including quasi-brittle material (concrete), rubber-like materials and polymer materials. In the homogenization schemes developed in this work, strain localization, rate dependency, dynamic effects at the local-scale and large deformations and strains are taken into account. Furthermore, the existence of RVEs, and the reduction of computational cost are discussed in this work. The remainder of this thesis is outlined as follows:

Chapter 2. In this chapter, an overview of the problem is given and the *standard computational homogenization* scheme and the *discontinuous computational homogenization* scheme for the static problem are described. These two methods will be further developed and extended for the dynamic problems in this thesis.

Chapter 3. The aim of this chapter is to extend the proposed discontinuous homogenization scheme by Nguyen et. al. [54] to wave propagation problems. Furthermore, rate effects are added to the model by relating the material properties of the RVE to the rate of the macroscopic crack opening. The scheme developed in this chapter is limited to dynamic problems where the macroscopic wave length is significantly larger than the local-scale length scale. In this case, the problem at the local-scale can be solved as a quasi-static problem. This is advantageous since as explained before considering inertia forces at the local-scale may cause two problems. Firstly, spurious reflections at the RVE's boundaries occur and secondly, it breaks down the assumption of a constant deformation gradient over the RVE volume.

Chapter 4. In this chapter, the computational homogenization scheme developed in chapter 3 is modified to capture the effect of meso-scale inertia forces for high frequency loading conditions using the dispersive model given in [23]. Furthermore, in order to determine the macro-crack initiation and direction, a loss of hyperbolicity criterion in the meso-scale model is used. The effect of dispersion on the damage evolution is taken into account via rate dependency of the cohesive law while the dispersion effects are assumed to be only a function of the meso-scale model configuration and material properties. Verification studies are performed using different numerical examples by comparing the dispersive multi-scale results with those of direct numerical simulations (DNS) and the existence of the RVE for the proposed dispersive multi-scale scheme is shown.

Chapter 5. In this chapter, based on a so-called computational continua formulation, a computational homogenization scheme is developed to model heterogeneous incompressible hyperelastic materials with relatively large RVEs undergoing large deformations and large strains. The computational procedures are developed and relations are derived from the RVE problem solution to obtain the macroscopic stress tensors and macroscopic tangent tensors used in the computational continua formulation. The computational issues for calculating the macroscopic tangent when the RVE undergoes large deformations are also discussed. The developed computational homogenization scheme is then verified through numerical examples for a heterogeneous elastic structure and a heterogeneous hyperelastic structure undergoing large deformations against the DNS model. The computational cost of the proposed scheme versus the standard homogenization scheme is also investigated.

Chapter 6. In this chapter, a numerical homogenization scheme is developed to model the glass particle-toughened polymer materials. A material model for the polymer is developed and verified against experimental results. In the homogenization scheme, it is assumed that the macroscopic behavior of the glass particle-polymer composite is governed by the same constitutive law as the polymer material with unknown material parameters. The unknown material parameters are then obtained from an RVE problem using the standard computational homogenization scheme. It is shown that unlike standard computational homogenization, the proposed method can be used after strain localization occurs in the material. Furthermore, initiation of crazing in the polymer material is investigated. The multi-scale model is then verified against direct numerical simulation (DNS) results.

Chapter 7. Conclusions and recommendations for future work are presented in this chapter.

2

Computational homogenization schemes for static problems

2.1. Multi-scale model

A heterogeneous body which consists of embedded stiff particles in the matrix is shown in figure 2.1. The body is subjected to a external force $\bar{\boldsymbol{t}}^{\zeta}$. As it is shown in figure 2.1, a localization band occurs in the matrix. In the multi-scale model, the heterogeneous body undergoing localized failure is replaced by a homogeneous macro-scale model with a discrete cohesive crack and a meso-scale model with a localization band of diffuse damage. In the present work, a cohesive crack in the macro-scale model is modeled using XFEM. In order to solve the macro-scale model problem, the constitutive law for the bulk material and the cohesive law for the cohesive crack are required to be determined. The constitutive law of the bulk material is obtained using a standard computational homogenization method by applying the macroscopic strain ($\boldsymbol{\varepsilon}^{\boldsymbol{M}}$) on the RVE boundary. By solving a boundary value problem for the RVE, the corresponding macroscopic stress ($\boldsymbol{\sigma}^{\boldsymbol{M}}$) and macroscopic tangent ($\boldsymbol{C}^{\boldsymbol{M}}$) can be computed. The cohesive law for the crack can be determined using a continuous-discontinuous computational homogenization method in which the macro-crack opening ($[\![\boldsymbol{u}]\!]^{M}$) is applied on the RVE for the integration points on the crack surface. The macroscopic traction ($\boldsymbol{t}^{\boldsymbol{M}}$) and the cohesive tangent ($\boldsymbol{T}^{\boldsymbol{M}}$) are calculated by solving an RVE problem.

In the following sections, the finite element formulations for the macro-scale model and the meso-scale model are derived and the procedures for determining the macroscopic properties from the meso-scale model are presented.

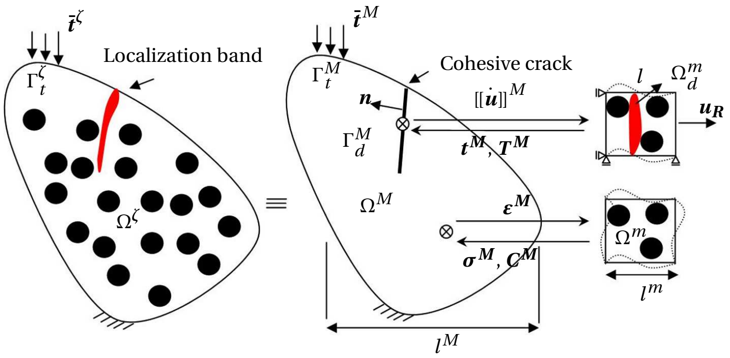

Heterogeneous body Macro-scale model Meso-scale model

Figure 2.1: Multi-scale scheme

2.2. Macro-scale model

The momentum equation for the heterogeneous body shown in figure 2.1 can be written as:

$$\frac{\partial \sigma_{ij}^{\zeta}}{\partial x_j^{\zeta}} = 0 \tag{2.1}$$

In the multi-scale scheme two spatial coordinates are introduced; macro-scale coordinates $\boldsymbol{x^M}$ and meso-scale coordinates $\boldsymbol{x^m}$ which are related via $\boldsymbol{x^m} = \frac{\boldsymbol{x^M}}{\zeta}$ with $\zeta \ll 1$. The displacement, strain and stress fields for the heterogeneous body can be written using asymptotic expansions as [23]:

$$u_i^{\zeta}(\boldsymbol{x^M}, \boldsymbol{x^m}, t) = u_i^{M}(\boldsymbol{x^M}, t) + \zeta u_i^{m}(\boldsymbol{x^M}, \boldsymbol{x^m}, t) + o(\zeta^2) \tag{2.2}$$

$$\varepsilon_{ij}^{\zeta}(\boldsymbol{x^M}, \boldsymbol{x^m}, t) = \varepsilon_{ij}^{m}(\boldsymbol{x^M}, \boldsymbol{x^m}, t) = \varepsilon_{ij}^{M}(\boldsymbol{x^M}, t) + u_{(i,x_j^m)}^{m}(\boldsymbol{x^M}, \boldsymbol{x^m}, t) \tag{2.3}$$

$$\sigma_{ij}^{\zeta}(\boldsymbol{x^M}, \boldsymbol{x^m}, t) = \sigma_{ij}^{m}(\boldsymbol{x^M}, \boldsymbol{x^m}, t) = \sigma_{ij}^{M}(\boldsymbol{x^M}, t) + \tilde{\sigma}_{ij}(\boldsymbol{x^M}, \boldsymbol{x^m}, t) \tag{2.4}$$

where ζ, M and m superscripts denote the heterogeneous model, macro-scale model and the meso-scale model quantities, respectively. $\boldsymbol{x}^{\square}$, $u_i^{\square}$, $\varepsilon_{ij}^{\square}$ and $\sigma_{ij}^{\square}$ are position vector, displacement vector, strain tensor and stress tensor, respectively. $\tilde{\sigma}_{ij}$ is the meso-scale stress perturbation. ζ is the ratio of the meso-model characteristic length to the macro-model characteristic length (figure 2.1). The derivative used in (2.3) is defined as $A_{(i,x_j^m)} = \frac{1}{2}\left(\frac{\partial A_i}{\partial x_j^m} + \frac{\partial A_j}{\partial x_i^m}\right)$.

Macroscopic strain/stress can be related to the meso-scale strain/stress fields via:

$$\boldsymbol{\varepsilon^M} = \frac{1}{|\Omega^m|}\int_{\Omega^m} \boldsymbol{\varepsilon^m}\, d\Omega^m \tag{2.5}$$

$$\boldsymbol{\sigma}^{\boldsymbol{M}} = \frac{1}{|\Omega^m|}\int_{\Omega^m} \boldsymbol{\sigma}^{\boldsymbol{m}} d\Omega^m \tag{2.6}$$

Energy consistency in transition of scales is satisfied by the Hill-Mandel principle [34] which states that the macroscopic work rate must be equal to the volume average of local-scale work rate over the RVE, according to:

$$\boldsymbol{\sigma}^M : \dot{\boldsymbol{\varepsilon}}^M = \frac{1}{|\Omega^m|}\int_{\Omega^m} \boldsymbol{\sigma}^m : \dot{\boldsymbol{\varepsilon}}^m d\Omega^m \tag{2.7}$$

Inserting equations (2.2)-(2.4) into the heterogeneous model momentum equation (2.1) and using averaging equations (2.5) and (2.6), the equation of motion for the bulk domain of the macro-scale model can be derived as:

$$\frac{\partial \sigma^M_{ij}}{\partial x^M_j} = 0 \quad \text{on} \quad \Omega^M \setminus \Gamma^M_d \tag{2.8}$$

The bulk material macro-stress can be computed via:

$$\dot{\boldsymbol{\sigma}}^{\boldsymbol{M}} = \boldsymbol{C}^{\boldsymbol{M}} : \dot{\boldsymbol{\varepsilon}}^{\boldsymbol{M}} \tag{2.9}$$

The fourth-order tensor $\boldsymbol{C}^{\boldsymbol{M}}$ is the bulk homogenized tensor which can be computed using a homogenization technique. The boundary condition for the crack surface reads:

$$\boldsymbol{n}\cdot\boldsymbol{\sigma}^{\boldsymbol{M}}{}_{+} = \boldsymbol{n}\cdot\boldsymbol{\sigma}^{\boldsymbol{M}}{}_{-} = \boldsymbol{t}^{\boldsymbol{M}} \quad \text{on} \quad \Gamma^M_d \tag{2.10}$$

where $\boldsymbol{n}$ and $\boldsymbol{t}^{\boldsymbol{M}}$ are the outward normal to the crack surface and the macroscopic traction, respectively. The cohesive law for the cohesive crack can be written in the rate form as:

$$\dot{\boldsymbol{t}}^{\boldsymbol{M}} = \boldsymbol{T}^{\boldsymbol{M}}\cdot [[\dot{\boldsymbol{u}}]]^{\boldsymbol{M}} \tag{2.11}$$

where $[[\boldsymbol{u}]]^{\boldsymbol{M}}$ and $\boldsymbol{T}^{\boldsymbol{M}}$ are the displacement jump for the macro crack and the macro cohesive tangent, respectively. In the finite element method, the phantom node method is used to model the strong discontinuity in which the cracked element is modeled using two overlapping elements[49, 69]. The weak form of the problem can be written as:

$$\int_{\Gamma^M_t} \delta\boldsymbol{u}.\bar{\boldsymbol{t}}^M d\Gamma^M_t - \int_{\Omega^M} \nabla^s\delta\boldsymbol{u} : \boldsymbol{\sigma}^M d\Omega^M - \int_{\Gamma^M_d} \delta[[\boldsymbol{u}]]^M.\boldsymbol{t}^M d\Gamma^M_d = 0 \tag{2.12}$$

The discretized equations for the macro-scale model can be written as:

$$\boldsymbol{f}^{\boldsymbol{M}}_{\boldsymbol{ext}} - (\boldsymbol{f}^{\boldsymbol{M}}_{\boldsymbol{bulk}} + \boldsymbol{f}^{\boldsymbol{M}}_{\boldsymbol{coh}}) = 0 \tag{2.13}$$

where $\boldsymbol{f}^{\boldsymbol{M}}_{\boldsymbol{ext}}$, $\boldsymbol{f}^{\boldsymbol{M}}_{\boldsymbol{bulk}}$ and $\boldsymbol{f}^{\boldsymbol{M}}_{\boldsymbol{coh}}$ are the external force vector, the bulk force vector and the cohesive force vector, respectively. Internal force vectors can be obtained via

$$\boldsymbol{f}^{\boldsymbol{M}}_{\boldsymbol{bulk}} = \int_{\Omega^M} \boldsymbol{B}^T \boldsymbol{\sigma}^{\boldsymbol{M}} d\Omega^M \tag{2.14a}$$

$$\boldsymbol{f^M_{coh}} = \int_{\Gamma^M_d} \boldsymbol{N}^T \boldsymbol{t^M} d\Gamma^M \tag{2.14b}$$

in which $\boldsymbol{N}$ and $\boldsymbol{B}$ are the matrix of nodal shape functions and the matrix of derivatives of the shape functions, respectively.

2.3. Meso-scale problem

The momentum equation for the meso-scale problem can be written similar to the macro-scale problem as:

$$\frac{\partial \sigma^m_{ij}}{\partial x^m_j} = 0 \tag{2.15}$$

The rate form of the constitutive law for the meso-scale problem reads:

$$\boldsymbol{\dot{\sigma}^m} = \boldsymbol{C^m} : \boldsymbol{\dot{\varepsilon}^m} \tag{2.16}$$

where the fourth-order tensor $\boldsymbol{C^m}$ is the meso-scale model tangent module which depends on the material model. The discretized form of equation (2.15) reads:

$$\boldsymbol{f^m_{int}} = \boldsymbol{f^m_{ext}} \tag{2.17}$$

in which

$$\boldsymbol{f^m_{int}} = \int_{\Omega^m} \boldsymbol{B}^T \boldsymbol{\sigma^m} d\Omega^m \tag{2.18}$$

2.4. Macro-meso transition

In order to solve the discretized equation (2.13), one needs to find the macroscopic constitutive law for the bulk material (equation (2.9)) and the macroscopic cohesive law for the macro crack (equation (2.11)) from the meso-scale model. In section (2.4.1) the standard computational homogenization is presented which can be used to obtain the bulk material macroscopic constitutive law. The continuous-discontinuous computational homogenization scheme is explained in section (2.4.2) which is used to obtain the cohesive law for the cohesive crack.

2.4.1. Standard computational homogenization scheme for bulk material

Before strain localization occurs in the bulk material, the macro strain $\boldsymbol{\varepsilon^M}$ can be transformed on the RVE boundary as (for periodic boundary condition) [40]:

$$\boldsymbol{u_i} = \boldsymbol{H_i}^T \boldsymbol{\varepsilon^M} \qquad i = 1, 2, 4 \tag{2.19}$$

where $\boldsymbol{u_i}$ is the displacement of the RVE's three controlling nodes shown in figure 2.2 and $\boldsymbol{H_i}$ is:

$$\boldsymbol{H_i} = \begin{bmatrix} x_i & 0 \\ 0 & y_i \\ \frac{y_i}{2} & \frac{x_i}{2} \end{bmatrix} \tag{2.20}$$

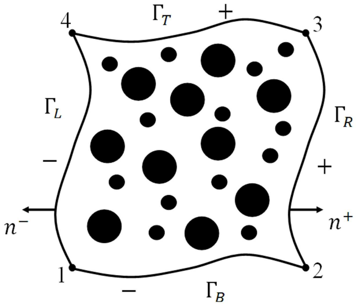

Figure 2.2: Periodic representative volume element

The macroscopic stress as the volume average of meso-scale stress can be obtained via

$$\boldsymbol{\sigma}^{\boldsymbol{M}} = \frac{1}{|\Omega^m|}\begin{bmatrix}\boldsymbol{H}_1 & \boldsymbol{H}_2 & \boldsymbol{H}_4\end{bmatrix}\begin{bmatrix}\boldsymbol{f}_1\\ \boldsymbol{f}_2\\ \boldsymbol{f}_4\end{bmatrix} \tag{2.21}$$

where $\boldsymbol{f_i}$ is the force vector at the controlling nodes.

At the converged state the linearized form of equation (2.17) for the meso-scale model problem is written as $\boldsymbol{K}^m\delta\boldsymbol{u}^m = \delta\boldsymbol{f}^m$ from which the macroscopic tangent moduli, $\boldsymbol{C^M}$, can be obtained via

$$\boldsymbol{C^M} = \begin{bmatrix}\boldsymbol{H}_1 & \boldsymbol{H}_2 & \boldsymbol{H}_4\end{bmatrix}(\boldsymbol{K^m_{bb}} - \boldsymbol{K^m_{ba}}(\boldsymbol{K^m_{aa}})^{-1}\boldsymbol{K^m_{ab}})\begin{bmatrix}\boldsymbol{H}_1\\ \boldsymbol{H}_2\\ \boldsymbol{H}_4\end{bmatrix} \tag{2.22}$$

in which subscript b denotes controlling nodes (three corner nodes) degrees of freedom and subscript a represents the other nodes' DOFs.

2.4.2. Continuous-discontinuous computational homogenization scheme for the macro crack

When localization is detected in the RVE associated to a certain integration point of the macro-scale model, a macrocrack is inserted in that point. In the cracked element, the bulk integration points are disconnected from the meso-scale model. In the continuous-discontinuous scheme, the macro stress can be obtained from:

$$\boldsymbol{\sigma^M} = \boldsymbol{C^M_{un}} : \boldsymbol{\varepsilon^M} \tag{2.23}$$

where $\boldsymbol{C^M_{un}}$ is a secant unloading tensor which can be computed by unloading the localized RVE and computing the homogenized tangent from equation (2.22). To each integration point on the crack surface, an RVE with boundary conditions shown in figure 2.1 is allocated. The macro-meso transition equation is given as [55]:

$$\boldsymbol{u}_R(\boldsymbol{u^m}) = (w - l(\boldsymbol{u^m}))\boldsymbol{Ct^M} + [[\boldsymbol{u}]]^{\boldsymbol{M}} + \boldsymbol{u^0_{dam}} \tag{2.24}$$

where $\boldsymbol{u}_R$ is the total displacement at the right edge of the RVE. The first term in the right-hand-side of the equation represents the linear displacement and $\boldsymbol{u^0_{dam}}$ is the compatibility displacement. w and l denote the width of the RVE and the averaged width of the localization band, respectively (figure 2.1). Matrix $\boldsymbol{C}$ is obtained as:

$$\boldsymbol{C} = \boldsymbol{\Delta^T} \Re^{-\boldsymbol{1}} \boldsymbol{\Delta}, \quad \boldsymbol{\Delta} = \begin{bmatrix} 1 & 0 \\ 0 & 0 \\ 0 & 1 \end{bmatrix} \tag{2.25}$$

$\Re$ can be computed using the cloning operation as follows: when localization is detected in the RVE associated to the bulk integration point, the average stress , $\boldsymbol{\sigma^M_{loc}}$, is calculated from equation (2.21). The traction can be obtained using $\boldsymbol{t^M_{loc}} = \boldsymbol{\sigma^M_{loc}} \cdot \boldsymbol{n}$, where $\boldsymbol{n}$ is the normal vector of the macro-crack. The initial state of the RVE corresponding to the integration point on the crack surface is obtained as follows: The undeformed RVE with the boundary conditions shown in figure 2.1 is loaded to $\alpha \boldsymbol{t}^M_{loc}$. Then the deformed RVE is temporarily unloaded. At the converged state of this unloading step the secant matrix $\Re$ can be computed using equation (2.22). Taking α=1.0 shows divergence of the solution. Here $\alpha = 0.99$ is used.

The failure zone averaging scheme is used to compute the averaged quantities for the meso-scale model. The averaged quantities are calculated over the active damaged zone Ω^m_d. The meso-scale quantities can be defined through:

$$l = \frac{|\,\Omega^m_d\,|}{h}, \quad \boldsymbol{\varepsilon^m}_{dam} = \frac{1}{|\,\Omega^m_d\,|} \int_{\Omega^m_d} \boldsymbol{\varepsilon^m} \, d\Omega^m, \quad \boldsymbol{u^m_{dam}} = \boldsymbol{\varepsilon^m}_{dam} \cdot (l\boldsymbol{n}) \tag{2.26}$$

h and $\boldsymbol{n}$ are the height of the RVE and normal to the crack band, respectively. l is the width of the localization band. $\boldsymbol{u^0_{dam}}$ is calculated at the moment of crack initiation using above equations. In order to compute the macroscopic traction, $\boldsymbol{t^M}$, and the macroscopic cohesive tangent, $\boldsymbol{T^M}$, system of equations (2.17) and (2.24) are solved. Details on theoretical and computational aspects can be found in [54, 55].

3

A computational homogenization scheme for quasi-brittle heterogeneous materials under dynamic loading

3.1. Summary

[1] In this chapter, a multi-scale numerical approach for modeling cracking in heterogeneous quasi-brittle materials under dynamic loading is presented.

In the proposed model, a discontinuous crack model is used at macro-scale to simulate fracture and a gradient-enhanced damage model has been used at meso-scale to simulate diffuse damage. The traction-separation law for the cohesive zone model at macro-scale is obtained from the meso-scale through the discontinuous computational homogenization method. An implicit time integration is used to solve the dynamic problem at the macro-scale while the meso-scale model is solved as a quasi-static problem. The effect of crack opening rate on the macro cohesive law is taken into account by relating the material properties of the meso-scale model to the macro crack opening rate. The objectivity of the model response with respect to the representative volume element size is demonstrated for wave propagation problems. The model is verified by comparison with a direct numerical simulation.

---

[1] Based on reference [36]

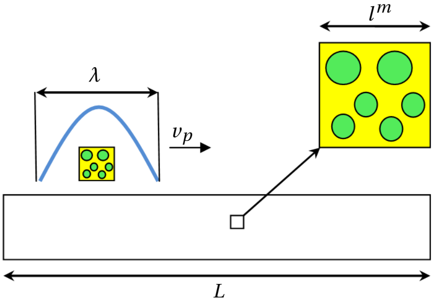

Figure 3.1: Wave propagation in a heterogeneous beam

3.2. Computational homogenization scheme for dynamic loading

To use computational homogenization theory, the problem must meet the following requirements. Firstly, the RVE should exist for the heterogeneous material. As it is noted in chapter 1, the RVE exists if an increase in size does not change homogenized properties and the sample is large enough so that the meso-/micro- structure randomness does not affect the homogenized properties. The second important issue in computational homogenization is the principle of separation of scales which indicates that the macroscopic characteristic length scale, l^M, which is either geometrical or related to the characteristic length of the phenomenon [3] is assumed to be much larger than the local-scale length, l^m (see figure 2.1).

Figure 3.1 depicts a wave propagating with wave speed v_p through a heterogeneous beam of length L. In wave propagation problems it can be shown that the macroscopic characteristic length, l^M, is related to the macro-scale wave length, λ, through $l^M = \frac{\lambda}{2\pi}$ [11]. In this case, the principle of separation of scales reads:

$$\delta = \frac{l_m}{l^M} = \frac{2\pi l^m}{\lambda} \ll 1 \tag{3.1}$$

Fish et. al. [21] showed that higher-order homogenization is required to model dispersion effects in wave propagation problems using a two-scale asymptotic expansion method. They demonstrated that in a dynamic problem, homogenized material properties obtained using the zero-order homogenization method is the same as in the statics. It is also concluded in [21] that for low values of δ ($\delta \leq 10^{-2} \Leftrightarrow 10^{-1}$), the classical zero-order homogenization gives proper results for dynamic problems.

In this chapter, problems with small values of δ are considered. Therefore, according to the aforementioned discussion, the structural response is obtained by solving the dynamic problem for the macro-scale model and for each time step of the macro-scale solution, the material response is obtained from a static analysis of the meso-scale problem.

3.2.1. Macro-scale model

The momentum equation for the heterogeneous body (figure 2.1) in a dynamic problem can be written as:

$$\frac{\partial \sigma_{ij}^{\zeta}}{\partial x_j^{\zeta}} = \rho^{\zeta}\, \ddot{u}_i^{\zeta} \tag{3.2}$$

in which ρ^{ζ} is the density of the heterogeneous body. The discretized equation (2.13) can be written for a dynamic problem as:

$$\boldsymbol{M^M} \boldsymbol{\ddot{u}^M} = \boldsymbol{f^M_{ext}} - (\boldsymbol{f^M_{bulk}} + \boldsymbol{f^M_{coh}}) \tag{3.3}$$

where $\boldsymbol{M^M}$ is the macro-scale model mass matrix and can be obtained via:

$$\boldsymbol{M^M} = \int_{\Omega^M} \boldsymbol{N}^T \rho^M \boldsymbol{N} d\Omega^M \tag{3.4}$$

in which ρ^M denotes the macro-scale model density and can be obtained from the meso-scale mass densities $\rho^m (=\rho^{\zeta})$ as:

$$\rho^M = \frac{1}{|\Omega^m|} \int_{\Omega^m} \rho^m d\Omega^m \tag{3.5}$$

An implicit Newmark time integration scheme is used to solve equation (3.3) in which consistent mass matrix is used. $\boldsymbol{f^M_{bulk}}$ and $\boldsymbol{f^M_{coh}}$ are computed from the meso-scale problem (RVE) using standard computational homogenization (2.4.1) and discontinuous computational homogenization (2.4.2) schemes, respectively.

3.2.2. Meso-scale model

In this chapter quasi-brittle materials (for example concrete) are analyzed. A gradient-enhanced damage model [57] is used to model the behavior of such materials. The stress-strain relation is given as [44]:

$$\boldsymbol{\sigma}^m = (1-\omega)\boldsymbol{C}^m : \boldsymbol{\varepsilon}^m \tag{3.6}$$

where ω is the scalar damage variable ($0 \le \omega \le 1$) and $\boldsymbol{C}^m$ is a fourth-order tensor which contains the elastic moduli. The damage evolution law is written as:

$$\omega = \begin{cases} 0 & \text{if } \kappa \le \kappa_I \\ 1 - \frac{\kappa}{\kappa_I}\left[1-\gamma+\gamma \exp\left(-\beta(\kappa-\kappa_I)\right)\right] & \text{if } \kappa > \kappa_I \end{cases} \tag{3.7}$$

where γ, β and κ_I denote residual stress, softening slope and damage threshold, respectively. κ is a scalar measure of the largest strain ever reached and is defined by loading function f as:

$$f = \bar{\varepsilon}_{eq} - \kappa \tag{3.8}$$

f and κ satisfy the Kuhn-Tucker conditions:

$$f \le 0, \quad \dot{\kappa} \ge 0, \quad f\dot{\kappa} = 0 \tag{3.9}$$

$\bar{\varepsilon}_{eq}$ is the nonlocal equivalent strain which is implicitly related to the local equivalent strain according to [57]:

$$\bar{\varepsilon}_{eq} - c\nabla^2\bar{\varepsilon}_{eq} = \varepsilon_{eq} \tag{3.10}$$

In this equation, c is defined as $c = \frac{1}{2}l_c^2$ and l_c represents the length scale. The local equivalent strain [48] is defined as:

$$\varepsilon_{eq} = \sqrt{\langle\varepsilon_1\rangle^2 + \langle\varepsilon_2\rangle^2} \tag{3.11}$$

where ε_i are the principle strains and $\langle x\rangle$ refers to the positive part of x.
At time step t and iteration i (in case of using implicit time integration for non-linear problems) in the macro-scale problem solution procedure, a quasi-static problem should be solved for RVEs associated to the integration points on the crack. The discrete system of equations for meso-scale model (RVE) can be written as:

$$^{(t,i)}\boldsymbol{f}^m_{ext} = {}^{(t,i)}\boldsymbol{f}^m_{int} \tag{3.12}$$

where $^{(t,i)}\boldsymbol{f}^m_{int}$ and $^{(t,i)}\boldsymbol{f}^{ext}_m$ are the internal force vector and the external force vector for the meso-scale problem (at time step t and iteration i of the macro-scale problem solution), respectively. By solving equation (3.12) one can find macroscopic quantities for the bulk ($\boldsymbol{\sigma}^M$ and $\boldsymbol{C}^M$) and the macro crack ($\boldsymbol{t}^M$ and $\boldsymbol{T}^M$) at time step t and iteration i for each integration point.

3.3. Wave propagation in a heterogeneous elastic beam

In this section, a heterogeneous 3-phase beam is considered which is subjected to a half sine impact pulse at one end (figure 3.2). Material properties for different phases are given in table 3.1. In this case, the beam remains elastic during the loading. Figure 3.3 depicts two different methods for modeling the problem. Figure 3.3 (a) shows a direct numerical simulation (DNS) in which all heterogeneities are directly modeled whereas figure 3.3 (b) illustrates the multi-scale model. Three phases including matrix, aggregates and interfacial transition zone (ITZ) are shown in yellow, green and blue, respectively. As shown in figure 3.3 (b), an RVE is associated to each integration point on the model. The dimensions of the RVE are 10 mm×10 mm which is 100 times smaller than the macro wave length which is 1000 mm.

The Newmark time integration scheme is used to solve the dynamic problem at the macro-scale. The time step for the macro-scale problem is 5.0e-4 (ms). For a certain time step, the macroscopic strain is transmitted to the RVE boundary condition using (2.19) and after solving the static boundary value problem (BVP) for the RVE, the homogenized stress and tangent moduli are calculated through (2.21) and (2.22). The tip displacement obtained from the DNS model and multi-scale model are shown in figure 3.4. Stress history curves for different points along the beam are given in figure 3.5 for DNS and multi-scale models. In this figure, curve number n shows average stress in x direction ($\overline{\sigma_x^M} = \frac{1}{|\Omega_n^M|}\int_{\Omega_n^M}\sigma_x^M d\Omega$) over a domain specified as $\{(x,y) \in \Omega_n^M \mid 20(n-1) \le x \le 20n, 0 \le y \le 20\}$ (in mm). Good

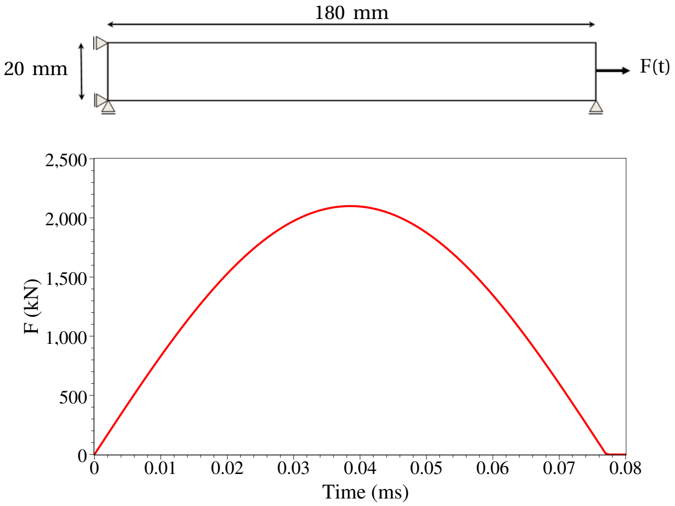

Figure 3.2: Heterogeneous elastic beam under dynamic loading

agreement can be observed between the results obtained from the DNS model and the multi-scale model.

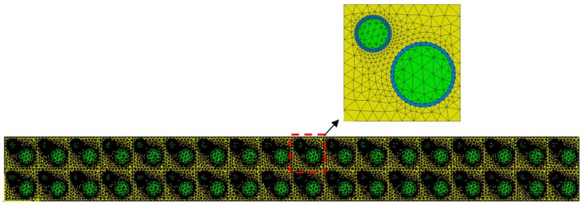

DNS Model

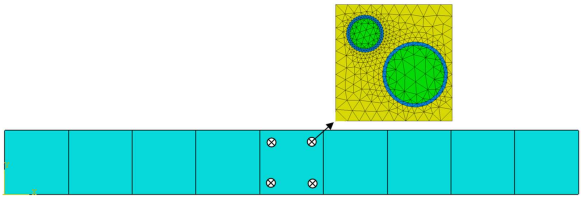

Multi-scale model

Figure 3.3: Direct numerical simulation and multi-scale model

Table 3.1: Material properties of different phases.

		Matrix	Aggregate	ITZ
E	(GPa)	12	80	7.2
ν	(-)	0.25	0.15	0.35
ρ	(kg/m^3)	1900	2400	1900

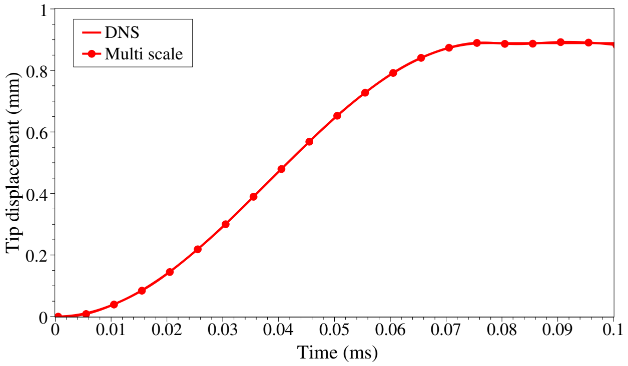

Figure 3.4: Tip displacement for DNS model and multi-scale model.

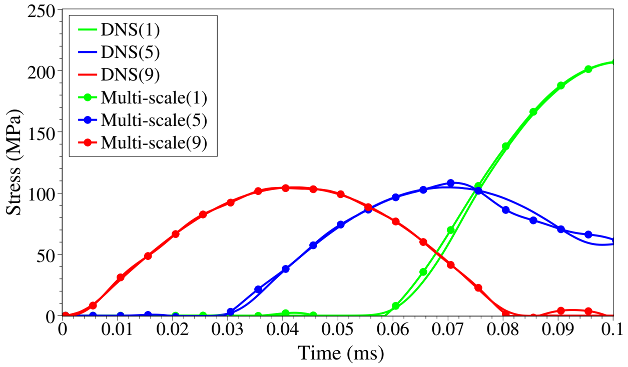

Figure 3.5: Stress history for DNS model and multi-scale model

3.4. Wave propagation in a heterogeneous beam with strain localization using rate-independent model

To study wave propagation in strain localization problems, a heterogeneous beam is subjected to a constant velocity at both ends (figure 3.6). Tensile waves propagate through the beam and after superposition of the waves at the center of the beam, the stress at this point exceeds the tensile strength and a crack initiates. Figure 3.7 shows the multi-scale model of the problem. Voided structures with different sizes are chosen as RVE for this problem. It should be mentioned that the multi-scale scheme is applied only on the crack and the bulk part is solved using the standard finite element method. The material properties for the RVE and the bulk material are given in table 3.2. A constant velocity equal to 0.3 (m/s) is applied at both ends of the beam. The time step is set to 3.2e-4 (ms)[2].

Parameter c in table 3.2 is related to the internal length-scale, l_c, which is linked to the microstructure of the material. This parameter can not be measured directly in the laboratory. The model needs to be calibrated for parameter c using experimental data. However, this is out of the scope of this work. In order to show the influence of parameter c, cohesive laws computed for c=0.01, 0.04 and 0.07 mm^2 using a 2.5 mm×2.5 mm RVE are given in figure 3.8. It can be observed that a decrease in parameter c leads to a more brittle response. This can be explained in figure 3.9 which shows the localization band at t=0.0128 (ms) in the RVE for various values of parameter c. The width of the damage band increases with increasing value of c and hence for a given traction more energy dissipates. The RVE size should be large enough to encompass the localization band, otherwise results become dependent on RVE size.

Cohesive laws computed from different RVE sizes, for c=0.04 mm^2, according to the failure zone averaging scheme, are illustrated in figure 3.10. It can be observed that the results are objective with respect to RVE size. In order to verify the multi-scale model, the results are compared with a DNS model. Figure 3.11 depicts the DNS model in which the material properties of the voided part and bulk part are similar to those of the RVE and the bulk part of the multi-scale model. Averaged stress over active damage zone (similar to the averaged strain in equation (2.26)) versus damage opening, $\boldsymbol{u}^m_{dam}$, for the DNS model and the multi-scale model are shown in figure 3.12 which shows good agreement. The difference between the results in the elastic branch is due to the fact that the mesostructure is not present in the multi-scale model before crack initiation and the averaged properties for the bulk part are not used before crack initiation. The RVE failure mode using the multi-scale model is also compared to that of the DNS model at time step t=0.0128 (ms) in figure 3.13. This comparison also demonstrates that the development of the damage zone for both models is similar.

For the problems described in this section, the computational time required for solving the DNS model until time t=0.001376 (ms) is 66.37 (s) while for the multi-scale models with RVE sizes 2.5 mm×2.5 mm, 5.0 mm×2.5 mm and 5.0 mm×5.0 mm are 29.2 (s), 65.42 (s) and 188.9 (s), respectively. The computational time for the multi-scale model with RVE size 5.0 mm×5.0 mm is larger than that of the DNS model but in this problem results obtained from an RVE size 2.5 mm×2.5 mm are accurate enough and as mentioned its computational time is less than half of that of the DNS model. The computational time for a multi-scale model depends on the size of the RVE and the mesh density of the RVE and the coarse

---

[2] The relevant time-scale can be calculated by dividing the crack tip speed by the cohesive zone length. The cohesive zone length can be obtained as: $l_{coh} = \frac{9\pi}{32}\frac{E}{1-\nu^2}\frac{G_c}{t^2_{max}}$ [79]. In this equation G_c and t_{max} are the fracture energy and maximum cohesive force, respectively. The limiting crack tip speed for mode I fracture is the Rayleigh wave speed which can be calculated as: $c_R = \left(\frac{0.862+1.14\nu}{1+\nu}\right)\sqrt{\frac{E}{2\rho(1+\nu)}}$ [26]. So the minimum time step can be found using: $\Delta t_{min} = \frac{l_{coh}}{c_R}$. The minimum time step for the problem given here is 6.2e-3 (ms). Due to rate dependency, an additional time-scale related to the crack opening rate is present which is generally smaller than the time scale linked to the crack tip speed. So, in order to ensure accuracy of the modeling, the time step is set to 3.2e-4 (ms).

model. However, one of the advantages the multi-scale method is that parallel computing methods can be used in this framework which decreases the computational time to a significant extent.

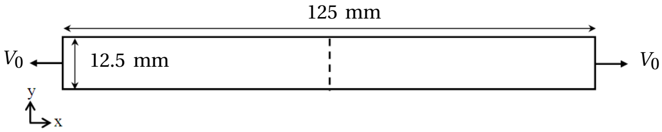

Figure 3.6: Heterogeneous beam under dynamic loading

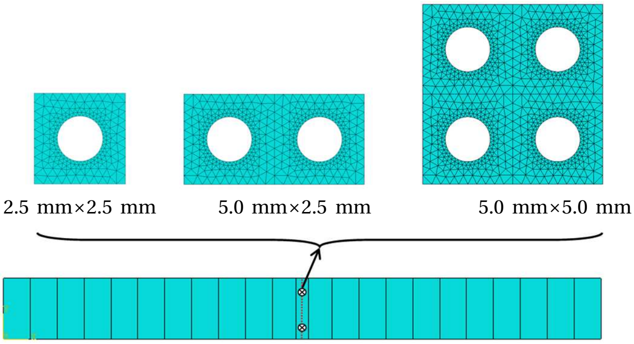

Figure 3.7: Multi-scale model and different RVE sizes

Table 3.2: Material properties for bulk material and RVE

		Bulk	RVE
E	(GPa)	50	50
ν	(-)	0.2	0.2
κ_I	(-)	0.3	8e-5
α	(-)	0.99	0.99
β	(-)	1500	1500
ρ	(kg/m^3)	1200	1200
c	(mm^2)	0.04	0.04

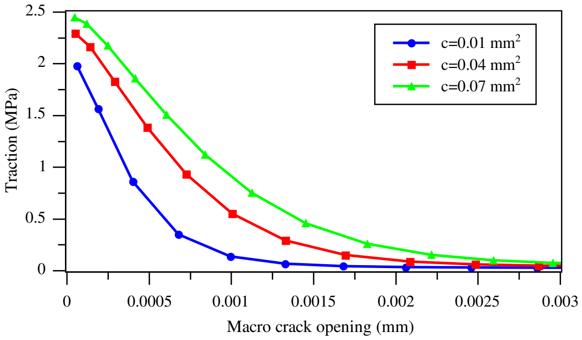

Figure 3.8: Computed cohesive law for different values of parameter c using a 2.5 mm×2.5 mm RVE

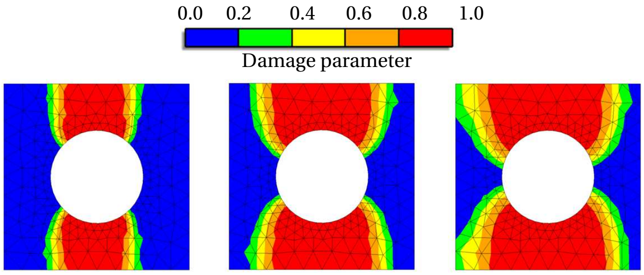

c=0.01 mm^2 c=0.04 mm^2 c=0.07 mm^2

Figure 3.9: The localization band for different values of parameter c

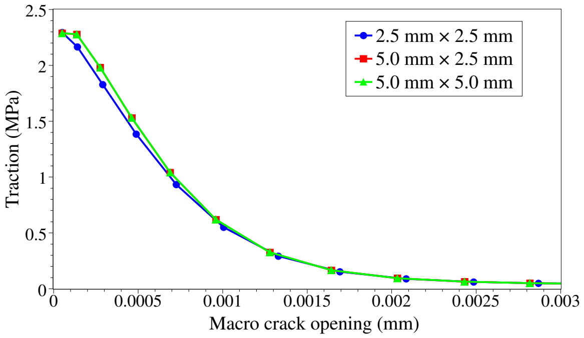

Figure 3.10: Computed cohesive law for different RVE sizes

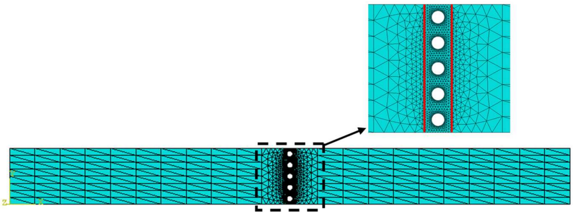

Figure 3.11: DNS model.

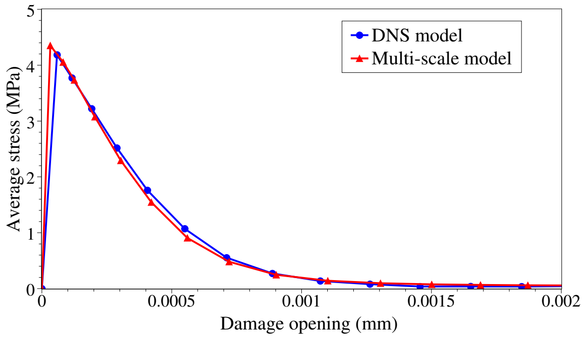

Figure 3.12: Averaged stress over failure zone versus damage opening for multi-scale model and DNS model

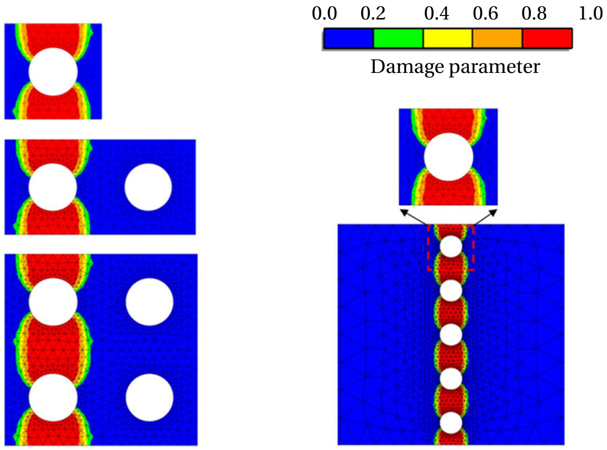

Multi-scale model DNS model

Figure 3.13: Comparison of failure modes for multi-scale model and DNS model

3.5. Rate-dependent cohesive law

There are two sources for rate dependency in concrete materials [13]: (i) the viscoelasticity of the material behavior in the bulk of the structure, (ii) the rate process of the bonds breakage in the fracture process zone. Both mechanisms are important for concrete but in high strain rate dynamic loading, the latter is the dominant mechanism which causes the cohesive law to be rate dependent. Bažant [5, 13], by considering fracture as a thermally activated phenomenon, derived a rate-dependent softening law. Here, we consider mode I fracture and for the traction in normal direction to the crack surface, the rate dependent softening law can be written as:

$$t_n^M\left([[u]]_n^M, [[\dot{u}]]_n^M\right) = \left[1 + c_1 \operatorname{asinh}\left(\frac{[[\dot{u}]]_n^M}{c_0}\right)\right] t_{0n}^M \tag{3.13}$$

where subscript n shows the direction to the crack surface, $[[\dot{u}]]_n^M$ denotes the macro crack opening rate and t_{0n}^M is the traction under static loading condition following from the RVE analysis. c_0 and c_1 are material parameters.

Here, we assume that, when a crack initiates, the damage threshold, κ_I, in the gradient damage model which is used for meso-scale model, is dependent on the crack opening rate through:

$$\kappa_I\left([[\dot{u}]]_n^M\right) = \left[1 + c_1 \operatorname{asinh}\left(\frac{[[\dot{u}]]_n^M}{c_0}\right)\right] \kappa_I^0 \tag{3.14}$$

in which κ_I^0 is the static damage threshold. In order to investigate this assumption, cohesive laws are computed for various values of κ_I (for problem shown in figure 3.6) which are obtained from equation (3.14) for $[[\dot{u}]]_n^M = 0.0, 0.25, 0.5, 1.0$ (m/s). Here, c_0 and c_1 are taken equal to 0.8 and 0.5, respectively [3]. In figure 3.14, these results are shown with solid lines. The dashed lines depict the static cohesive law, t_{0n}^M, multiplied by $\frac{\kappa_I\left([[\dot{u}]]_n^M\right)}{\kappa_I^0}$. From figure 3.14, it can be concluded that:

$$t_n^M\left([[u]]_n^M, [[\dot{u}]]_n^M\right) \simeq \frac{\kappa_I\left([[\dot{u}]]_n^M\right)}{\kappa_I^0} t_{0n}^M \quad \text{or} \quad \frac{t_n^M\left([[u]]_n^M, [[\dot{u}]]_n^M\right)}{t_{0n}^M} \simeq \frac{\kappa_I\left([[\dot{u}]]_n^M\right)}{\kappa_I^0} \tag{3.15}$$

The above relation shows that equations (3.13) and (3.14) are almost equivalent. So, in order to capture rate dependency effects in the macro-scale cohesive law, one can insert rate effects in the meso-scale model using equation (3.14). In the solution procedure, at time step t_i, for a certain crack in the macro-scale model, the crack opening rate is calculated and the damage threshold for the RVE corresponding to the integration points on this crack is updated using equation

---

[3] Parameters c_0 and c_1 can normally be found by fitting the model with experimental data. Due to lack of experimental data, these coefficients are chosen such that the effect of rate dependency on the cohesive law can be properly observed.

(3.14). To obtain a more accurate result, the problem is solved again for time step t_i with updated values for damage threshold, κ_I.

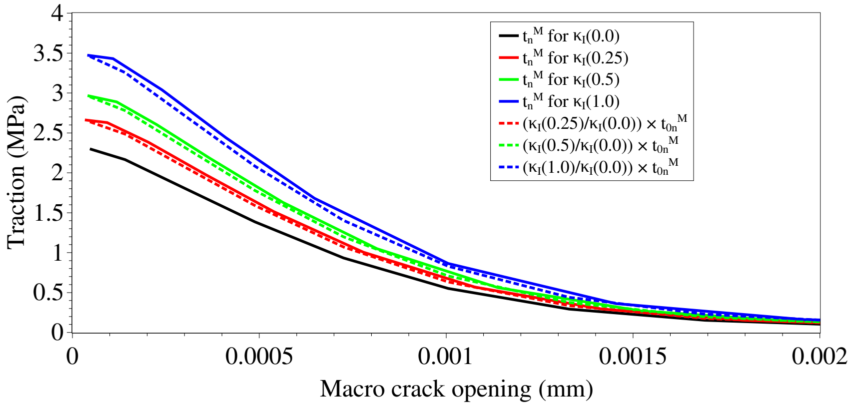

Figure 3.14: Traction-macro crack opening for various κ_I

3.6. Wave propagation in a heterogeneous beam with strain localization using rate-dependent model

The problem described in figure 3.6 is now considered for a crack with a rate-dependent cohesive law. The multi-scale problem is solved for different loading rates. Figure 3.15 illustrates the computed cohesive laws for various RVE sizes at different loading rates. As it can be observed in this figure, for a given crack opening, the traction increases with loading rate. It is also obvious that the obtained softening curves are objective with respect to the RVE size. The area under the traction-separation curve represents the dynamic fracture energy (G_c). Figure 3.16 shows the fracture energy versus applied velocity (V_0) for various RVE sizes. The dashed curve is an exponential function with format $y_0 + A\exp\left(-\frac{V_0}{y_1}\right)$ fitted to the data. Constant numbers y_0, y_1 and A are equal to 3.01, 0.45 and -1.35, respectively. It can be observed that the fracture energy increases with loading rate.

In order to verify the model, a DNS model is presented as before. In the DNS model, the relative velocity values between right-hand side and left-hand side of the voided part (parts shown with red lines in figure 3.11), after damage initiation, is taken as the crack opening rate. A comparison of crack opening rate in multi-scale model and DNS model for V_0=0.3 (m/s) is shown in figure 3.17. The averaged stress over the active damage zone versus damage opening is given in figure 3.18 for the multi-scale and the DNS model at various loading rates. It can be observed that for lower velocities the results are in good agreement. But, at higher loading rates, the curve obtained for the DNS model is above the multi-scale curve and the difference between these two curves increases with increasing loading rate. This difference stems from the inertia forces around the damaged zone in the DNS model. In the multi-scale model, as discussed before, the inertia forces at meso-scale are neglected in the present work and as a result the effects of inertia forces cannot be captured. Nevertheless, even at high rates, the multi-scale model is capable of properly calculating the material response. To illustrate this fact, the density of the voided part in the DNS model is assumed to be artificially small so that the inertia forces around the damaged zone are negligible. Averaged stress-damage opening curves are shown for V_0=1.0 (m/s) in figure 3.19. It can be observed that the curves for the DNS model and the multi-scale model lie on top of each other when the inertia forces are neglected in the voided part.

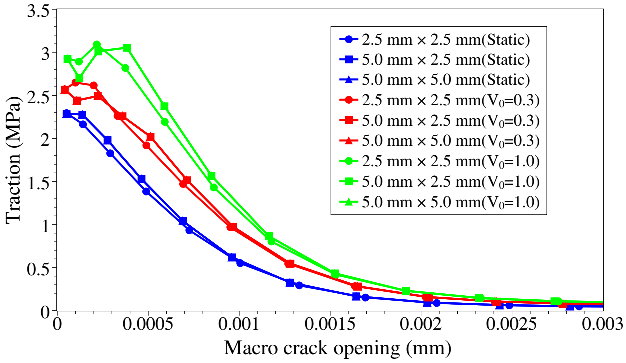

Figure 3.15: Computed cohesive laws for different RVE size at various loading rates

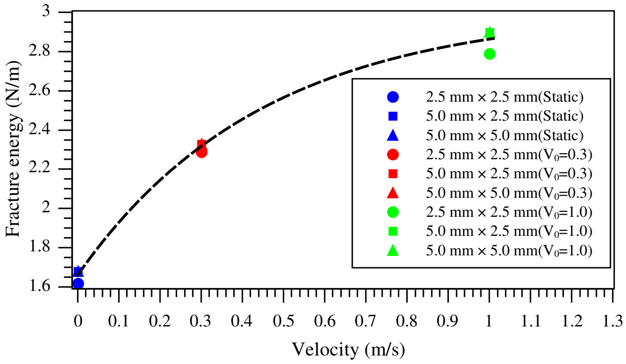

Figure 3.16: Fracture energy versus applied velocity for different RVE sizes

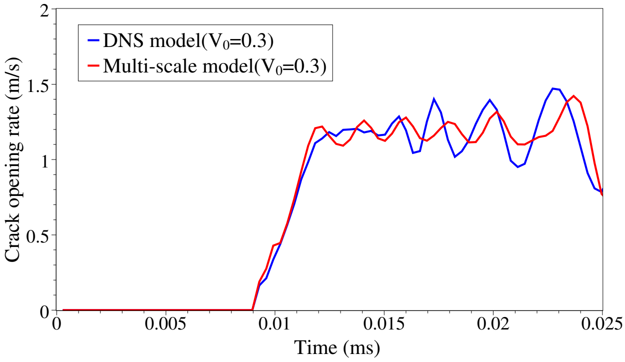

Figure 3.17: Crack opening rate at V_0=0.3 (m/s) for DNS and multi-scale models

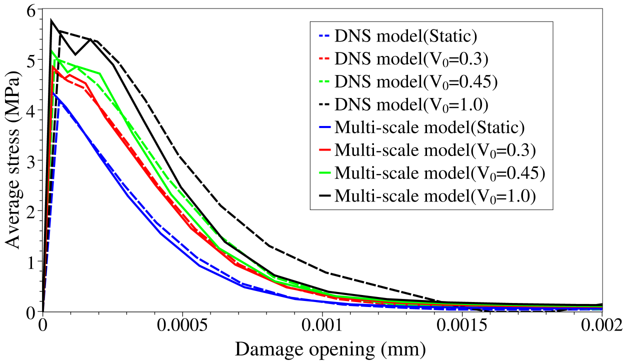

Figure 3.18: Averaged stress over the active damage zone versus damage opening for DNS model and multi-scale model at various loading rates

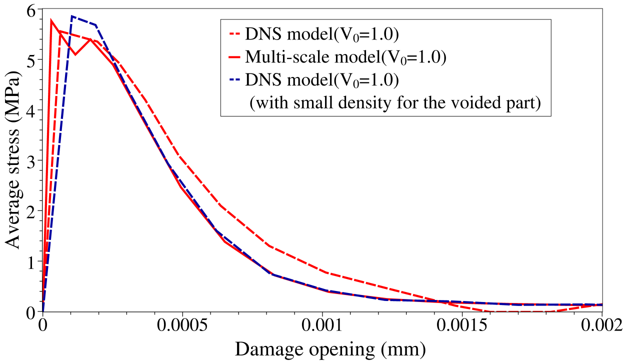

Figure 3.19: Inertia force effect on averaged stress-damage opening curve

3.7. Computation of rate dependent cohesive law for random heterogeneous meso-structure

In this section the model will be used to compute rate dependent cohesive laws for a heterogeneous three-phase material. Three phases include circular aggregates, ITZ and matrix. The size of aggregates is in the range of 1.25 (mm) to 2.5 (mm) and they are randomly distributed in the matrix. The width of the ITZ is 0.25 (mm) and the aggregate density is 45%. It is worth mentioning that in the gradient enhanced model used for the meso-scale model (section (3.2.2)), the normal component of the gradient of the nonlocal equivalent strain is zero on the external boundaries only. As a result, there exist non-local interactions at the interface of different phases. However, this is not a critical issue in the present work because the aggregates are elastic and the material properties used for matrix and ITZ are almost similar.

Table 3.3: Material properties for RVE

		Matrix	Aggregate	ITZ
E	(GPa)	25	30	20
ν	(-)	0.2	0.2	0.2
κ_I	(-)	7e-6	0.3	3e-6
α	(-)	0.99	0.99	0.99
β	(-)	1500	1500	1500
ρ	(kg/m^3)	1200	1200	1200
c	(mm^2)	0.02	0.02	0.02

The two-scale model is shown in figure 3.20. Loading and boundary conditions are the same as in the wave propagation problem described in figure 3.6. The length and width of the beam are 800 (mm) and 125 (mm), respectively. Material properties for the RVE are given in table 3.3. The macro-scale bulk material is an elastic material with Young's modulus of 30 (GPa) and Poisson ratio of 0.2. The material constants c_0 and c_1 from equation (3.14) are 0.2 and 1.0, respectively. The time step is 1.5e-3 (ms). Three different sizes for the RVE with random structure are used. Traction-separation (cohesive law) curves for the different RVE sizes at various loading rates are demonstrated in figure 3.21. It can be observed from figure 3.21 that the traction-separation curves are independent of RVE size. Slight differences observed between the results for various RVE sizes are due to the randomness of the structure and the fact that complex damaged areas are simply replaced by a rectangular damaged zone in this model (see equation (2.26)). Variation of the fracture energy with applied velocity is depicted in figure 3.22. It can be observed that the fracture energy is larger at higher loading rates. The constant numbers for the fitted curve are y_0=0.44, y_1=0.09 and A=-0.23. In order to show the rate effects on the failure evolution at meso-scale, the problem shown in figure 3.20 is solved for V_0=0.2 (m/s) using rate-dependent and rate-independent models. Failure zones for a 20 (mm)×20 (mm) RVE are illustrated in figure 3.23 when the macro-crack traction is equal to 4766.74 (Pa). It can be observed that the localized band width for results obtained with the rate-dependent model is larger than the width obtained with the rate-independent model. This is consistent with results reported by Zhou et. al. [79].

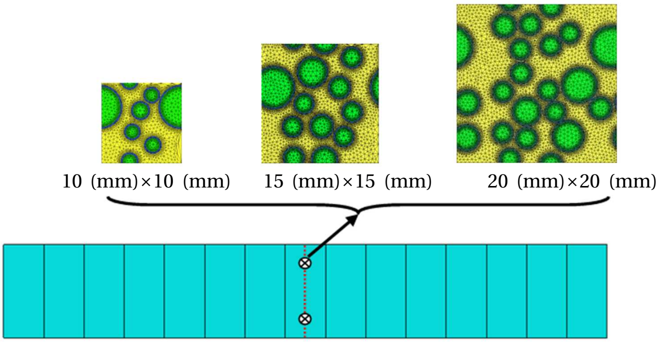

Figure 3.20: Multi-scale model

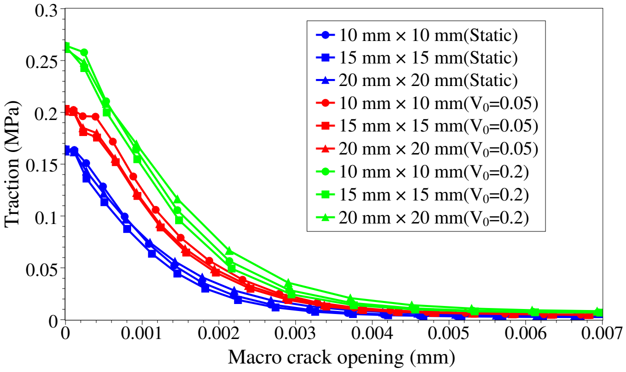

Figure 3.21: Cohesive law for various RVE size

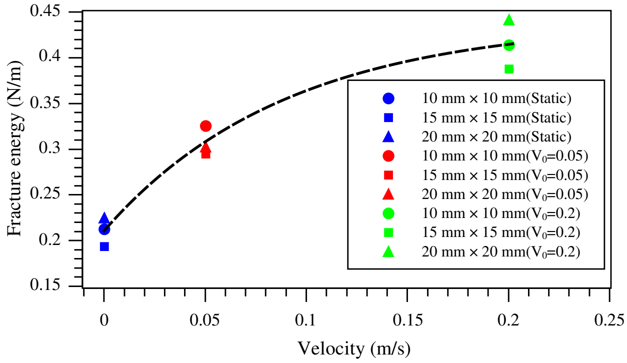

Figure 3.22: Fracture energy versus applied velocity for different RVE sizes

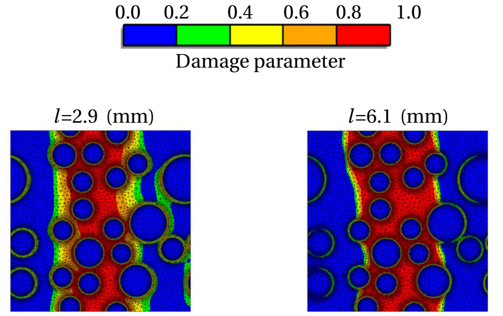

Rate-independent model

Rate-dependent model

Figure 3.23: Localized band width at meso-scale for rate-independent and rate-dependent models

3.8. Conclusion

In this chapter, the wave propagation problem in heterogeneous materials is studied using a multi-scale method. It is shown that when the length of the macroscopic propagating wave is significantly larger than the local-scale dimensions, one can perform a quasi-static analysis for the local-scale problem.

A two-scale rate-dependent crack model is developed based on the discontinuous computational homogenization scheme in which a failure zone averaging technique is used. Rate effects due to bond breakage in the fracture process zone are taken into account in the multi-scale model through the dependency of the material properties at the meso-scale model on the macrocrack opening rate.

The results obtained for various loading rates using different RVE sizes show that the model is objective with respect to the RVE size. Comparison of the multi-scale model results with those of a DNS model shows a good agreement which not only certifies the capability of the discontinuous homogenization method but also supports the idea of neglecting wave propagation at the local-scale problem.

4

A dispersive multi-scale crack model for quasi-brittle heterogeneous materials under impact loading

4.1. Summary

[1]A dispersive multi-scale model is presented to model failure in heterogeneous quasi-brittle materials under high frequency loading conditions. In the dispersive multi-scale model, the heterogeneous model undergoing localized failure is replaced by a homogeneous macro-scale model with a cohesive crack and a meso-scale model with diffuse damage. Each material point of the macro-scale model is linked to a heterogeneous meso-scale model. The macro-crack is modeled as a strong discontinuity and the gradient-enhanced damage model is used to model diffuse damage in the meso-scale model. The constitutive law for the bulk material is obtained from the meso-scale model analysis using a standard computational homogenization scheme. The cohesive law for the macro-crack is obtained using a continuous-discontinuous homogenization scheme which is based on a failure zone averaging technique. In the dispersive multi-scale model, at the macro-scale, a dynamic analysis is performed and the meso-scale model is solved as a quasi-static problem. The meso-scale inertia forces are taken into account via a dispersion tensor which only depends on the meso-scale model material properties and the heterogeneity of the material. The meso-scale inertia effects appear as additional body forces in the macro-scale model and cause dispersion of the propagating wave. The effect of dispersion on the cohesive cracking is captured via a rate dependent cohesive law. The dispersive multi-scale model

---

[1] Based on references [37, 38]

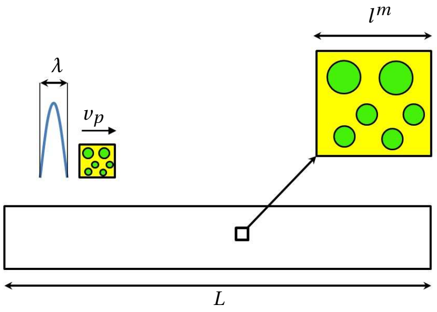

Figure 4.1: Wave propagation in a heterogeneous beam

is verified against a direct numerical simulation and the objectivity of the scheme with respect to the representative volume element size is shown.

4.2. Dispersive Multi-scale model for high frequency loading

In chapter 3, the dynamic problems in which the macroscopic wave length is significantly larger than meso-scale model is considered and it is shown than in such cases the meso-scale problem can be solved as a static problem. This chapter focuses on the dynamic problems in which the macro-scale wave length is comparable with the size of the meso-scale model. Figure 4.1 shows a wave propagating with wave speed v_p through a heterogeneous beam of length L. Unlike the problem shown in figure 3.1 in chapter 3, the macroscopic characteristic length l^M (see section (3.2)) is comparable with the meso-scale model length l^m. In this case equation (3.1) rewrites as:

$$\delta = \frac{l_m}{l^M} = \frac{2\pi l^m}{\lambda} \geq 1 \tag{4.1}$$

Similar to the wave propagation problem in chapter 3, the macro-scale model is solved as a dynamic problem while the meso-scale problems are solved as quasi-static problems. However, when $\delta \geq 1$, the dispersion effects cannot be neglected but since the meso-scale model is being solved statically, wave dispersion which is caused by the meso-scale inertia forces cannot be modeled. In order to model the effect of the meso-scale inertia forces, a dispersion tensor $\boldsymbol{D}$, which can be computed from the meso-scale model is presented.

4.2.1. Inclusion of the meso-scale model inertia forces in the macro-scale model

The inertia force for the heterogeneous body (figure 2.1) can be written as:

$$\rho^{\zeta}\ddot{u}_i^{\zeta}(\boldsymbol{x^M},\boldsymbol{x^m},t) = \rho^M \ddot{u}_i^M(\boldsymbol{x^M},t) + \zeta\rho^m \ddot{u}_i^m(\boldsymbol{x^M},\boldsymbol{x^m},t) \tag{4.2}$$

where $\ddot{u}_i^{\square}$ is acceleration vector and as described in chapter 2, ζ, M and m superscripts denote the heterogeneous model, macro-scale model and the meso-scale model quantities, respectively. In [21], a higher order homogenization method is used for dynamic problems and it is shown that the meso-scale inertia force vector, $\rho^m \ddot{u}_i^m$ (in equation (4.2)), is related to the acceleration of the gradients of the macroscopic displacement fields. The inertia force vector of a material point in the macroscopic model is equal to the volume average of the inertia force vectors of the heterogeneous body over a sample volume associated to that material point, that is, $\rho^M \ddot{u}_i^M = \int_{\Omega^m} \rho^\zeta \ddot{u}_i^\zeta d\Omega^m$. The meso-scale inertia force can be related to the macroscopic strain acceleration through an equation which satisfies these aforementioned conditions [23]:

$$\rho^m \ddot{u}_i^m(\boldsymbol{x^M}, \boldsymbol{x^m}, t) = \rho^M h_i^{pq}(\boldsymbol{x^M}, \boldsymbol{x^m}, t)\ddot{\varepsilon}_{pq}^M(\boldsymbol{x^M}, t) \tag{4.3}$$

in which h_i^{pq} is a periodic tensor which is normalized as:

$$\int_{\Omega^m} h_i^{pq}(\boldsymbol{x^M}, \boldsymbol{x^m}, t) d\Omega^m = 0 \tag{4.4}$$

Tensor h_i^{pq} depends on the meso-scale model heterogeneity and material properties. For a homogeneous meso-scale model, tensor h_i^{pq} vanishes. Equation (4.3) denotes that the meso-scale inertia forces can be expressed in terms of the macro-scale strain acceleration and the meso-scale heterogeneity and material properties. Using this equation, the time-dependent terms ($\ddot{u}_i^m$) can be eliminated from the meso-scale model. Inserting equations (2.2)-(2.4), (4.2) and (4.3) into the heterogeneous model momentum equation (3.2) and using averaging equations (2.5) and (2.6), the equation of motion for the bulk domain of the macro-scale model can be derived as [23]:

$$\frac{\partial}{\partial x_j^M}(\sigma_{ij}^M + \zeta^2 D_{ijkl}\ddot{\varepsilon}_{kl}^M) = \rho^M \ddot{u}_i^M \quad \text{on} \quad \Omega^M \setminus \Gamma_d^M \tag{4.5}$$

where the dispersion tensor D_{ijkl} can be defined as:

$$D_{ijkl} = \frac{\rho^M}{|\Omega^m|} \int_{\Omega^m} h_s^{ij} h_s^{kl} d\Omega^m \tag{4.6}$$

The weak form (2.12) can be modified for this problem as:

$$\begin{aligned} &\int_{\Gamma_t^M} \delta\vartheta \left(\sigma_{ij} + \zeta^2 D_{ijkl}\ddot{\varepsilon}_{kl}^M\right) n_i^M d\Gamma_t^M - \int_{\Omega^M} \frac{\partial \delta\vartheta}{\partial x_i} \left(\sigma_{ij} + \zeta^2 D_{ijkl}\ddot{\varepsilon}_{kl}^M\right) d\Omega^M \\ &- \int_{\Gamma_d^M} \delta [[u]]_i^M t_i d\Gamma_d^M = \int_{\Omega^M} \delta\vartheta \rho^M \ddot{u}_i^M d\Omega^M \end{aligned} \tag{4.7}$$

The discretized equations for the macro-scale model can be written as:

$$(\boldsymbol{M^M} + \boldsymbol{m_D^M})\boldsymbol{\ddot{u}^M} = \boldsymbol{f_{ext}^M} - (\boldsymbol{f_{bulk}^M} + \boldsymbol{f_{coh}^M}) \tag{4.8}$$

where $\boldsymbol{m}^{\boldsymbol{M}}_{\boldsymbol{D}}$ is the mass matrix corresponding to the meso-scale inertia forces and can be obtained via:

$$\boldsymbol{m}^{\boldsymbol{M}}_{\boldsymbol{D}} = \int_{\Omega^M} \boldsymbol{B}^T \boldsymbol{D}\boldsymbol{B}\, d\Omega^M \tag{4.9}$$

A non-zero dispersion tensor, $\boldsymbol{D}$ results in a non-zero consistent additional mass matrix $\boldsymbol{m}^M_D$. Similar to the problem in chapter 3, an implicit Newmark time integration scheme is used to solve equation (4.8) and $\boldsymbol{f}^{\boldsymbol{M}}_{\boldsymbol{bulk}}$ and $\boldsymbol{f}^{\boldsymbol{M}}_{\boldsymbol{coh}}$ are computed from the meso-scale problem (RVE) using standard computational homogenization (2.4.1) and discontinuous computational homogenization (2.4.2) schemes, respectively. A gradient-enhanced damage model (see section (3.2.2)) is also used for the meso-scale model. For computing the dispersion tensor using equation (4.6), the components of tensor h^{pq}_i should be determined. The procedure for finding tensor h^{pq}_i is given in the following section.

4.2.2. Determination of tensor h^{pq}_i

The effect of inertia at the meso-scale is represented as an eigenstrain which is assumed to be proportional to the mass density at meso-scale [23]:

$$\varepsilon^I_{ij} = \frac{\rho^m}{\rho^M} f^M_{ij} \tag{4.10}$$

f^M_{kl} is a function of macro-scale strain acceleration $\ddot\varepsilon^M_{kl}$ such that for $\ddot\varepsilon^M_{kl} = 0$, $f^M_{kl} = 0$. Equation (4.10) shows that inertia acts as an eigenstrain and changes the shape and volume of the material. In equation (2.3), the meso-scale displacement derivative $u^m_{(i,x^m_j)}$ can be witten as [23]:

$$\dot u^m_{(i,x^m_j)} = H^{kl}_{(i,x^m_j)} \dot\varepsilon^M_{kl} + \dot\varepsilon^I_{ij} + h^{kl}_{(i,x^m_j)} \dot f^M_{kl} \tag{4.11}$$

where H^{kl}_i is a periodic tensor which is related to the meso-scale model behavior. Substituting (4.10) into equation (4.11) and then inserting (4.11) into the rate form of equation (2.3), the meso-scale strain rate can be written as:

$$\begin{aligned} \dot\varepsilon^m_{kl}(\boldsymbol{x^M}, \boldsymbol{x^m}, t) \quad = \quad & \left[I_{klpq} + H^{pq}_{(k,x^m_l)}(\boldsymbol{x^M}, \boldsymbol{x^m}, t) \right] \dot\varepsilon^M_{pq}(\boldsymbol{x^M}, t) + \\ & \left[\frac{\rho^m(\boldsymbol{x^m})}{\rho^M} I_{klpq} + h^{pq}_{(k,x^m_l)}(\boldsymbol{x^M}, \boldsymbol{x^m}, t) \right] \dot f^M_{pq}(\boldsymbol{x^M}, t) \end{aligned} \tag{4.12}$$

Substituting (4.12) into the meso-scale constitutive law (equation (3.6)) in rate form (when $\omega = 0$) and substituting the meso-scale stress into the momentum equation (2.15) and making use of arbitrariness of $\dot\varepsilon^M_{ij}$ and $\dot f^M_{ij}$ one obtains:

$$\frac{\partial}{\partial x^m_j} \left[C^m_{ijkl}(\boldsymbol{x^m}, t) \left[I_{klpq} + \frac{1}{2} \left(\frac{\partial H^{pq}_k}{\partial x^m_l} + \frac{\partial H^{pq}_l}{\partial x^m_k} \right) \right] \right] = 0 \tag{4.13a}$$

$$\frac{\partial}{\partial x^m_j} \left[C^m_{ijkl}(\boldsymbol{x^m}, t) \left[\frac{\rho^m(\boldsymbol{x^m})}{\rho^M} I_{klpq} + \frac{1}{2} \left(\frac{\partial h^{pq}_k}{\partial x^m_l} + \frac{\partial h^{pq}_l}{\partial x^m_k} \right) \right] \right] = 0 \tag{4.13b}$$

Equation (4.13a) can be solved for H_i^{mn}. Inserting (4.12) into (3.6) and performing a volume average of both sides of the resulting equation over the meso-scale volume, Ω^m, and using (2.5) and (2.6) yields the following equation for the macroscopic tangent, C^M_{ijkl}:

$$C^M_{ijkl}(\boldsymbol{x^M}, t) = \int_{\Omega^m} C^m_{ijpq}(\boldsymbol{x^m}, t) \left[I_{pqkl} + H^{kl}_{(p,x^m_q)}(\boldsymbol{x^M}, \boldsymbol{x^m}, t) \right] d\Omega^m \tag{4.14}$$

However in the present work, instead of solving equation (4.13a) and using equation (4.14), the macroscopic tangent is obtained using the standard homogenization method presented in section (2.4.1) via equation (2.22). Equation (4.13b) which is called the quasi-dynamic equation can be solved to find tensor h_i^{mn}. Using test function ϑ the weak form of equation (4.13b) can be written as:

$$\begin{aligned} &\frac{1}{2}\int_{\Gamma^m} \vartheta C^m_{ijkl} \left(\frac{\partial h_k^{pq}}{\partial x_l^m} + \frac{\partial h_l^{pq}}{\partial x_k^m} \right) n_j d\Gamma^m - \frac{1}{2}\int_{\Omega^m} \frac{\partial \vartheta}{\partial x_j^m} C^m_{ijkl} \left(\frac{\partial h_k^{pq}}{\partial x_l^m} + \frac{\partial h_l^{pq}}{\partial x_k^m} \right) d\Omega^m \\ &= \int_{\Gamma^m} \vartheta C^m_{ijkl} \frac{\rho^m}{\rho^M} I_{ijkl} n_j d\Gamma^m - \int_{\Omega^m} \frac{\partial \vartheta}{\partial x_j^m} \left(C^m_{ijkl} \frac{\rho^m}{\rho^M} I_{ijkl} \right) d\Omega^m \end{aligned} \tag{4.15}$$

By inserting discretized form of h_i^{pq} and test function ϑ into (4.15), one can find the discretized set of equations for 2D problems as:

$$\begin{bmatrix} \boldsymbol{K}^{pq}_{11} & \boldsymbol{K}^{pq}_{12} \\ \boldsymbol{K}^{pq}_{21} & \boldsymbol{K}^{pq}_{22} \end{bmatrix} \begin{bmatrix} \bar{\boldsymbol{h}}^{pq}_{1} \\ \bar{\boldsymbol{h}}^{pq}_{2} \end{bmatrix} = \begin{bmatrix} \boldsymbol{f}^{pq}_{1} \\ \boldsymbol{f}^{pq}_{2} \end{bmatrix} \quad p,q = 1,2 \tag{4.16}$$

where $\bar{\boldsymbol{h}}^{pq}_{\boldsymbol{i}}$ are the nodal values for h_i^{pq}. $\boldsymbol{K}^{pq}_{\boldsymbol{ij}}$ and $\boldsymbol{f}^{pq}_{\boldsymbol{i}}$ are given in A. In order to solve system of equations (4.16), condition (4.4) and periodicity of h_i^{pq} should be satisfied over the meso-scale domain. Periodicity of h_i^{pq} can be achieved by applying periodic boundary conditions on the RVE (same as in figure 2.2 for the displacement field). Once tensor h_i^{pq} is obtained, the dispersion tensor can be computed via equation (4.6).

4.3. Cracking criteria

In the continuous-discontinuous scheme, the loss of hyperbolicity criterion is employed for crack initiation and propagation. The hyperbolicity indicator is defined as [6]:

$$e = \min_{\boldsymbol{n},\boldsymbol{v}} (\boldsymbol{n} \otimes \boldsymbol{v} : \boldsymbol{A} : \boldsymbol{n} \otimes \boldsymbol{v}) \tag{4.17}$$

where $\boldsymbol{n} = (\cos\theta, \sin\theta)$ shows the normal vector to the crack surface and $\boldsymbol{v}$ is assumed to be parallel to $\boldsymbol{n}$. Tensor $\boldsymbol{A}$ is defined as:

$$\boldsymbol{A} = \boldsymbol{C^M} + \boldsymbol{\sigma}^{\boldsymbol{M}} \otimes \boldsymbol{I} \tag{4.18}$$

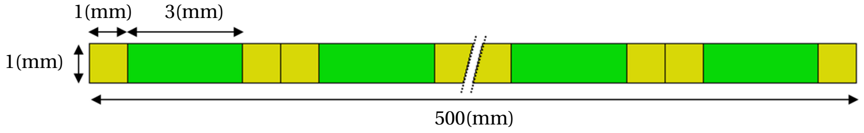

Figure 4.2: One dimensional DNS model

Based on this criterion the momentum equation loses hyperbolicity when $e < 0$ and vector $\boldsymbol{n}$ that minimizes e is normal to the direction of the crack (localization) [2]. In the multi-scale analysis, this criterion can be used to detect localization in the RVE. At each time step, having the homogenized tangent moduli, $\boldsymbol{C^M}$, tensor $\boldsymbol{A}$ can be calculated using equation (4.18). Initiation and direction of the localization can then be determined using equation (4.17). The advantage of this criterion is that both initiation and direction of the crack can be obtained from the meso-scale model which is physically more realistic.

4.4. Verification of the dispersive multi-scale model

In order to verify the proposed multi-scale model, the multi-scale simulation results are compared to a direct numerical simulation analysis. Two examples are given in this section. In the first example a one dimensional heterogeneous elastic bar under a sine pulse is given and in the second example, a two dimensional heterogeneous beam is considered in which strain localization occurs due to a propagating longitudinal wave.

4.4.1. One dimensional heterogeneous beam under impact loading

A one dimensional heterogeneous beam shown in figure 4.2 is analyzed in this section. The beam consists of material 1 (green) and material 2 (yellow). The left side of the beam is fixed and the right end is subjected to a displacement sine pulse $\bar{u}_x = A_0 \sin\left(2\pi f t\right) H\left(\frac{1}{2f} - 1\right)$ (mm). A_0 and f are the maximum applied displacement the pulse frequency, respectively. The multi-scale model for this problem is shown in figure 4.3 in which the material points of the homogeneous macro-scale model are linked to a heterogeneous RVE. The macroscopic wave length, λ^M, can be obtained via $\lambda^M = v/f$ in which v is the wave velocity which can be computed using $v = \sqrt{C^M_{11}/\rho^M}$. The material properties of different materials are E_1=200(GPa), E_2=2(GPa), ρ_1=10000(kg/m^3), ρ_2=4000(kg/m^3) and ν_1=ν_2=0.0.

Four cases are considered including (1) dispersive multi-scale model, (2) non-dispersive multi-scale model, (3) heterogeneous DNS model and (4) homogeneous DNS model. In the homogeneous DNS model, the homogenized material properties are used and it is obviously almost equivalent to the non-dispersive multi-scale model. The DNS model and the macro-scale beam in the multi-scale model are discretized using 500 beam elements and 5 beam elements are used for

---

[2] In fact, this is a condition for material stability and implies the stable response of an infinite medium in a uniform state of stress and strain when subjected to a perturbation $\boldsymbol{u} = \boldsymbol{v}e^{iwt+k\boldsymbol{n}.\boldsymbol{x}}$ [6]

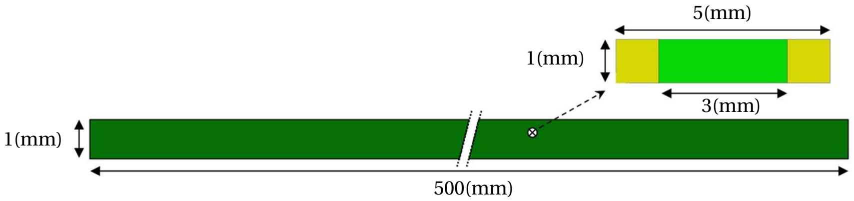

Figure 4.3: One dimensional multi-scale model

the RVE.

The macroscopic stiffness and mass density can be computed for the RVE shown in figure 4.3 as: C_{11}^M=E^M=4.926(GPa) and ρ^M=7600(kg/m^3). In a one dimensional problem, tensor $D_{ijkl} = D$ and $h_s^{ij} = h$ are scalar values. Nodal values of h can be computed by solving equation (4.16) for the one dimensional RVE shown in figure 4.3. The values of h along the RVE are shown in figure 4.4. The dispersion coefficient can be obtained using equation (4.6) as $D = 0.0095$(Pa.s^2). In [23], analytical expressions are derived for calculating homogenized stiffness and dispersion coefficient for a one-dimensional RVE shown in figure 4.3. The homogenized stiffness can be calculated using

$$E^M = \frac{E_1 E_2}{(\alpha_1 E_2 + \alpha_2 E_1)} \tag{4.19}$$

where α_i is the volume fraction of material i. The dispersion coefficient can be obtained via

$$D = \frac{1}{12}\rho^M (\alpha_1 \alpha_2)^2 \varphi^2 (l^m)^2 \tag{4.20}$$

in which $\varphi = \frac{E_2\rho_2 - E_1\rho_1}{\rho^M(\alpha_1 E_2 - \alpha_2 E_1)}$. By substituting material properties for the problem shown in figure 4.3 into equations (4.19) and (4.20), the homogenized stiffness and dispersion coefficient can be obtained as $E^M = 4.926$(GPa) and $D = 0.0095$(Pa.s^2) which are equal to the results obtained using the finite element analysis.

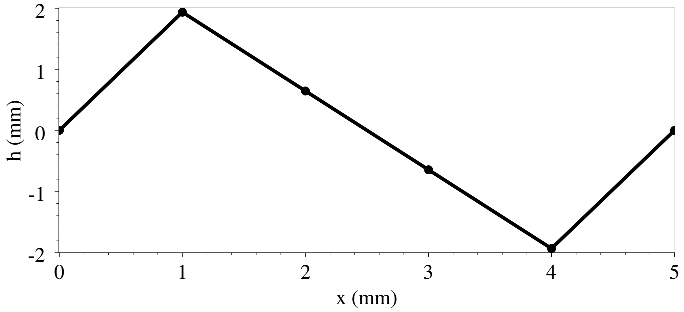

Figure 4.4: Values of h along the RVE

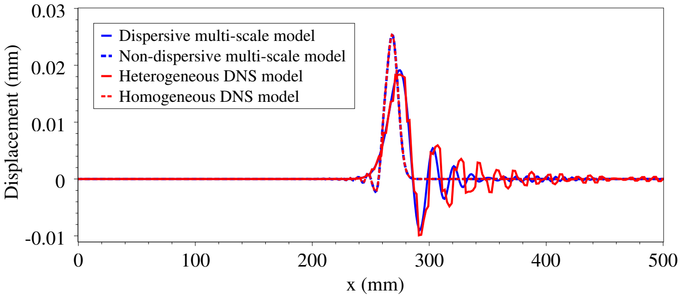

Figure 4.5: The displacement field for multi-scale models and DNS models for A_0=0.025(mm) and f=20000(Hz) at t=0.3(ms)

Figure 4.5 shows the displacement field along the beam subjected to the sine pulse with A_0=0.025(mm) and f=20000(Hz) at t=0.3(ms) for the dispersive multi-scale model, the non-dispersive multi-scale model, the heterogeneous DNS model and the homogeneous DNS model. The ratio of the RVE length to the macroscopic wave length is 0.124 for this case. As it can be observed in figure 4.5, the curves corresponding to the homogeneous DNS model and non-dispersive multi-scale model are exactly the same. This ensures that the differences between the curves are due to the dispersion effects and not due to the discretization. In figure 4.5, it can also be observed that the results of the heterogeneous DNS model and the dispersive multi-scale model are in good agreement. Figure 4.6 shows the results for the same problem when the beam is subjected to a sine pulse with A_0=0.025(mm) and f=6666.67(Hz) at t=0.3(ms). The ratio of the RVE length to the macroscopic wave length is 0.0413. As it is shown in figure 4.6, all four curves are on top of each other which certifies that for large macroscopic wave length compared to the RVE characteristic length, dispersion effects disappear. Figure 4.7 shows dispersive curves obtained from the dispersive model, non-dispersive model and exact solution of the model shown in figure 4.3. The relations for obtaining dispersive curves are given in B. As it can be observed in figure 4.7, dispersion effects are negligible up to $\frac{l^m}{\lambda^M}$=0.2 and as the ratio of the RVE size to the macroscopic wave length increases, the deviation of the dispersive model curve from the non-dispersive model curve increases. Furthermore, it is shown in figure 4.7 that the dispersive model coincides with the exact solution up to $\frac{l^m}{\lambda^M}$=0.3. However, for $\frac{l^m}{\lambda^M}$ values higher than 0.3, the error increases.

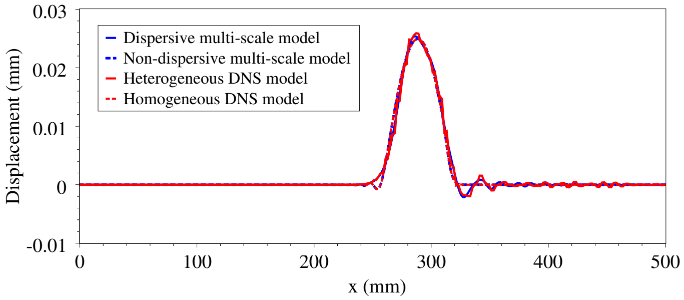

Figure 4.6: The displacement field for multi-scale models and DNS models for A_0=0.025(mm) and f=6666.67(Hz) at t=0.3(ms)

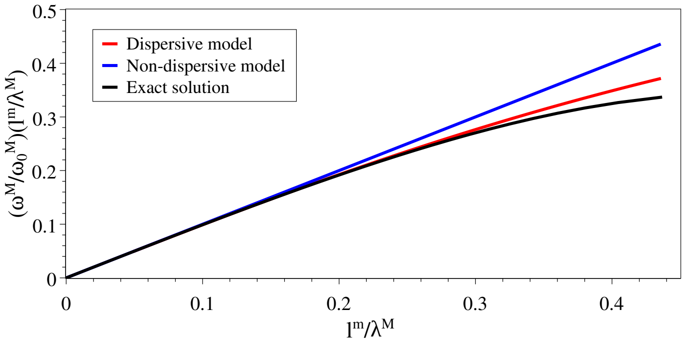

Figure 4.7: Dispersive curves for the dispersive model, the non-dispersive model and the exact solution

4.4.2. Two dimensional heterogeneous beam with strain localization under impact loading

Figure 4.8 shows a heterogeneous beam subjected to a sine pulse at the right-hand-side end. The beam consists of the bulk matrix (yellow), the matrix with voids (gray) and the stiff particles (green). The material properties are shown in table 4.1. Materials parameters c_0 and c_1 in equation (3.14) are equal to 0.5. Damage is assumed to occur only in the gray zone due to the existence of voids and it is modeled by taking a low value for the damage threshold in this area. The multi-scale model is shown in figure 4.9. The bulk part is shown in green color and cracking occurs in the gray part. The DNS model and the multi-scale model are discretized using 123,492 linear triangular elements and 769 linear quadrilateral elements, respectively.

The next step is to compute the h_s^{ij} tensor by solving equation (4.16). However, satisfying constraint (4.4) is sometimes not possible for a complex RVE (figure 4.9) because system of equations (4.16) may become overdetermined. In order to find tensor h_s^{ij}, the complex RVE is replaced by a partially homogenized RVE using the procedure shown in figure 4.10. As it is illustrated in figure 4.10, each heterogeneous unit cell is replaced by a homogenized cell using the homogenization method. Components of tensor h_s^{ij} for the partially homogenized RVE are shown in figure 4.11. Using equation 4.6, one can obtain the dispersion tensor which is written as a 3×3 matrix for the present two dimensional case as:

$$\boldsymbol{D} = \begin{bmatrix} 0.0214 & -7\times10^{-5} & 0.0 \\ -7\times10^{-5} & 0.0214 & 0.0 \\ 0.0 & 0.0 & 0.038 \end{bmatrix} (\mathrm{Pa.s^2})$$

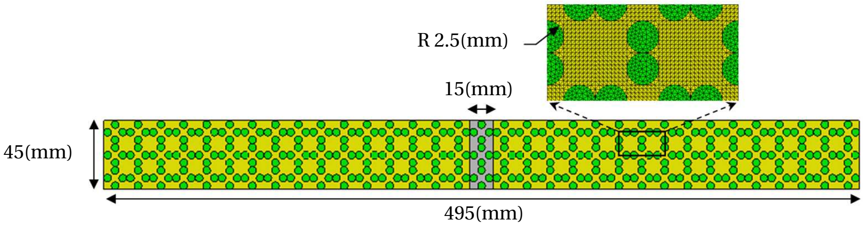

Figure 4.8: Two dimensional DNS beam model

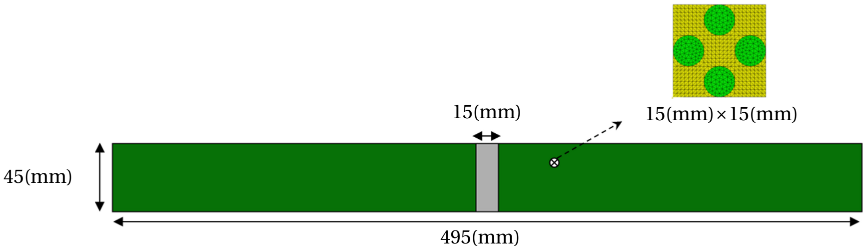

Figure 4.9: Two dimensional multi-scale beam model

Table 4.1: Material properties for heterogeneous beam

		Bulk matrix	Matrix with voids	Particle
E	[GPa]	2	2	200
ν	[−]	0.0	0.0	0.0
κ_I	[−]	0.3	5×10^{-5}	0.3
α	[−]	0.99	0.99	0.99
β	[−]	1500	1500	1500
ρ	[kg/m^3]	4000	4000	10000
c	[m^2]	10^{-7}	10^{-7}	10^{-7}

It should be noted that the dispersion tensor only depends on the configuration of the meso-scale model and contains dispersion effects due to the reflection of the wave at the interfaces of different phases. The effect of the presence

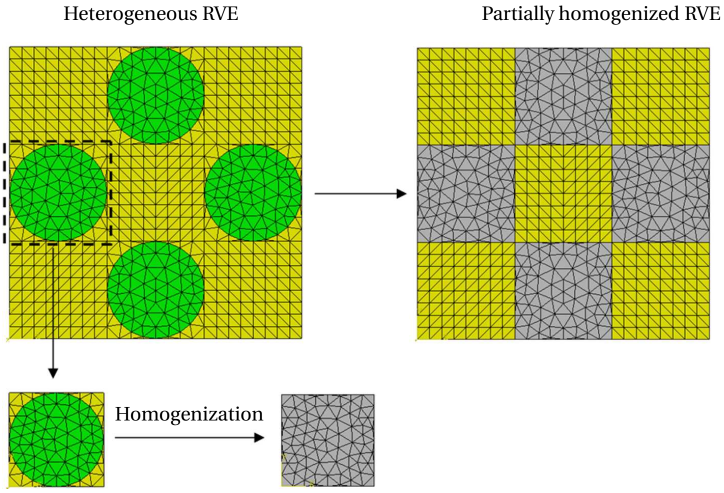

Figure 4.10: Partial homogenization of RVE

of the crack on the wave propagation is modeled explicitly via a strong discontinuity in the macro-scale model. Figure 4.12a-4.12c depict the macroscopic displacement in x direction for the dispersive multi-scale model, the non-dispersive multi-scale model and the DNS model at t=0.2304(ms), 0.3(ms) and 0.4(ms) for A_0=0.025(mm) and f=66666.68(Hz). In this case the ratio of the RVE length to the macroscopic wave length is 1.16 which denotes that the macroscopic wave length is smaller than the RVE size, so dispersion effects play a role. The black dashed line in figures 4.12b and 4.12c shows the location of the macro crack. It can be observed in these figures that the dispersive multi-scale model results are in good agreement with the results obtained from the DNS model, however, the difference between the non-dispersive model results and DNS model results is significant. In figures 4.12a-4.12c, it can be observed that as one moves away from the wave front the difference between the results obtained from the dispersive multi-scale model and the DNS model increases. This can be explained as follows. In the finite element model, in addition to physical dispersion effects, the discretization causes non-physical dispersion effects as well. After the wave has passed high frequency waves with low amplitude are still present, may accumulate and lead to non-physical dispersion. The present dispersive model does not account for non-physical dispersion effects. Since the discretization in the DNS model is considerably finer than the macro-scale discretization in the multi-scale model, the non-physical dispersion effects for the DNS model are more significant in comparison with the multi-scale model. For this reason a deviation of the DNS model results from the dispersive multi-scale model results away from the wave front can be observed. The damaged zone is given for the dispersive and non-dispersive multi-scale models and the DNS model at t=0.3(ms) in figure 4.13. The width of the localization bands (l) for the dispersive multi-scale model and the DNS model are 0.219(mm) and 0.211(mm), respectively which are almost the

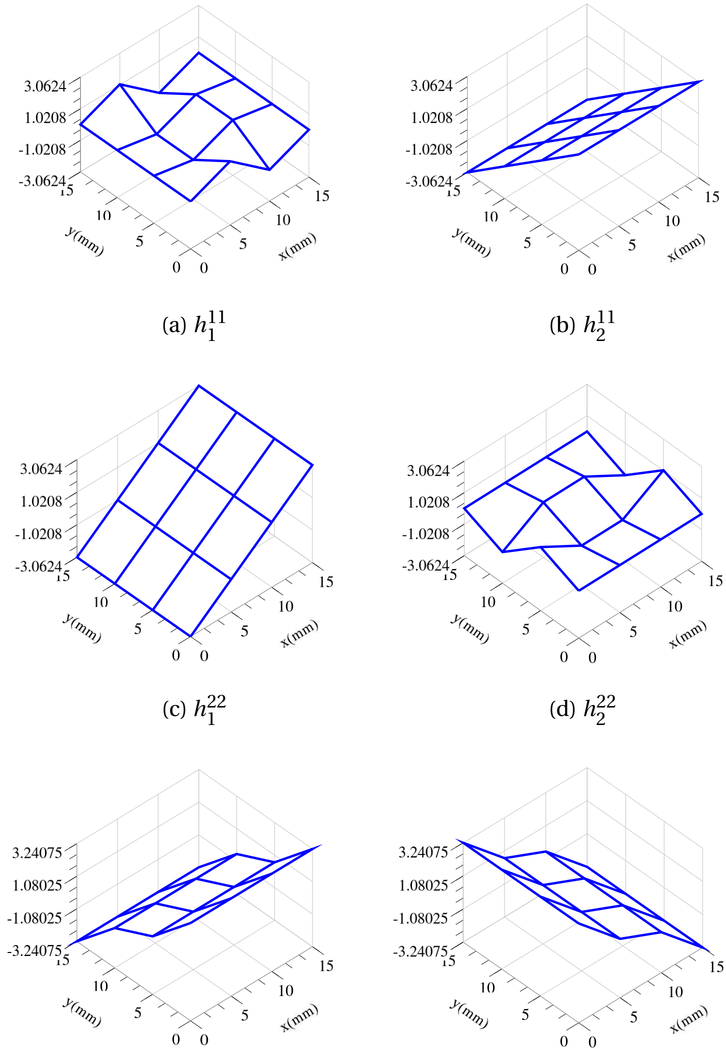

(a) h_1^{11} (b) h_2^{11}

(c) h_1^{22} (d) h_2^{22}

(e) h_1^{12} (f) h_2^{12}

Figure 4.11: Components of h_s^{ij} tensor

same but for the non-dispersive multi-scale model, the width is 0.464(mm) which is more than twice as much as the DNS model localization band width. The averaged stress over the active damaged zone versus averaged strain over the active damaged zone is shown for the three models in figure 4.14. It can be observed that the curves obtained from the dispersive multi-scale model agree with the curves of the DNS model while the non-dispersive multi-scale model predicts a larger averaged stress for a given averaged stress compared to the DNS model. This can be explained in figure 4.15 which shows the crack opening rate versus time for the dispersive and non-dispersive multi-scale models and the DNS model. The crack opening rate values are shown within the time span between the maximum traction is reached in the cohesive zone and complete crack opening (when the traction becomes zero). As it is shown in figure 4.15, energy dissipation in the cohesive zone occurs faster in the non-dispersive multi-scale model compared to the DNS model and the dispersive model. It can also be observed that the crack opening rate predicted using the DNS model and the dispersive multi-scale model are in good agreement while the crack opening rate obtained using the non-dispersive multi-scale model is larger. According to rate equation (3.14), a larger crack opening rate results in a larger strain threshold which causes an increase in the averaged stress over the active damage zone. It is worthwhile to mention that the simulation time for the DNS model until t=0.3(ms) is 13 hours and 23 minutes whereas for the multi-scale model is 6 minutes and 35 seconds using a PC with 8.0(GB) of RAM and speed 3.07(GHz).

Dispersive curves can be plotted for the present two-dimensional problem by solving an eigenvalue problem presented in B. However, in the present work, the main goal is to verify the dispersive multi-scale model.

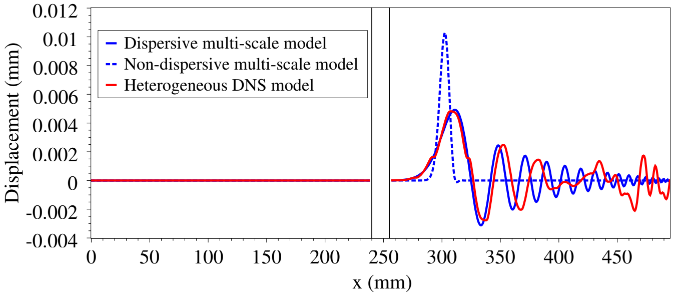

(a) t=0.2304(ms)

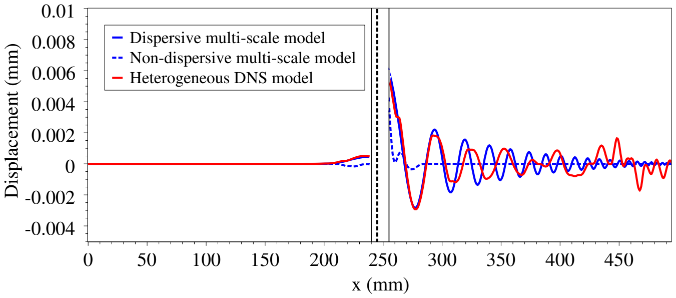

(b) t=0.3(ms)

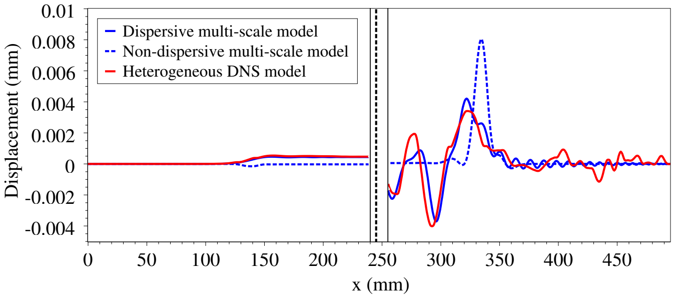

(c) t=0.4(ms)

Figure 4.12: Displacement in x direction along the beam subjected to sine pulse with A_0=0.025(mm) and $f = 66666.68$(Hz)

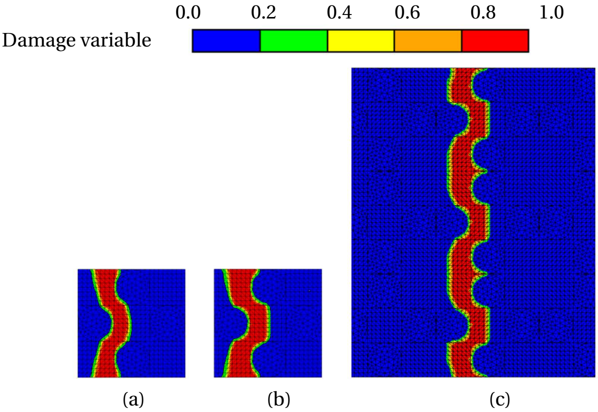

Figure 4.13: The damaged zone for (a) the dispersive multi-scale model RVE, (b) the non-dispersive multi-scale model RVE and (c) the DNS model

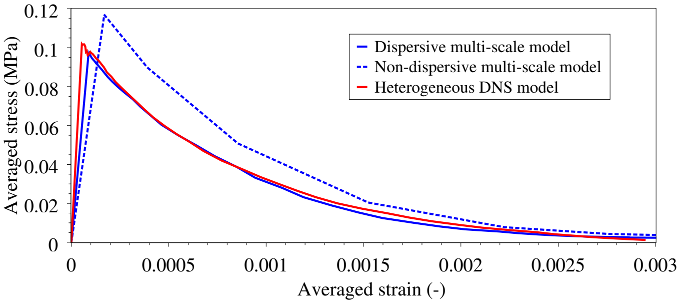

Figure 4.14: Averaged stress over active damaged zone versus averaged strain over active damaged zone

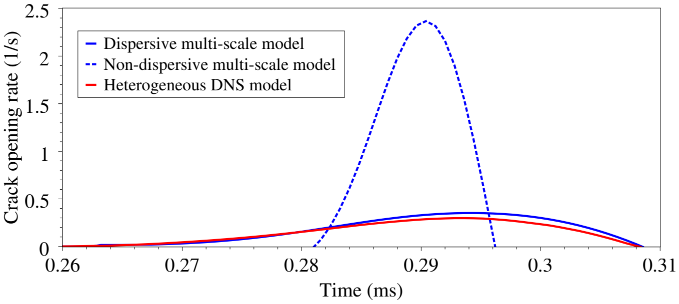

Figure 4.15: Crack opening rate for the multi-scale models and the DNS model

4.5. Objectivity of the dispersive multi-scale model

In order to investigate the objectivity of the dispersive multi-scale model, a beam of heterogeneous material shown in figure 4.16 is analyzed. The beam consists of a bulk matrix (yellow), a matrix with voids (gray) and circular particles (green). Properties of different phases are the same as in the example given in section (4.4.2) (table 4.1).

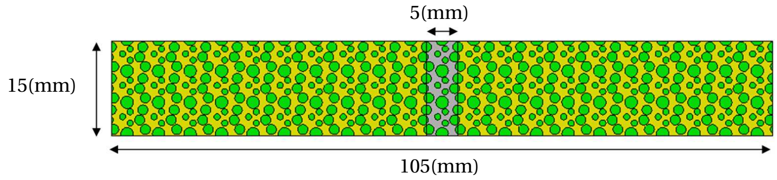

Figure 4.16: Beam of heterogeneous material

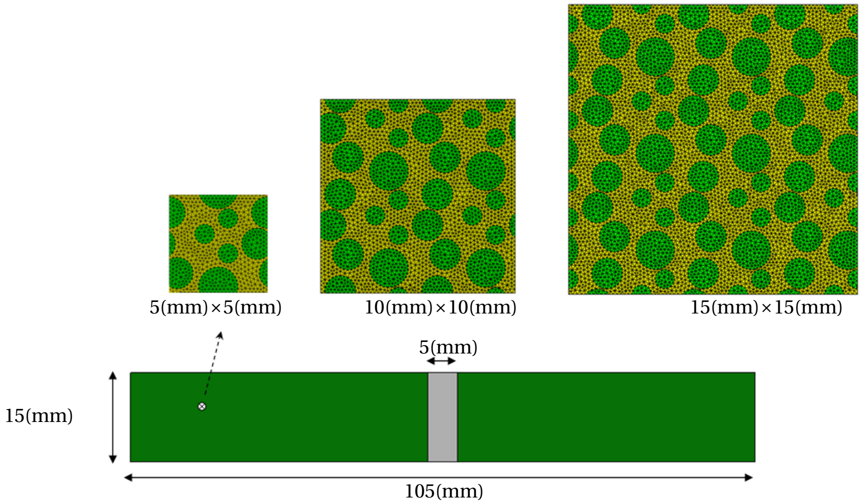

Figure 4.17: Multi-scale model with different RVE sizes

The radius of the particles is in the range of 0.5 (mm) to 1.0 (mm). The particle density is 46%. The beam is subjected to a sine pulse at the right end with A_0=0.03(mm) and f=100000(Hz) (see formulas in section (4.4.1)). The multi-scale model for the problem shown in figure 4.16, is presented in figure 4.17. Three RVE sizes including 5 × 5(mm), 10 × 10(mm) and 15 × 15(mm) are used. The dispersive tensor can be computed by solving equation (4.16) for partially homogenized mesostructures of RVEs as demonstrated in figure 4.10. The computed dispersion tensors are similar for the three RVE sizes and are equal to:

$$\boldsymbol{D} = \begin{bmatrix} 0.002609 & -2.039\times10^{-5} & 0.01332 \\ -2.039\times10^{-5} & 0.004077 & -0.002942 \\ 0.01332 & -0.002942 & 0.7526 \end{bmatrix} (\text{Pa.s}^2).$$

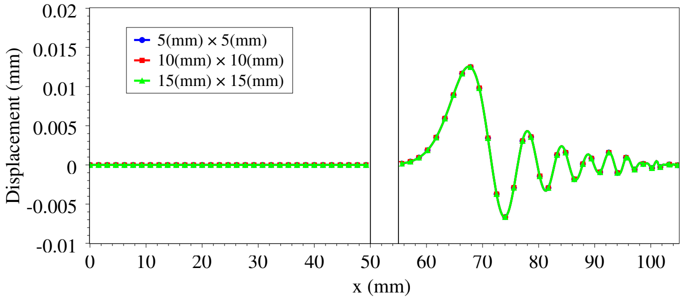

(a) t=0.05(ms)

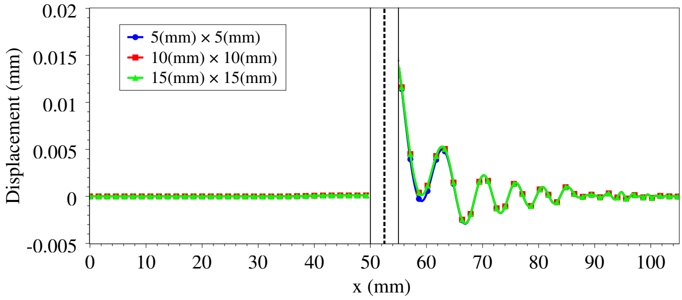

(b) t=0.07(ms)

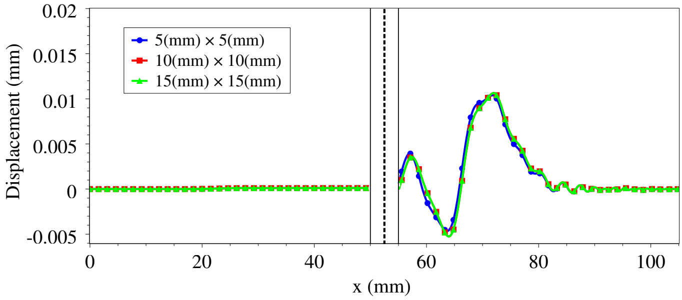

(c) t=0.09(ms)

Figure 4.18: Displacement in x direction along the beam subjected to sine pulse with A_0=0.03(mm) and f=100000.0(Hz)

The macroscopic displacements in x direction at t =0.05(ms), t =0.07 (ms) and t =0.09 (ms) are shown for different RVE sizes in figures 4.18a-4.18c. It can be observed that results obtained using the dispersive multi-scale model are objective with respect to the RVE size.

The damaged zones for different RVE sizes are shown in figure 4.19 at t =0.06(ms). The width of the localization band for 5 × 5(mm), 10 × 10(mm) and 15 × 15(mm) are 1.53(mm), 1.54(mm) and 1.58(mm), respectively. The maximum difference between computed localization band width values is 3.16% which confirms that the localization band width does not depend on the RVE size. Figure 4.20 shows the cohesive law curves obtained for different RVE sizes using the dispersive multi-scale model. As it can be seen in figure 4.20, the cohesive laws obtained using different RVE sizes are almost equivalent.

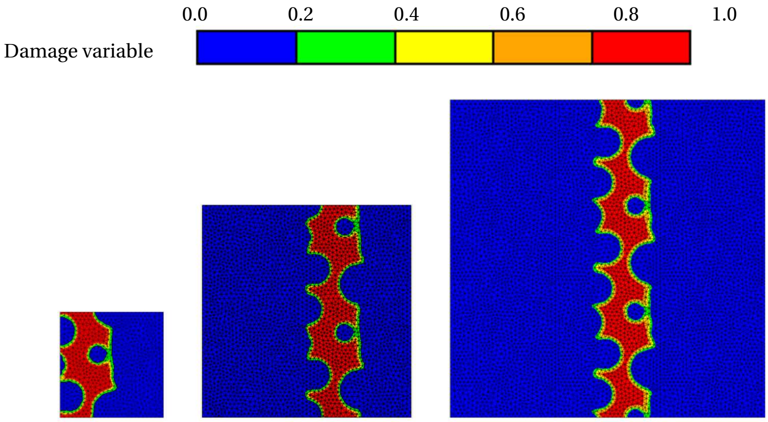

5(mm)×5(mm) 10(mm)×10(mm) 15(mm)×15(mm)

Figure 4.19: The damaged zone for various sizes of RVE

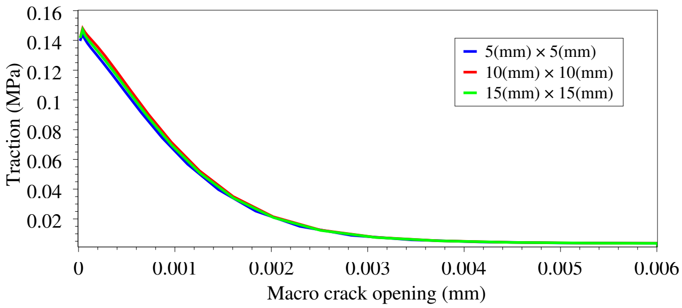

Figure 4.20: Cohesive law for the macro crack obtained using different sizes for RVE

4.6. Conclusion

In this chapter, a dispersive multi-scale model is developed for modeling cracking in quasi-brittle materials under high frequency impact loads. The dispersion effects which stem from meso-scale inertia forces are modeled by introducing an additional body force in the macro-scale model. The cohesive law for the macro-crack is obtained using a continuous-discontinuous homogenization scheme.

The dispersive multi-scale model is verified by comparing the multi-scale results with the DNS model results for various examples. It is shown that the dispersion effects are negligible when the macroscopic wave length is significantly larger than the characteristic length of the RVE and the dispersion effects increase with increasing wave frequency. It is also concluded that in order to obtain a correct cohesive law for the macro-scale cohesive crack, taking dispersion effects in high frequency loading into account, is essential. It is shown that the proposed multi-scale model is objective with respect to the RVE size.

5

A new multi-scale scheme for modeling heterogeneous incompressible hyperelastic materials

5.1. Summary

[1]A computational homogenization scheme is developed to model heterogeneous hyperelastic materials undergoing large deformations. The homogenization scheme is based on a so-called computational continua formulation in which the macro-scale model is assumed to consist of disjoint unit cells. This formulation adds no higher-order boundary conditions and extra degrees of freedom to the problem. A computational procedure is presented to calculate the macroscopic quantities from the solution of the representative volume element boundary value problem. The proposed homogenization scheme is verified against a direct numerical simulation. It is also shown that the computational cost of the proposed model is lower than that of standard homogenization schemes.

5.2. Computational homogenization scheme for large deformations

In this section, a computational homogenization scheme is developed for heterogeneous nearly incompressible hyperelastic materials. A schematic description of the computational homogenization method is shown in figure 5.1. As it can be observed, figure 5.1 is similar to figure 2.1. However, when the structure undergoes large deformations and strains, the infinitesimal strain tensor $\boldsymbol{\epsilon}$ cannot be

---

[1] Based on reference [39]

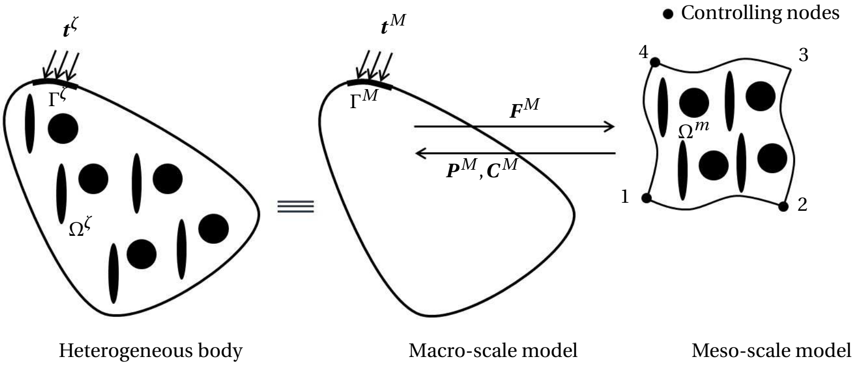

Figure 5.1: Computational homogenization scheme.

used. Therefore, as it is shown in figure 5.1, instead of the infinitesimal strain the macroscopic deformation gradient $\boldsymbol{F}^M$ is imposed as a boundary condition on the external boundaries of the RVE associated to that material point. The corresponding macroscopic first Piola-Kirchhoff stress tensor $\boldsymbol{P}^M$ and the macroscopic tangent moduli $\boldsymbol{C}^M$ can be obtained from solution of a boundary value problem for the RVE. Next, the macro-scale and the meso-scale model finite element formulations are presented in sections (5.2.1) and (5.2.2), respectively, and after explaining the computational continua model in section (5.2.3), computational procedures are given in section (5.2.4) for obtaining the macroscopic quantities from the RVE problem solution.

5.2.1. Macro-scale model

The momentum equation for the macro-scale model in the deformed configuration is given as:

$$\frac{\partial \sigma_{ij}^M}{\partial x_j^M} = 0 \tag{5.1}$$

where superscript M denotes the macro-scale model. σ_{ij}^M is the Cauchy stress and x_j^M is the coordinate in the deformed configuration. The incremental form of the constitutive equation for the macro-scale model is given as:

$$\delta \sigma_{ij}^M = C_{ijkl}^M \delta e_{kl}^M \tag{5.2}$$

in which C_{ijkl}^M contains the homogenized tangent moduli in the deformed configuration which is obtained from solution of the meso-scale problem. e_{ij}^M denotes the Almansi strain tensor which can be written in terms of macroscopic displacements u_i^M as follows:

$$e_{ij}^M = \frac{1}{2}\left(\frac{\partial u_i^M}{\partial x_j} + \frac{\partial u_j^M}{\partial x_i} - \frac{\partial u_k^M}{\partial x_i}\frac{\partial u_k^M}{\partial x_j}\right) \tag{5.3}$$

Using an updated Lagrangian formulation, the standard discretized equation for the macro-scale model can be written as [4]:

$$\left(\boldsymbol{K}_L^M + \boldsymbol{K}_{NL}^M\right)\delta\boldsymbol{u}^M = \boldsymbol{f}_{ext}^M - \boldsymbol{f}_{int}^M \tag{5.4}$$

where $\boldsymbol{K}_L^M$ and $\boldsymbol{K}_{NL}^M$ are linear and nonlinear stiffness matrices, respectively, and $\boldsymbol{f}_{ext}^M$ and $\boldsymbol{f}_{int}^M$ are external force and internal force vectors, respectively. The stiffness matrices and force vectors are given in C.

5.2.2. Meso-scale model

For hyperelastic materials, the strain energy Ψ^m can be written in terms of volumetric Ψ_{vol}^m and isochoric Ψ_{iso}^m (shape changing) parts as [45]:

$$\Psi^m = \Psi_{vol}^m(J) + \Psi_{iso}^m\left(\bar{I}_1, \bar{I}_2\right) \tag{5.5}$$

where superscript m denotes the meso-scale model. $J = det(\boldsymbol{F}^m)$, $\bar{I}_1 = J^{-2/3}I_1$ and $\bar{I}_2 = J^{-4/3}I_2$. $\boldsymbol{F}^m$ is the deformation gradient tensor and I_1 and I_2 denote first and second invariants of the right Cauchy-Green deformation tensor $\boldsymbol{C} = (\boldsymbol{F}^m)^T\boldsymbol{F}^m$, and are obtained via

$$\begin{aligned} I_1 &= tr\left(\boldsymbol{C}\right) \\ I_2 &= \frac{1}{2}\left[\left(tr\left(\boldsymbol{C}\right)\right)^2 - tr\left(\boldsymbol{C}^2\right)\right] \end{aligned} \tag{5.6}$$

in which tr denotes the trace of a matrix. Meso-scale model Cauchy stress tensor is obtained from

$$\boldsymbol{\sigma}^m = P^m\boldsymbol{I} + \boldsymbol{S}^m \tag{5.7}$$

where $\boldsymbol{I}$ is the second order unit tensor. P^m and $\boldsymbol{S}^m$ are the hydrostatic pressure and the deviatoric stress tensor, respectively and are obtained via

$$\begin{aligned} P^m &= \frac{\partial\Psi_{vol}^m}{\partial J} \\ \boldsymbol{S}^m &= \frac{1}{J}\left(2\frac{\partial\Psi_{iso}^m}{\partial\bar{I}_1}dev(\bar{\boldsymbol{b}}) + 2\frac{\partial\Psi_{iso}^m}{\partial\bar{I}_2}\left(tr(\bar{\boldsymbol{b}})dev(\bar{\boldsymbol{b}}) - dev(\bar{\boldsymbol{b}}^2)\right)\right) \end{aligned} \tag{5.8}$$

where $\bar{\boldsymbol{b}} = J^{-2/3}\boldsymbol{b}$ and $\boldsymbol{b}$ is the left Cauchy-Green deformation tensor ($\boldsymbol{b} = \boldsymbol{F}^m(\boldsymbol{F}^m)^T$). $dev(\boldsymbol{A})$ denotes the deviatoric part of tensor $\boldsymbol{A}$.

The tangent moduli in the deformed configuration can be decomposed into volumetric and isochoric terms according to:

$$\boldsymbol{C}^m = \boldsymbol{C}_{vol}^m + \boldsymbol{C}_{iso}^m \tag{5.9}$$

Volumetric and isochoric terms of tangent moduli can be obtained as

$$\begin{aligned} \boldsymbol{C}_{vol}^m &= \left(\frac{\partial\Psi_{vol}^m}{\partial J} + J\frac{\partial^2\Psi_{vol}^m}{\partial J^2}\right)\boldsymbol{I}\otimes\boldsymbol{I} - 2\frac{\partial\Psi_{vol}^m}{\partial J}\mathbb{I} \\ \boldsymbol{C}_{iso}^m &= \frac{1}{J}\left(\gamma_1\frac{\partial\Psi_{iso}^m}{\partial\bar{I}_1} + \gamma_2\frac{\partial\Psi_{iso}^m}{\partial\bar{I}_2} + \gamma_{11}\frac{\partial^2\Psi_{iso}^m}{\partial\bar{I}_1^2} + \gamma_{22}\frac{\partial^2\Psi_{iso}^m}{\partial\bar{I}_2^2} + \gamma_{12}\frac{\partial^2\Psi_{iso}^m}{\partial\bar{I}_1\partial\bar{I}_2}\right) \end{aligned} \tag{5.10}$$

in which $\mathbb{I}$ is the fourth order unit tensor and γ_1, γ_2, γ_{11}, γ_{22} and γ_{12} can be obtained as:

$$\begin{aligned}
\gamma_1 &= \frac{4}{3}\left[\bar{I}_1\left(\mathbb{I}-\frac{1}{3}\boldsymbol{I}\otimes\boldsymbol{I}\right)-\left(dev(\bar{\boldsymbol{b}})\otimes\boldsymbol{I}+\boldsymbol{I}\otimes dev(\bar{\boldsymbol{b}})\right)\right]\\
\gamma_2 &= \frac{8}{3}\left[\bar{I}_2\left(\mathbb{I}-\frac{2}{3}\boldsymbol{I}\otimes\boldsymbol{I}\right)-\bar{I}_2\left(dev(\bar{\boldsymbol{b}})\otimes\boldsymbol{I}+\boldsymbol{I}\otimes dev(\bar{\boldsymbol{b}})\right)\right.\\
&\quad\left.+\left(dev(\bar{\boldsymbol{b}}^2)\otimes\boldsymbol{I}+\boldsymbol{I}\otimes dev(\bar{\boldsymbol{b}}^2)\right)\right]+4\left(\bar{\boldsymbol{b}}\otimes\bar{\boldsymbol{b}}-\bar{\boldsymbol{H}}\right)\\
\gamma_{11} &= 4dev(\bar{\boldsymbol{b}})\otimes dev(\bar{\boldsymbol{b}})\\
\gamma_{22} &= 4\left(\bar{I}_1 dev(\bar{\boldsymbol{b}})-dev(\bar{\boldsymbol{b}}^2)\right)\otimes\left(\bar{I}_1 dev(\bar{\boldsymbol{b}})-dev(\bar{\boldsymbol{b}}^2)\right)\\
\gamma_{12} &= 4\left[dev(\bar{\boldsymbol{b}})\otimes\left(\bar{I}_1 dev(\bar{\boldsymbol{b}})-dev(\bar{\boldsymbol{b}}^2)\right)\right.\\
&\quad\left.+\left(\bar{I}_1 dev(\bar{\boldsymbol{b}})-dev(\bar{\boldsymbol{b}}^2)\right)\otimes dev(\bar{\boldsymbol{b}})\right]
\end{aligned}\tag{5.11}$$

in which $\bar{H}_{ijkl}=\frac{1}{2}\left(\bar{b}_{ik}\bar{b}_{jl}+\bar{b}_{il}\bar{b}_{jk}\right)$.

For the Mooney-Rivlin model considered in this work, the isochoric part of the energy function is obtained from

$$\Psi^m_{iso}=\alpha_1\left(\bar{I}_1-3\right)+\alpha_2\left(\bar{I}_2-3\right)\tag{5.12}$$

where α_1 and α_2 are material parameters. The volumetric part of strain energy is obtained via

$$\Psi^m_{vol}=\frac{K}{2}\left(J-1\right)^2\tag{5.13}$$

in which K denotes the bulk modulus. In order to model incompressibility, a large value should be chosen for the bulk modulus.

In the present work, a hybrid finite element formulation [66] is used to model incompressible rubber-like mesostructures. In the hybrid finite element method, the potential function is given as

$$\Pi\left(\boldsymbol{u}^m,\theta^m,P^m\right)=\int_{\Omega^m}\left[\Psi^m_{iso}(\bar{I}_1,\bar{I}_2)+\Psi^m_{vol}(\theta^m)+P^m(J-\theta^m)\right]d\Omega^m+\Pi^m_{ext}(\boldsymbol{u}^m)\tag{5.14}$$

where $\boldsymbol{u}^m$, θ^m and P^m are meso-scale model displacement field, dilatation and hydrostatic pressure, respectively, and Π^m_{ext} is the external forces potential. By taking the variation of Π with respect to $\boldsymbol{u}^m$, θ^m and P^m and performing linearization and discretization of the equations, one can find the following system of equations:

$$\begin{bmatrix}\boldsymbol{K}_{uu} & \boldsymbol{0} & \boldsymbol{K}_{uP}\\ \boldsymbol{0} & \boldsymbol{K}_{\theta\theta} & \boldsymbol{K}_{\theta P}\\ \boldsymbol{K}_{Pu} & \boldsymbol{K}_{P\theta} & \boldsymbol{0}\end{bmatrix}\begin{bmatrix}\delta\boldsymbol{u}^m\\ \delta\theta^m\\ \delta P^m\end{bmatrix}=\begin{bmatrix}\boldsymbol{F}_u\\ \boldsymbol{F}_\theta\\ \boldsymbol{F}_P\end{bmatrix}\tag{5.15}$$

where the stiffness matrices and force vectors are given in D. In the system of equations given in (5.15), $\delta\theta^m$ and δP^m can be calculated at element level as:

$$\begin{aligned}
\delta\theta^m &= \boldsymbol{K}^{-1}_{\theta\theta}\left(\boldsymbol{F}_\theta-\boldsymbol{K}_{\theta P}\delta P^m\right)\\
\delta P^m &= \boldsymbol{G}\delta\boldsymbol{u}^m+\boldsymbol{h}
\end{aligned}\tag{5.16}$$

in which

$$\begin{aligned} \boldsymbol{G} &= \left(\boldsymbol{K}_{P\theta}\boldsymbol{K}_{\theta\theta}^{-1}\boldsymbol{K}_{\theta P}\right)^{-1}\boldsymbol{K}_{Pu} \\ \boldsymbol{h} &= \left(\boldsymbol{K}_{P\theta}\boldsymbol{K}_{\theta\theta}^{-1}\boldsymbol{K}_{\theta P}\right)^{-1}\left(\boldsymbol{K}_{P\theta}\boldsymbol{K}_{\theta\theta}^{-1}\boldsymbol{F}_{\theta}-\boldsymbol{F}_{P}\right) \end{aligned} \tag{5.17}$$

Inserting (5.16) into (5.15), a condensed form of the equation can be obtained as:

$$\boldsymbol{K}_C^m\delta\boldsymbol{u}^m=\boldsymbol{F}_C^m \tag{5.18}$$

in which the components of $\boldsymbol{K}_C^m$ and $\boldsymbol{F}_C^m$ for each element can be calculated as:

$$\begin{aligned} \boldsymbol{K}_C^m &= \boldsymbol{K}_{uu}+\boldsymbol{K}_{up}\boldsymbol{G} \\ \boldsymbol{F}_C^m &= \boldsymbol{F}_u-\boldsymbol{K}_{uP}\boldsymbol{h} \end{aligned} \tag{5.19}$$

5.2.3. Computational continua formulation

In the first order homogenization theory, the RVE is subjected to a constant macroscopic deformation gradient. However, when the RVE size is large, the deformation gradient significantly varies over the RVE domain and cannot be ignored. In the present work, a computational continua model which is developed in [24] is used which requires no additional degrees of freedom and higher order boundary conditions. In the computational continua model, the macroscopic domain consists of disjoint RVEs which are located on the macro-scale element integration points as shown in figure 5.2.

The position of these integration points differs from those of standard integration points and depends on the RVE size and the macroscopic element size. The locations of the new integration points are chosen such that the integration of a function Φ over the heterogeneous domain Ω^{ζ} becomes equal to a sum of integrations of that function over the disjoint RVEs which implies:

$$\int_{\Omega^{\zeta}}\Phi\left(\boldsymbol{X}^M\right)d\Omega^{\zeta}=\sum_{I=1}^{k}\int_{\Omega^m}\hat{w}\left(\boldsymbol{X}_I^M,\boldsymbol{X}^m\right)\Phi\left(\boldsymbol{X}_I^M,\boldsymbol{X}^m\right)d\Omega^m \tag{5.20}$$

in which $\hat{w}$ is defined as:

$$\hat{w}\left(\boldsymbol{X}_I^M,\boldsymbol{X}^m\right)=\frac{j\left(\boldsymbol{X}_I^M,\boldsymbol{X}^m\right)w_I}{|\Omega^m|} \tag{5.21}$$

where k, j and w_I are the number of macroscopic element integration points, Jacobian and the nonlocal quadrature weight, respectively. It should be noted that in equation (5.20), the integral over the heterogeneous body is replaced by a sum of integrals over RVEs with finite size and unlike standard homogenization, no scale separation is introduced. It can be shown that for a bilinear quadrilateral element, the location of the integration points can be obtained as:

$$\left(\pm\xi_i,\pm\eta_i\right)=\left(\pm\sqrt{\frac{1}{3}\left(1-\frac{l_x^2}{W^2}\right)},\pm\sqrt{\frac{1}{3}\left(1-\frac{l_y^2}{H^2}\right)}\right)\qquad i=1,2,3,4 \tag{5.22}$$

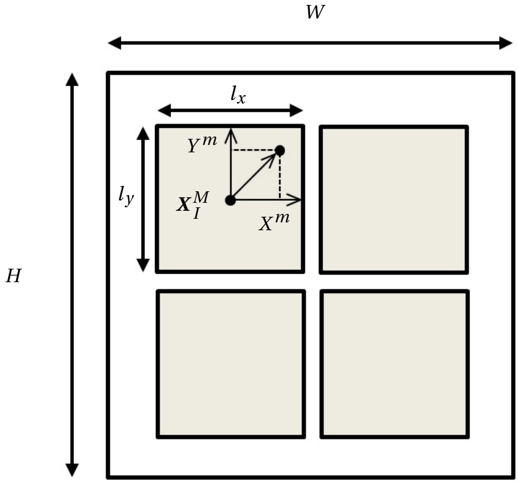

Figure 5.2: One macro-scale finite element with disjoint RVEs

where (ξ_i, η_i) denote the coordinates of the integration points of the element in the natural coordinate system. l_x, l_y, W and H are width of the RVE, height of the RVE, macro-scale element width and macro-scale element height, respectively (figure 5.2). In equation (5.22), when $l_x \to 0$ and $l_y \to 0$, the nonlocal integration points become the usual Gauss points. It should also be noted that in order to keep the value under the square root positive in equation (5.22), the macro-model finite element size must be larger than or equal to the RVE size which means: $W \geq l_x$ and $H \geq l_y$. The aforementioned formula is used for regular meshes when the macro-model finite element edges are parallel to those of the RVE. For irregular meshes, a so-called effective RVE domain can be defined. Details on defining an effective RVE domain can be found in [24].

The heterogeneous body displacement field $\boldsymbol{u}^\zeta$ and deformation gradient $\boldsymbol{F}^\zeta$ are related to the macroscopic displacement and the macroscopic deformation gradient via:

$$\begin{aligned} \boldsymbol{u}^\zeta &= \boldsymbol{u}^M + \boldsymbol{u}^* \\ \boldsymbol{F}^\zeta &= \boldsymbol{F}^M + \boldsymbol{F}^* \end{aligned} \tag{5.23}$$

where $\boldsymbol{u}^*$ denotes the displacement perturbation and $\boldsymbol{F}^M$ and $\boldsymbol{F}^*$ are defined as:

$$\begin{aligned} F_{ij}^M &= \frac{\partial u_i^M}{\partial X_j^M} + \delta_{ij} \\ F_{ij}^* &= \frac{\partial u_i^*}{\partial X_j^m} + \delta_{ij} \end{aligned} \tag{5.24}$$

in which δ_{ij} is Kronecker delta. The macroscopic deformation gradient is approximated as a linear function over the RVE:

$$F_{ij}^{M} = \bar{F}_{ij} + \overline{\frac{\partial F_{ij}}{\partial X_k^m}} X_k^m \tag{5.25}$$

where

$$\begin{aligned} \bar{F}_{ij} &= \frac{1}{|\Omega^m|}\int_{\Omega^m} F_{ij}^m d\Omega^m \\ \overline{\frac{\partial F_{ij}}{\partial X_k^m}} &= \frac{1}{|\Omega^m|}\int_{\Omega^m} \frac{\partial F_{ij}^m}{\partial X_k^m} d\Omega^m \end{aligned} \tag{5.26}$$

In the computational continua model, the first Piola-Kirchhoff stress tensor for the heterogeneous body ($\boldsymbol{P}^{\zeta}$) can be decomposed into macroscopic stress ($\boldsymbol{P}^{M}$) and meso-scale perturbation ($\boldsymbol{P}^{*}$) as [24]:

$$\begin{aligned} \boldsymbol{P}^{\zeta} &= \boldsymbol{P}^{M} + \boldsymbol{P}^{*} \\ \boldsymbol{P}^{M} &= \bar{\boldsymbol{P}}^{M} + X^m \boldsymbol{Q}_x^M + Y^m \boldsymbol{Q}_y^M \end{aligned} \tag{5.27}$$

It can be shown that $\bar{\boldsymbol{P}}^{M}$, $\boldsymbol{Q}_x^M$ and $\boldsymbol{Q}_y^M$ can be obtained as (see Appendix E):

$$\begin{aligned} \bar{\boldsymbol{P}}^{M} &= \frac{1}{|\Omega^m|}\int_{\Omega^m} \boldsymbol{P}^m d\Omega^m \\ \boldsymbol{Q}_x^M &= \frac{12}{l_x^2|\Omega^m|}\int_{\Omega^m} X^m \boldsymbol{P}^m d\Omega^m \\ \boldsymbol{Q}_y^M &= \frac{12}{l_y^2|\Omega^m|}\int_{\Omega^m} Y^m \boldsymbol{P}^m d\Omega^m \end{aligned} \tag{5.28}$$

In order to use the computational continua formulation, the macroscopic matrices and the force vector should be calculated using equation (5.20) instead of the integrals given in equations (C.1)-(C.3). For example, the macroscopic internal force vector can be computed via:

$$\boldsymbol{F}_{int}^{M} = \sum_{I=1}^{k} \int_{\Omega^m} \frac{j\left(\boldsymbol{X}_I^M, \boldsymbol{X}^m\right) w_I}{|\Omega^m|} \boldsymbol{B}_L^T\left(\boldsymbol{X}_I^M, \boldsymbol{X}^m\right) \boldsymbol{\sigma}^M\left(\boldsymbol{X}_I^M, \boldsymbol{X}^m\right) d\Omega^m \tag{5.29}$$

It should be noted that in equation (5.29), $\boldsymbol{B}_L$ is the matrix of derivatives of the macro-scale model shape functions. The macroscopic Cauchy stress $\boldsymbol{\sigma}^M$ can be obtained from the first Piola-Kirchhoff stress given in (5.27) as: $\boldsymbol{\sigma}^M = \frac{1}{J^M}\boldsymbol{P}^M \cdot \left(\boldsymbol{F}^M\right)^T$ in which $\boldsymbol{F}^M$ is the macroscopic deformation gradient and $J^M = det(\boldsymbol{F}^M)$.

5.2.4. Homogenization

In order to compute macroscopic tensors given in equations (5.28), the volume integrals can be converted into surface integrals on the boundaries of the RVE via:

$$\bar{\boldsymbol{P}}^{M} = \frac{1}{|\Omega^m|}\int_{\Omega^m} \boldsymbol{P}^m d\Omega^m = \frac{1}{|\Omega^m|}\int_{\Gamma^m} \left(\boldsymbol{f} \otimes \boldsymbol{X}^m\right) d\Gamma^m = \frac{1}{|\Omega^m|}\tilde{\boldsymbol{P}}^M \tag{5.30}$$

$$\begin{aligned}\boldsymbol{Q}_x^M = \frac{12}{l_x^2\,|\Omega^m|}\int_{\Omega^m} X^m \boldsymbol{P}^m d\Omega^m = \frac{12}{l_x^2\,|\Omega^m|}\left\{\frac{\boldsymbol{G}_1}{2}\int_{\Gamma^m} X^m\left(\boldsymbol{f}\otimes\boldsymbol{X}^m\right)d\Gamma^m + \right.\\ \left.\frac{\boldsymbol{G}_2}{2}\int_{\Gamma^m} Y^m\left(\boldsymbol{f}\otimes\boldsymbol{X}^m\right)d\Gamma^m\right\} = \frac{12}{l_x^2\,|\Omega^m|}\left\{\frac{\boldsymbol{G}_1}{2}\tilde{\boldsymbol{Q}}_x^M + \frac{\boldsymbol{G}_2}{2}\tilde{\boldsymbol{Q}}_y^M\right\}\end{aligned} \tag{5.31}$$

$$\begin{aligned}\boldsymbol{Q}_y^M = \frac{12}{l_y^2\,|\Omega^m|}\int_{\Omega^m} Y^m \boldsymbol{P}^m d\Omega^m = \frac{12}{l_y^2\,|\Omega^m|}\left\{\frac{\boldsymbol{G}_3}{2}\int_{\Gamma^m} X^m\left(\boldsymbol{f}\otimes\boldsymbol{X}^{\boldsymbol{m}}\right)d\Gamma^m + \right.\\ \left.\frac{\boldsymbol{G}_4}{2}\int_{\Gamma^m} Y^m\left(\boldsymbol{f}\otimes\boldsymbol{X}^{\boldsymbol{m}}\right)d\Gamma^m\right\} = \frac{12}{l_y^2\,|\Omega^m|}\left\{\frac{\boldsymbol{G}_3}{2}\tilde{\boldsymbol{Q}}_x^M + \frac{\boldsymbol{G}_4}{2}\tilde{\boldsymbol{Q}}_y^M\right\}\end{aligned} \tag{5.32}$$

in which $\boldsymbol{f}$ denotes the force vectors on the RVE's boundary. $\tilde{\boldsymbol{P}}^M$, $\tilde{\boldsymbol{Q}}_x^M$, $\tilde{\boldsymbol{Q}}_y^M$, $\boldsymbol{G1}$, $\boldsymbol{G2}$, $\boldsymbol{G3}$ and $\boldsymbol{G4}$ are given in Appendix F. The incremental displacement at the RVE's controlling nodes (see figure 5.1) and the incremental macroscopic deformation gradient are related via:

$$\delta\boldsymbol{u}_i^m = \boldsymbol{H}_i^T\delta\boldsymbol{F}^M \qquad i = 1,2,4 \tag{5.33}$$

The meso-scale problem stiffness in equation (5.18) can be rearranged for the independent and dependent nodes as described in [40]. It should be noted that in the finite element formulation of the macro-scale model, the geometrical nonlinearities are accounted for via nonlinear stiffness matrix $\boldsymbol{K}_{NL}^M$ (equation (C.2)) and the homogenized tangent moduli $\boldsymbol{C}^M$ is a function of the meso-scale model material response. Therefore, in order to calculate the homogenized tangent moduli from the meso-scale model stiffness matrix, only the first integral in equation (D.1) is used which is related to the meso-scale model material properties. Hence, at the converged state of the meso-scale problem, a modified matrix $\bar{\boldsymbol{K}}_C^m$ is computed by setting the second integral in equation (D.1) to zero. $\bar{\boldsymbol{K}}_C^m$ is then used to obtain the macroscopic tangent instead of $\boldsymbol{K}_C^m$. The linear system of equations for the meso-scale problem can be written as $\bar{\boldsymbol{K}}_{Cii}^m\delta\boldsymbol{u}_{ii}^m = \delta\boldsymbol{f}_{ii}^m$ in which i denotes the independent degrees of freedom. The system of equations can be rewritten as:

$$\begin{bmatrix}\bar{\boldsymbol{K}}_{Caa}^m & \bar{\boldsymbol{K}}_{Cab}^m\\ \bar{\boldsymbol{K}}_{Cba}^m & \bar{\boldsymbol{K}}_{Cbb}^m\end{bmatrix}\begin{bmatrix}\delta\boldsymbol{u}_a^m\\ \delta\boldsymbol{u}_b^m\end{bmatrix} = \begin{bmatrix}0\\ \delta\boldsymbol{f}_b^m\end{bmatrix} \tag{5.34}$$

where subscript b denotes the degrees of freedom associated to the controlling nodes (see figure 5.1) and subscript a represents the other nodes' degrees of freedom. Equation (5.34) can be written in a condensed form as:

$$\tilde{\boldsymbol{K}}_T^m\delta\boldsymbol{u}_b^m = \boldsymbol{f}_b^m \tag{5.35}$$

where $\tilde{\boldsymbol{K}}_T^m$ is calculated from stiffness matrix $\bar{\boldsymbol{K}}_T^m$ as:

$$\tilde{\boldsymbol{K}}_C^m = \left(\bar{\boldsymbol{K}}_{Cbb}^m\right)^T - \bar{\boldsymbol{K}}_{Cbb}^m\left(\bar{\boldsymbol{K}}_{Caa}^m\right)^{-1}\bar{\boldsymbol{K}}_{Cab}^m \tag{5.36}$$

Similar to the homogenized macroscopic stress tensor, the homogenized macroscopic tangent can be written as:

$$\boldsymbol{C}^M = \bar{\boldsymbol{C}}^M + X^m\boldsymbol{d}_x^M + Y^m\boldsymbol{d}_y^M \tag{5.37}$$

in which

$$
\begin{aligned}
\boldsymbol{d}_x^M &= \boldsymbol{G}_1 \tilde{\boldsymbol{d}}_x^M + \boldsymbol{G}_2 \tilde{\boldsymbol{d}}_y^M \\
\boldsymbol{d}_y^M &= \boldsymbol{G}_3 \tilde{\boldsymbol{d}}_x^M + \boldsymbol{G}_4 \tilde{\boldsymbol{d}}_y^M
\end{aligned}
\tag{5.38}
$$

Matrices $\bar{\boldsymbol{C}}^M$, $\tilde{\boldsymbol{d}}_x^M$ and $\tilde{\boldsymbol{d}}_y^M$ can be obtained via:

$$
\begin{aligned}
\bar{\boldsymbol{c}}^M &= \begin{bmatrix} \boldsymbol{H}_1 & \boldsymbol{H}_2 & \boldsymbol{H}_4 \end{bmatrix} \tilde{\boldsymbol{K}}_C^m \begin{bmatrix} \boldsymbol{H}_1 \\ \boldsymbol{H}_2 \\ \boldsymbol{H}_4 \end{bmatrix} \\
\tilde{\boldsymbol{d}}_x^M &= \frac{12}{l_x^2 \left|\Omega^m\right|} \begin{bmatrix} X\boldsymbol{H}_1 & X\boldsymbol{H}_2 & X\boldsymbol{H}_4 \end{bmatrix} \tilde{\boldsymbol{K}}_C^m \begin{bmatrix} \boldsymbol{H}_1 \\ \boldsymbol{H}_2 \\ \boldsymbol{H}_4 \end{bmatrix} \\
\tilde{\boldsymbol{d}}_y^M &= \frac{12}{l_y^2 \left|\Omega^m\right|} \begin{bmatrix} Y\boldsymbol{H}_1 & Y\boldsymbol{H}_2 & Y\boldsymbol{H}_4 \end{bmatrix} \tilde{\boldsymbol{K}}_C^m \begin{bmatrix} \boldsymbol{H}_1 \\ \boldsymbol{H}_2 \\ \boldsymbol{H}_4 \end{bmatrix}
\end{aligned}
\tag{5.39}
$$

5.3. Numerical results

In this section, numerical examples for an elastic material model and an incompressible hyperelastic material model are given. In each example three solutions including direct numerical simulation (DNS), standard homogenization and computational continua model are presented and the results are compared.

5.3.1. Elastic model - stiff particles in a soft matrix

A two-dimensional heterogeneous structure is shown in figure 5.3. The structure consists of circular aggregates (material 1, green) and matrix (material 2, yellow). Both aggregates and matrix are modeled as linear elastic material. The material properties are: E_1=40 (MPa), E_2=0.01 (MPa), υ_1=0.0, υ_2=0.49, where E and υ are Young's modulus and Poisson's ratio, respectively.

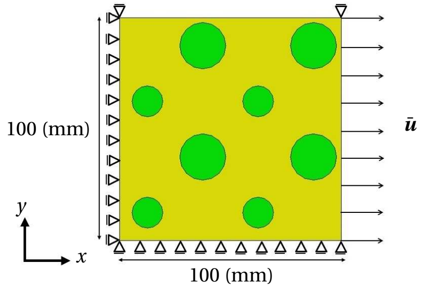

Figure 5.3: Heterogeneous elastic structure

A uniform displacement field $\bar{\boldsymbol{u}}$ is applied on the right edge which increases monotonically. The left and bottom edges are constrained in x and y directions, respectively. The displacement of the upper right node is constrained in y direction. The structure undergoes large deformations and a plane strain state is considered for the model. The DNS model and the multi-scale model for the problem are shown in figure 5.4. The DNS model is discretized using 1540 linear triangular elements. The RVE is meshed using 396 linear triangular elements which is consistent with the DNS model. Periodic boundary conditions are used for the RVE. Linear quadrilateral elements are used to discretize the macro-scale model. Three different mesh sizes are chosen for the macro-scale model which are shown in figure 5.5. For the computational continua model, a macro-scale model with 4 elements is used which is the coarsest mesh (see figure 5.5). The locations of the nonlocal integration points can be obtained using equation (5.22). For this example, l_x=l_y=W=H=50 (mm). Therefore, $\left(\pm\xi_i, \pm\eta_i\right)$=(0,0) which means that four integration points are converted into one integration point at the center of the macro-scale element. As it is discussed in section (5.2.3), for the computational continua model, the macroscopic element must be larger than or equal to the RVE size and further refinement is not possible for the present example. The reaction forces in x direction, at the right hand side edge versus applied displacement $\bar{\boldsymbol{u}}$ for the DNS model, the standard homogenization model (with 4, 16, 64 and 256 elements) and the computational continua model (with 4 elements) are shown in figure 5.6. As it can be seen in figure 5.6, for the standard homogenization model, by refining the macro-scale model mesh size, the reference solution is approached. It can also be seen that the result obtained using computational continua model with 4 elements is very close to that of the standard homogenization model with 256 elements. It can also be observed in this figure that even when using 256 elements for the macroscopic model, there is a difference between the multi-scale result and the DNS model result. Further refinement of the maro-scale model mesh size decreases the error slightly but it does not vanish. This is due to the fact that the periodicity condition which is used in the multi-scale model is only valid far enough away from the boundary and using this assumption near the boundary gives rise to errors in the solution. The distribution of the macroscopic Cauchy stress in x direction is shown for the DNS model, the standard homogenization model and the computational continua model in figure 5.7. As it can be observed in this figure, the macroscopic stress distributions for the standard homogenization model with 256 elements and the computational continua model with 4 elements are in good agreement with the DNS model. For example, in the DNS model, the macroscopic stress at the upper edge is 4e3 (Pa) and at the lower edge is 6.8e3-9.6e3 (Pa) which are the same for the standard homogenization model with 256 elements and the computational continua model with 4 elements. However, results obtained from standard homogenization with 4 and 16 elements are not accurate compared to the DNS model results. The better results obtained using the computational continua model can be explained by considering the distribution of strains over the RVE which are shown in figures 5.8 and 5.9. The distribution of the Almansi strain in x direction for the DNS model (top-right part) and RVEs associated to the specified integration points of the macroscopic element for the computational continua model and the standard homogenization model are shown in figure 5.8. Figure 5.9 depicts the distribution of the Almansi strain in y direction. Since the Poisson's ratio is non-zero for the soft material, the macroscopic stress in x direction depends on both strain in x and y directions. In figure 5.8, it can be observed that the values of the strains in x direction and the distribution over the RVEs are close to those of the DNS model for both the standard homogenization model and the computational continua model. However, in figure 5.9, the distribution of the strain in y direction over the RVEs associated to the macroscopic integration points (2) and (4) for the standard computational homogenization model differ from that of the DNS model and gives higher averaged strain values compared to the DNS model. This results in higher macroscopic strain values in y direction and consequently higher stress values in x direction compared to the DNS model (figure 5.10). Therefore, it can be concluded that for the computational continua model, the macroscopic deformation gradient which is applied on the RVE boundary is more consistent with those of the DNS model compared to the standard homogenization model. The reaction force on the right edge as a function of RVE size is plotted at $\bar{\boldsymbol{u}}$=30 (mm) for the DNS model, the standard homogenization model and the computational continua model in figure 5.11. For the results shown in figure 5.11, the macro-scale model for the computational continua model is discretized using 4 elements (element size=50×50 (mm)). As it can be observed in this figure, by increasing the RVE size (l_x=l_y) the difference between the multi-scale models and the DNS model increases and for all RVE sizes the results obtained using the computational continua model are better than those of the standard homogenization method. It can also be observed that for the present example, the more accurate results from the computational continua model can be obtained by choosing the macroscopic element size equal to the RVE size. In figure 5.12, the reaction forces as a function of RVE size are plotted for the cases in which the macro-scale model element size is equal to the RVE size for the computational continua model and the standard homogenization model (W=l_x, H=l_y). As it can be observed in figure 5.12, the computational continua model results (in contrast to the standard homogenization results for larger RVEs) are in good agreement with the DNS model results and as the RVE size decreases the difference between the results obtained from the DNS model, the standard homogenization model and the computational continua model decreases. In order to compare the computational cost for DNS model, standard homogenization and computational continua, models with the same meso-structure size (50×50 (mm)) and different macro-scale model sizes (100×100 (mm), 150×150 (mm) and 200×200 (mm)) are solved. For the standard homogenization model, the macro-scale model is discretized using 256 linear quadrilateral elements which is the minimum number of elements with which a converged solution (with respect to the mesh size) is obtained. For the computational continua model, the macroscopic element size is equal to the RVE size. The computational time versus the size of the macroscopic model is shown in figure 5.13 at nominal strain $\bar{u}/W$=0.3. In figure 5.13, it can be observed that the computational cost increases with size and for all sizes the computational time for the computational continua model is significantly lower than for the other two

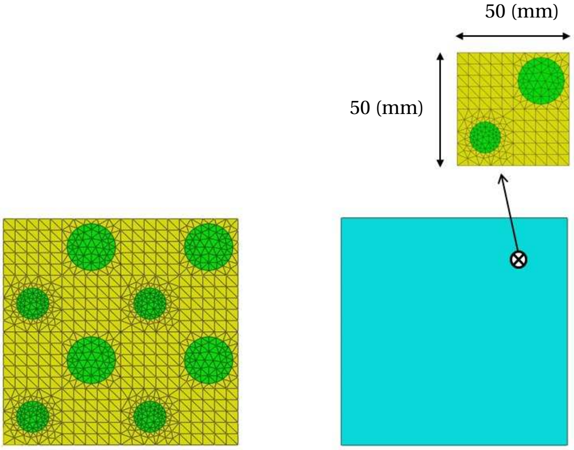

DNS model Multi-scale model

Figure 5.4: DNS and multi-scale models

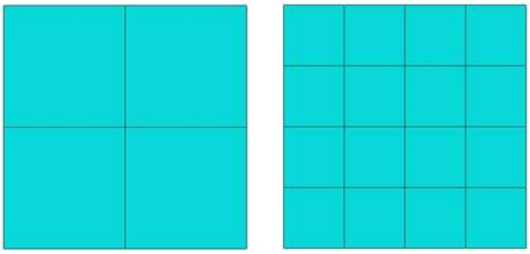

4 element 16 elements

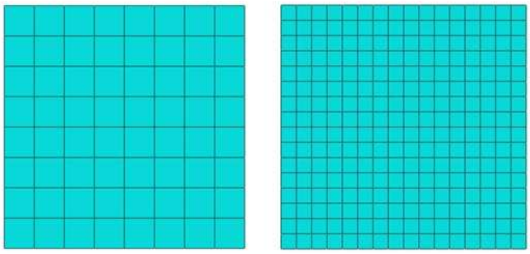

64 element 256 elements

Figure 5.5: Different mesh sizes for the macro-scale model in multi-scale simulation

models which resulted from using a coarser mesh in the computational continua model compared to the DNS model and the standard homogenization model. It should be noted that in the present example, a linear elastic material model is used and the RVE problem is solved only once and the homogenized properties are calculated a priori. As a result the computational time is directly related to the total number of degrees of freedom of the macro-scale model.

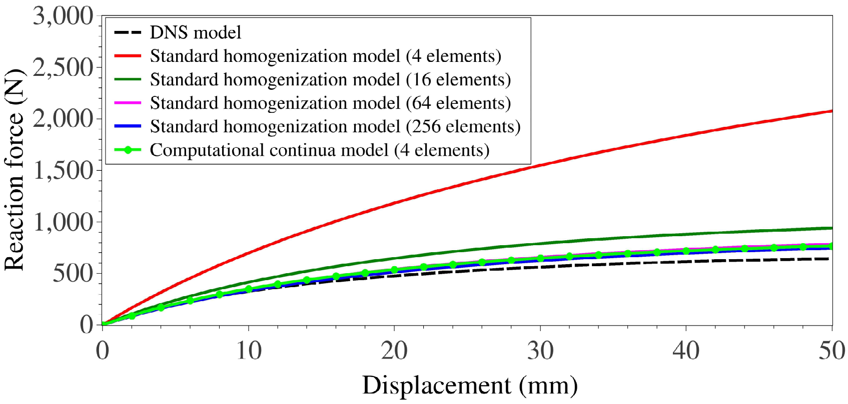

Figure 5.6: Reaction forces in x direction for different models

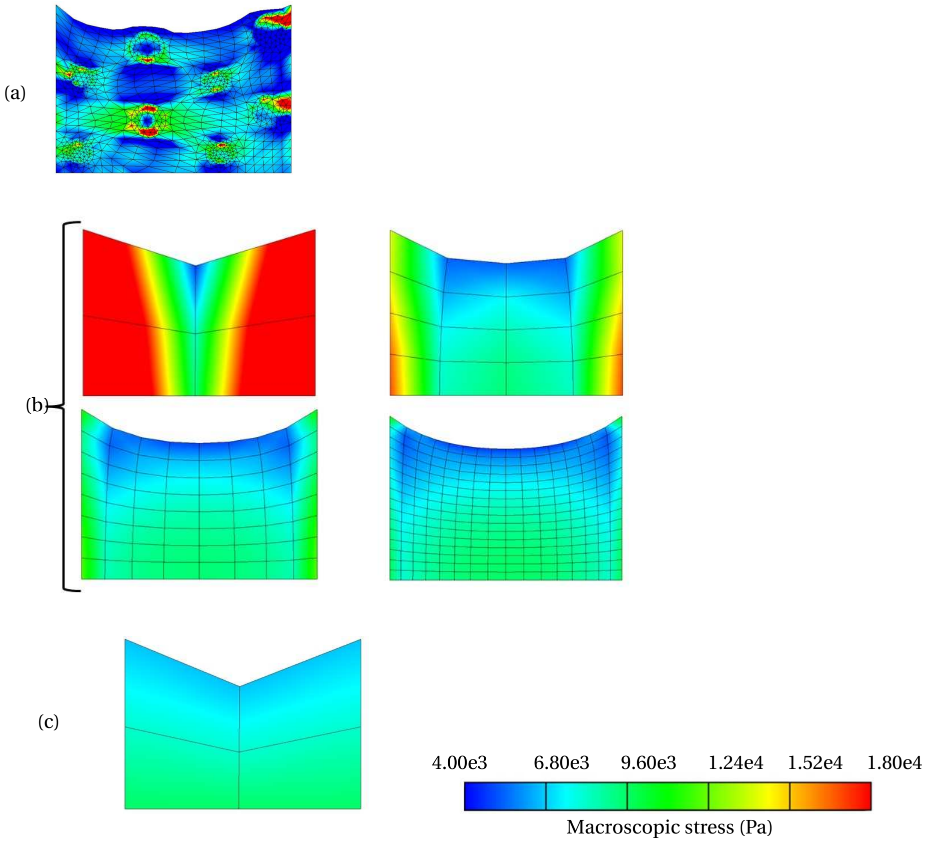

Figure 5.7: Macroscopic Cauchy distribution for (a) DNS model, (b) standard homogenization model (with 4, 16, 64 and 256 elements) and (c) computational continua model (with 4 elements)

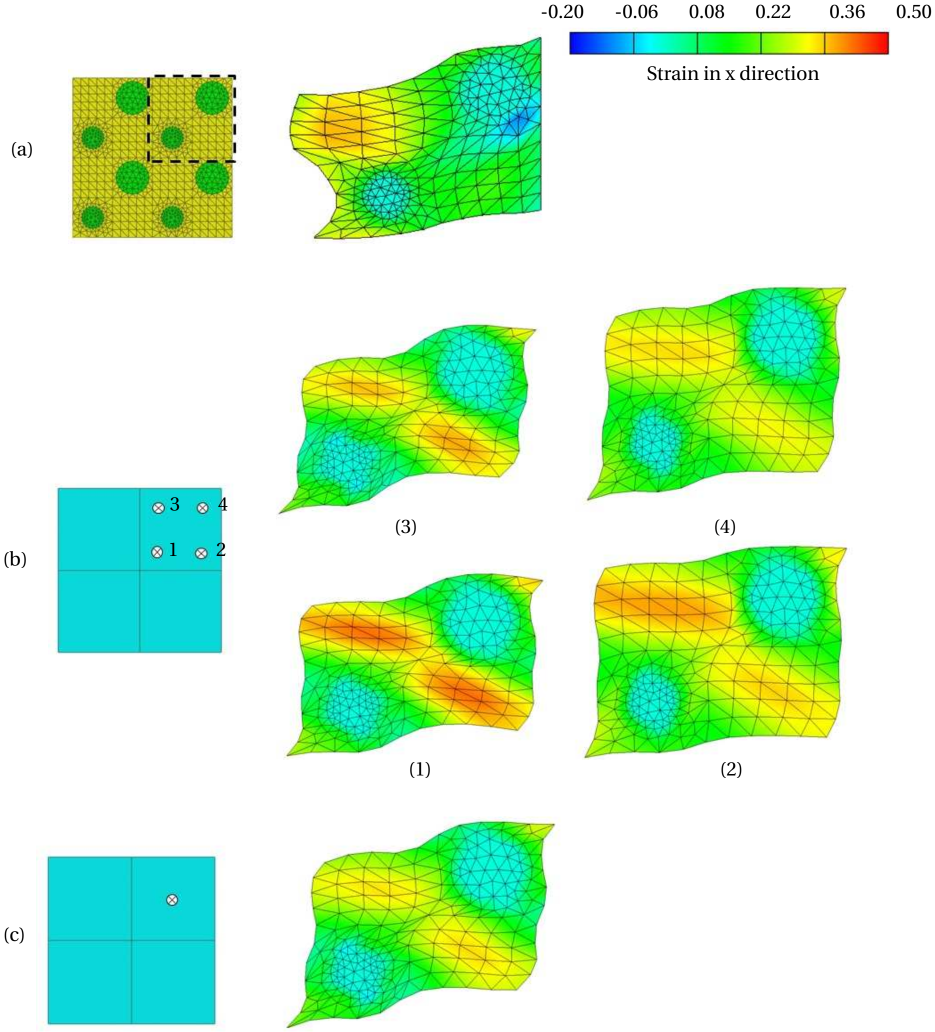

Figure 5.8: Strain distribution in x direction for (a) DNS model, (b) standard homogenization model and (c) computational continua model (with 4 elements)

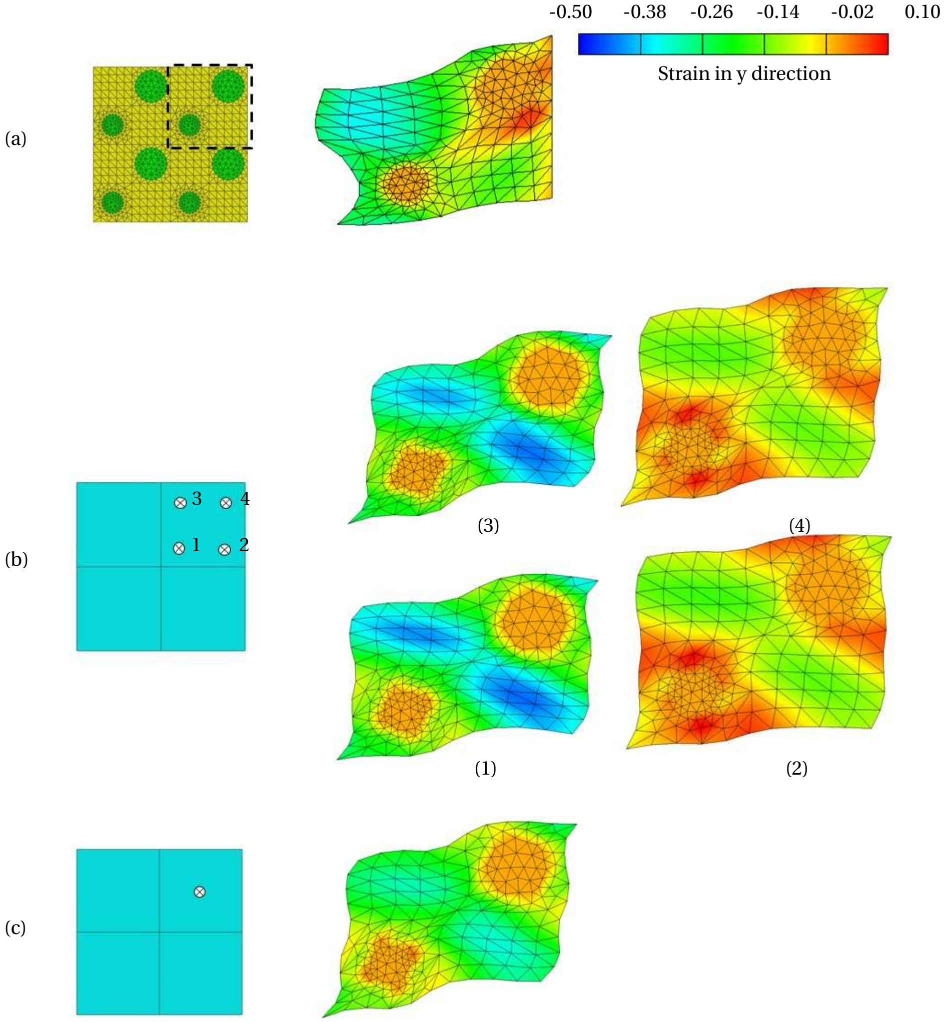

Figure 5.9: Strain distribution in y direction for (a) DNS model, (b) standard homogenization model and (c) computational continua model

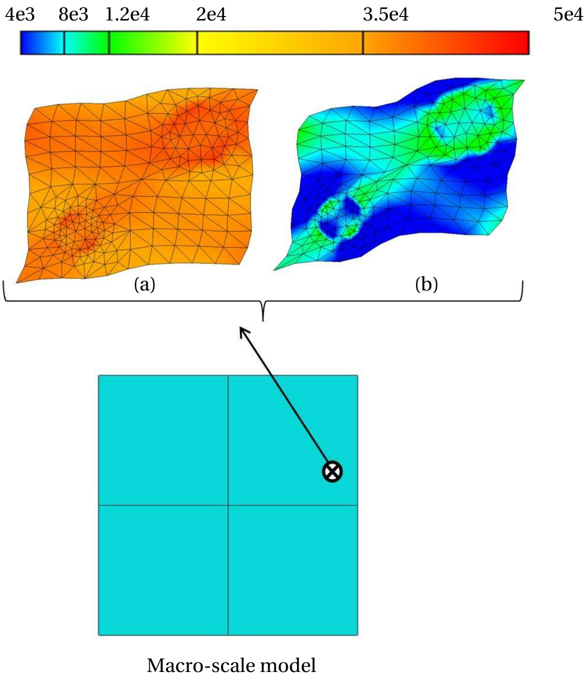

Figure 5.10: Distribution of the Cauchy stress (in Pa) in x direction over the RVE for (a) standard homogenization model and (b) computational continua model

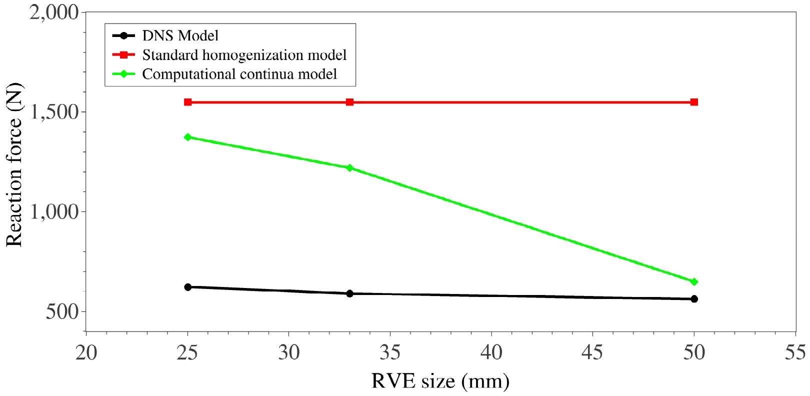

Figure 5.11: Reaction forces in x direction versus RVE size for the DNS, the standard homogenization and the computational continua models (macroscopic model is discretized by 4 elements)

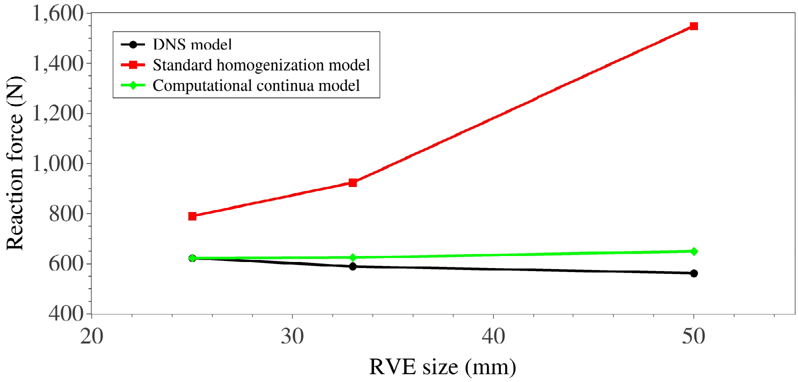

Figure 5.12: Reaction forces in x direction versus RVE size for the DNS, the standard homogenization and the computational continua models (macroscopic element size is the same as RVE size)

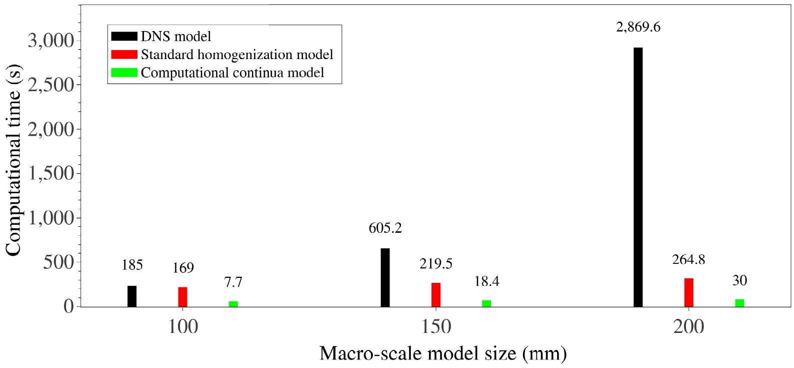

Figure 5.13: Computational time versus macro-scale model size for different models

5.3.2. Incompressible hyperelastic model - a stiff/soft layered cell

In this section, a numerical example for a heterogeneous incompressible hyperelastic structure is given. In this example, as shown in figure 5.14, a 100×100 (mm) heterogeneous structure which consists of two different hyperelastic materials is considered. An incompressible Mooney-Rivlin material model is used. The material properties are shown in table 5.1. In order to enforce the condition of incompressibility, a sufficiently large value for bulk modulus K=400 (Pa) is chosen for both materials. Material parameters α_1 and α_2 are related to the standard shear modulus via μ=2(α_1+α_2). Therefore, the material parameters given in table 5.1 denote that material 1 is stiffer than material 2. A linearly varying non-uniform

Table 5.1: Material properties of different phases

		Material 1 (green)	Material 2 (yellow)
α_1	(kPa)	5	1
α_2	(kPa)	5	6

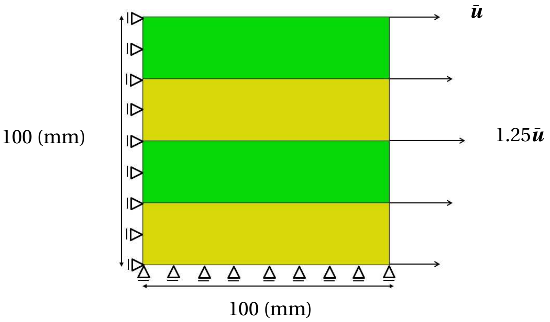

Figure 5.14: Heterogeneous hyperelastic structure

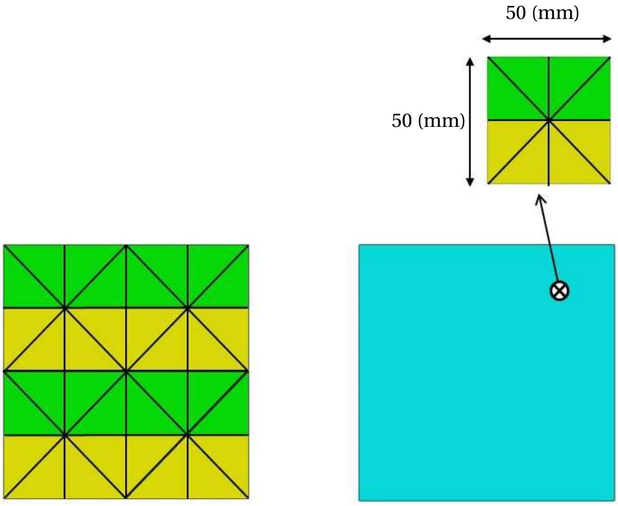

DNS model

Multi-scale model

Figure 5.15: DNS and multi-scale models

displacement field is applied on the right edge and a plane strain state is assumed. The DNS and the multi-scale models for the problem are shown in figure 5.15. A linear boundary condition is used for the RVE. Three different mesh sizes are considered for the macro-scale model which are shown in figure 5.16.

The reaction forces at the right edge of the structure versus applied displacement $\bar{\boldsymbol{u}}$ for the DNS model, the standard homogenization model (with 4, 16 and 64 elements) and the computational continua model with 4 elements are shown in figure 5.17. It can be seen that the results for the standard homogenization model with 16 and 64 elements and the computational continua model with 4 elements are in good agreement with the DNS model result, however, for applied displacement values larger than 35 (mm) the standard homogenization model with 4 elements, results in a lower reaction force compared to the DNS model. It can also be observed in figure 5.17 that the reaction force for standard computational homogenization with 64 elements slightly deviates from the DNS results. The error at x=80 (mm) is 2.02%. Increasing the number of macro-scale finite elements does not improve the results. This error is due to fact that in the computational homogenization model, a linear boundary condition is used for the RVE which is not properly valid near the boundaries (as explained in section (5.3.1)).

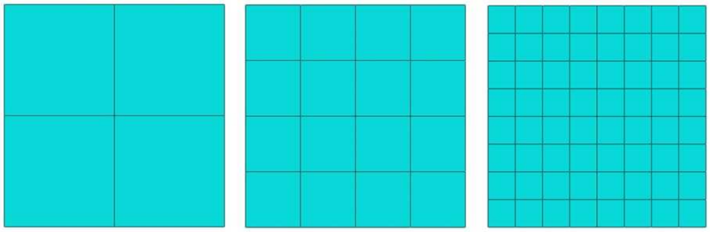
4 element 16 elements 64 elements

Figure 5.16: Different mesh sizes for the macro-scale model

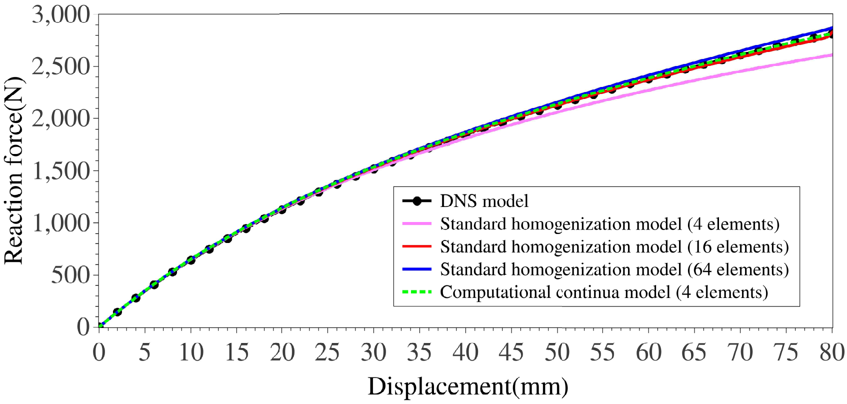

Figure 5.17: Reaction forces in x direction for different models

The distribution of the macroscopic Cauchy stress in x direction is shown for the DNS model, the standard homogenization model and the computational continua model in figure 5.18. The macroscopic stress distribution for the computational continua model with 4 elements is in good agreement with that of the DNS model whereas in case of the standard homogenization model, one needs to refine the macroscopic mesh to converge to the reference solution. Figure 5.19

shows the distribution of the meso-scale Cauchy stresses in x direction over an RVE associated to the macroscopic integration point (shown in the figure 5.19) for the standard homogenization model and the computational continua model with 4 elements. It can be seen that the stress values obtained from the standard computational homogenization method are higher than those of computational continua model. This results in higher values of the macroscopic stresses and consequently higher reaction forces.

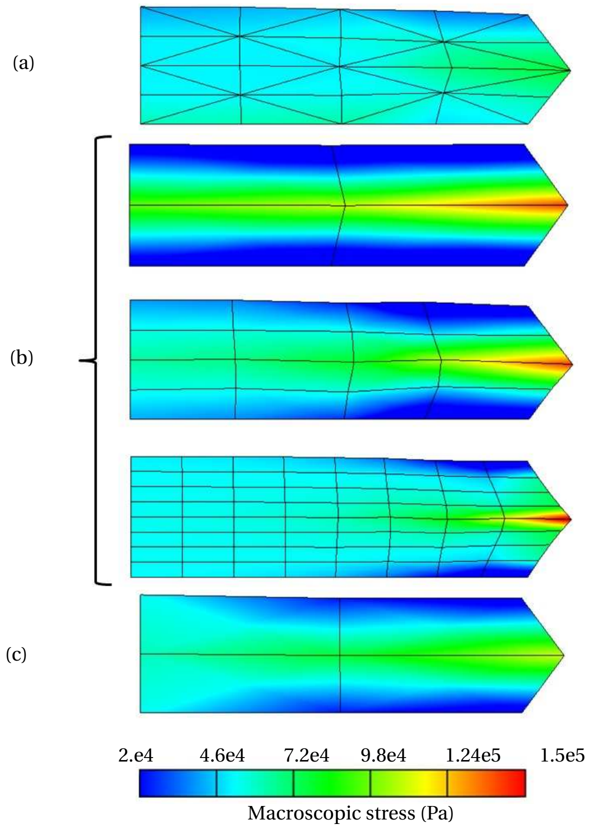

Figure 5.18: Macroscopic Cauchy stress distribution for (a) DNS model, (b) standard homogenization model (with 4, 16 and 64 elements) and (c) computational continua model (with 4 elements)

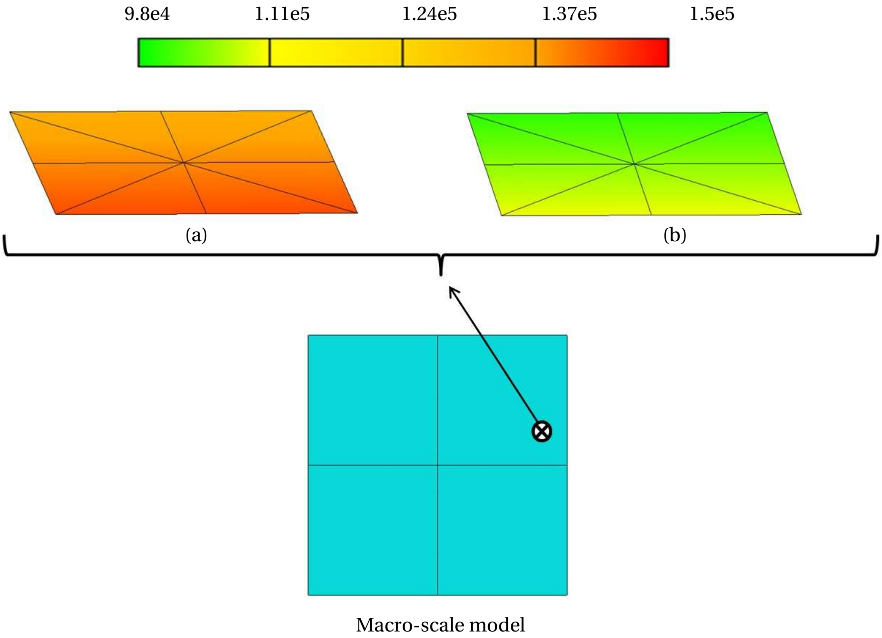

Figure 5.19: Distribution of the Cauchy stress (in Pa) in x direction over the RVE for (a) standard homogenization model and (b) computational continua model

5.4. Conclusion

In this chapter, based on a so-called computational continua model, a computational homogenization scheme is developed for modeling heterogeneous incompressible hyperelastic structures under large deformations. This model requires neither higher-order boundary conditions unlike higher-order homogenization methods nor extra degrees of freedom unlike gradient elasticity methods. The numerical implementation aspects of the homogenization procedure to calculate the macroscopic properties using the solution of the RVE problem are presented and discussed. Using two numerical examples including a heterogeneous elastic structure and a heterogeneous hyperelastic structure, the proposed multi-scale model is verified against a DNS model. Furthermore, it is shown that, using the present homogenization scheme, one can achieve the reference solution with a significantly coarser macroscopic mesh compared to the standard homogenization scheme which results in lower computational cost. The computational continua model is limited to cases in which the macroscopic element is larger than the RVE size. In the present work it is also shown that due to the invalidity of the periodicity close to the boundaries, using the usual boundary conditions such as periodic boundary condition and linear boundary condition causes an error in the computational homogenization model solution close to the boundaries.

6

A numerical homogenization scheme for glass particle-toughened polymers under dynamic loading

6.1. Summary

[1] In this chapter, a numerical homogenization scheme is presented to model glass particle-toughened polymer materials under dynamic loading. A constitutive law is developed for the polymer material and validated by comparing the results to experimental test data. A similar constitutive law as that of the polymer material with unknown material parameters is assumed for the glass particle-toughened polymer. A homogenization scheme is used to determine the unknown material parameters from the boundary value problem (BVP) of a representative volume element. Unlike the standard computational homogenization scheme, the proposed numerical homogenization scheme can be used after localization occurs in the material. The proposed multi-scale model is then verified against direct numerical simulation.

6.2. Introduction

Polymer materials have a wide range of applications due to their tunable material properties, ease of processing and low cost. The impact resistance which is related to the material toughness is important in the applications such as the automotive industry and defense industry where systems and structures may be subjected to intense dynamic loadings.

---

[1] Based on reference [35]

Polymer materials can exhibit both ductile and brittle responses. The ductile response is due to plastic deformations in the material and the brittle response is caused by initiation of localized crazes which can lead to brittle fracture. At high deformation rates, polymer materials behave more brittle which is not desirable for impact resistance applications. In order to enhance fracture toughness of polymer materials under high strain rates, glass or rubber particles can be added to the polymer matrix which promote the plastic deformations in the polymer matrix and result in an improvement of the particle-toughened polymer toughness. Adding the particles to the polymer matrix can also improve the stiffness of the mixture. The strength of the particle-toughened polymer depends on the bonding between particles and polymer matrix. For a well-bonded particle the strength increases, however, weak bonding between particles and polymer matrix may reduce the strength of the particle-toughened polymer [27].

The standard computational homogenization scheme can be used when the strain field is more or less constant over the volume of the RVE. In the particle-toughened polymer material, strain localization can occur in the forms of localized crazes and shear bands (plastic deformations). Therefore, the standard computational homogenization scheme cannot be used after strain localization occurs in the polymer matrix.

The continuous-discontinuous scheme (2) may also be extended for modeling shear banding in ductile materials. This can be achieved by modeling a shear band as a strong tangential discontinuity [61] and linking the corresponding cohesive law to averaged properties of the localized band in the RVE. However this is out of the scope of this chapter.

In this chapter, a numerical homogenization scheme is developed to model glass particle-toughened polymer materials. A viscoplastic material model for the polymer is developed and verified against experimental results. This model is not coupled to a damage model or discontinuous failure model to simulate the post-peak response. In the homogenization scheme, it is assumed that the macroscopic behavior of the glass particle-polymer composite is governed by the same constitutive law as the polymer material with unknown material parameters. A homogenization method is presented to obtain the unknown material parameters from an RVE problem. It is shown that unlike standard computational homogenization, the proposed method can be used after strain localization occurs in the material. Furthermore, initiation of crazing in the polymer material is investigated. The multi-scale model is then verified against direct numerical simulation (DNS) results.

6.3. Material model for glassy polymer under dynamic loading

The stress-strain response of a glassy polymer material during dynamic tension loading is shown in figure 6.1. Four different regions can be observed during deformation: i) elastic, ii) yielding, iii) strain softening and iv) strain hardening. As it is proposed by Haward and Thackray [33], the total stress can be decomposed into two components: 1) a viscous component due to inter-molecular interactions and 2) an elastic hardening component which is related to the entangled molecular network. In the following sections a constitutive law is formulated based on this stress decomposition and the required material parameters are obtained for the soft, transparent polyurethane elastomeric polymer, Clear Flex 75 (CF 75), using the experimental data reported in [17, 19].

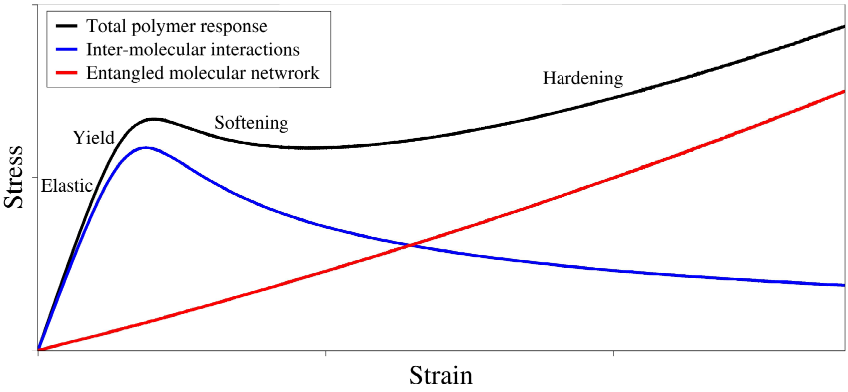

Figure 6.1: Stress-strain response of glassy polymer material

6.3.1. Constitutive law

The constitutive model is shown in figure 6.2. Chains (I) and (II) represent the elasto-visco plastic response (inter molecular interactions) and the linear elastic hardening response (network), respectively. E^I, E^{II} and η are Young's modulus for chain (I), Young's modulus for chain (II) and the viscosity of the material, respectively, and they are strain rate dependent.

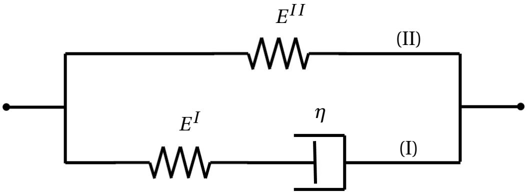

Figure 6.2: The constitutive model for the glassy polymer.

The total 2nd Piola-Kirchhoff stress can be obtained as:

$$\boldsymbol{S} = \boldsymbol{S}^I + \boldsymbol{S}^{II} \tag{6.1}$$

$\boldsymbol{S}^I$ and $\boldsymbol{S}^{II}$ denote 2nd Piola-Kirchhoff stress tensor in chains (I) and (II), respectively, and can be written in rate form as [2]:

$$\begin{aligned} \dot{\boldsymbol{S}}^{I} &= \boldsymbol{C}^{I} : \dot{\boldsymbol{e}} \\ \dot{\boldsymbol{S}}^{II} &= \boldsymbol{C}^{II} : \dot{\boldsymbol{e}} \\ \boldsymbol{e} &= \frac{1}{2}\left(\boldsymbol{F}^{T}\boldsymbol{F} - \boldsymbol{I}\right) \end{aligned} \tag{6.2}$$

in which $\boldsymbol{e}$ is the total Green-Lagrangian strain tensor and over-dot denotes time derivative. $\boldsymbol{F}$ and $\boldsymbol{I}$ are the deformation gradient tensor and the second order unit tensor, respectively. $\boldsymbol{C}^{I}$ and $\boldsymbol{C}^{II}$ are linear elastic tangent moduli for chains (I) and (II), respectively and are obtained as:

$$\boldsymbol{C}^{n}_{ijkl} = -\frac{\nu^{n}}{E^{n}}\delta_{ij}\delta_{kl} + \frac{1+\nu^{n}}{E^{n}}\left[\delta_{ik}\delta_{jl} + \delta_{il}\delta_{jk}\right] \qquad n = I, II \tag{6.3}$$

where ν and δ_{ij} are Poisson ratio and Kronecker delta, respectively. The inelastic rate of deformation, $\boldsymbol{d}_{p}$ can be obtained as:

$$\boldsymbol{d}_{p} = \frac{\boldsymbol{\tau}^{I}_{d}}{\eta} \tag{6.4}$$

in which $\boldsymbol{\tau}^{I}_{d}$ is the deviatoric Kirchhoff stress tensor and is given via:

$$\begin{aligned} \boldsymbol{\tau}^{I} &= \boldsymbol{F}\boldsymbol{S}^{I}\boldsymbol{F}^{T} \\ \boldsymbol{\tau}^{I}_{d} &= \boldsymbol{\tau}^{I} - \frac{1}{3}tr\left(\boldsymbol{\tau}^{I}\right) \end{aligned} \tag{6.5}$$

where tr denotes the trace of a matrix. The viscosity η is calculated via

$$\begin{aligned} \eta &= \eta_{0}\frac{\tau/\tau_{0}}{\sinh\left(\tau/\tau_{0}\right)}exp\left(\frac{\mu p}{\tau_{0}}\right) \\ \tau &= \sqrt{\frac{1}{2}\boldsymbol{\tau}^{I}_{d} : \boldsymbol{\tau}^{I}_{d}}, \qquad p = \frac{1}{3}tr\left(\boldsymbol{\tau}^{I}_{d}\right) \end{aligned} \tag{6.6}$$

where η_{0}, τ_{0} and μ are material parameters. According to experimental observations [17, 19], one can write E^{I}, E^{II} and τ_{0} as functions of equivalent strain rate as[3]:

$$E^{I} = \alpha_{1}\dot{e}_{eq}^{\beta_{1}}, \qquad E^{II} = \alpha_{2}\dot{e}_{eq}^{\beta_{2}}, \qquad \tau_{0} = \alpha_{3}\dot{e}_{eq}^{\beta_{3}} \tag{6.7}$$

in which α_{i} and β_{i} (i=1, 2, 3) are material constants and the equivalent strain rate is calculated as: $\dot{e}_{eq} = \sqrt{\frac{2}{3}\dot{\boldsymbol{e}} : \dot{\boldsymbol{e}}}$. The flow rule (6.4) can be solved by applying a return mapping algorithm and spectral decomposition using local Newton-Raphson iteration (see G). The proposed model in total consists of 10 material parameters including ν^{I}, ν^{II}, μ, η_{0}, α_{i} and β_{i} (i=1, 2, 3) which can be found using experimental data at various strain rates.

---

[2] For branch (I), $\boldsymbol{F} = \boldsymbol{F}^{elastic}\boldsymbol{F}^{plastic}$ and equation (6.2a) are solved together with a flow rule.

[3] It should be noted that equation (6.4) controls the rate dependency of the inelastic response and equations (6.7) control the rate dependency of the elastic response and the yield stress.

6.3.2. Calculation of material parameters

In the present work, experimental data for CF 75 polymer is used which is reported in [17, 19]. The tension and compression tests are performed using a split Hopkinson bar apparatus. For the tension test a dogbone specimen with gauge length 10 (mm) and circular cross section with diameter 6 (mm) is used. For the compression test a cylindrical specimen with length 5 (mm) and diameter 10 (mm) is tested. For the numerical, cylindrical specimens with a diameter of 6 (mm) and length of 10 (mm) under tension and cylindrical speciemens with a diameter of 10 (mm) and length of 5 (mm) under compression are analyzed. The axisymmetric state is used for the numerical analysis. A constant velocity $\bar{V}$ is applied on the edge of specimens in the numerical analysis (figure 6.3). In order to account for incompressibility of the polymer material, Poisson ratio values can be chosen close to 0.5. For CF 75 polymer we set ν^{I}=ν^{II}=0.4. Parameter μ is taken equal to -5e-5 (MPa). The values for α_i and β_i for tension and compression are given in table 6.1. Figure 6.4 and 6.5 show the experimental and numerical stress-strain curves at different strain rates under tension and compression, respectively. It should be noted that for the tension test, the material parameters are obtained using the experimental data at rates 900, 1300 and 2200 (1/s). The results at the other strain rates are predicted using the proposed polymer model. For the compression test, the material parameters are calculated from the data at 1092, 2191 and 4334 (1/s) and the stress-strain curve at strain rate 5124 (1/s) is predicted using the polymer model.

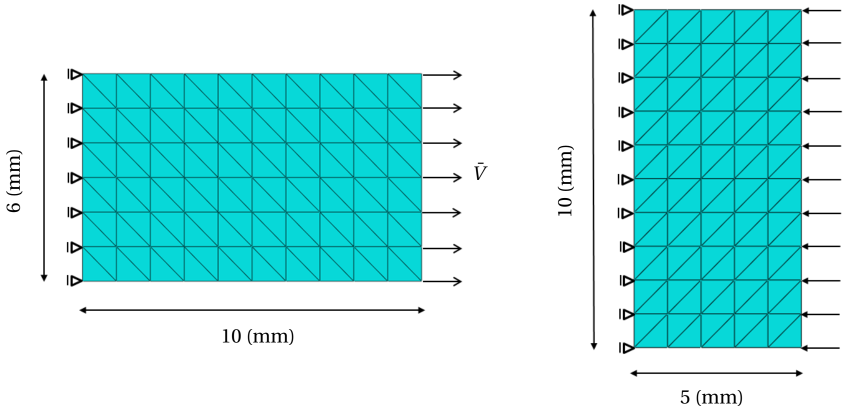

(a) Tension

(b) Compression

Figure 6.3: Numerical models for the tension and compression tests

Table 6.1: Material parameters

Parameters		Tension	Compression
α_1	(MPa)	20.6	1.31e-2
α_2	(MPa)	4.35	56.9
α_3	(MPa)	9.94e-4	0.771
β_1	(-)	0.55	1.43
β_2	(-)	0.50	0.23
β_3	(-)	1.31	0.39
ν^I	(-)	0.4	0.4
ν^{II}	(-)	0.4	0.4
μ	(MPa)	-5e-5	-5e-5
η_0	(MPa.s)	0.1	0.1

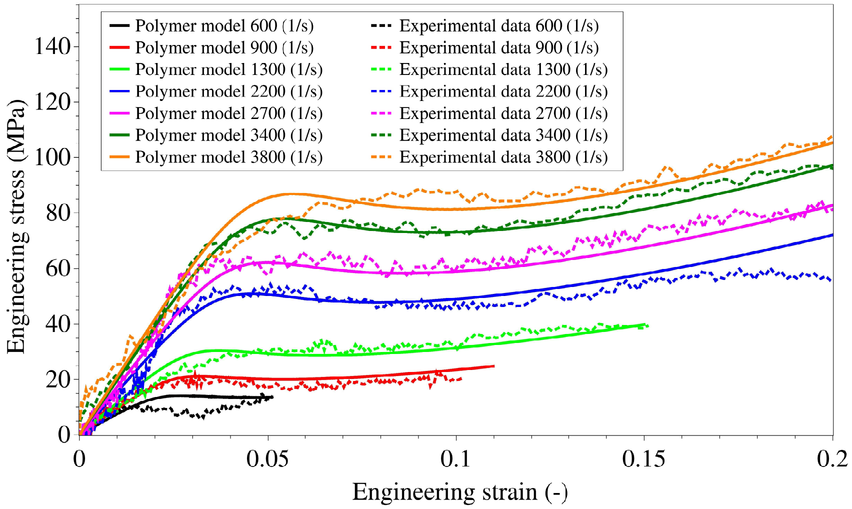

Figure 6.4: Numerical and experimental stress-strain curve for tension test at different strain rates

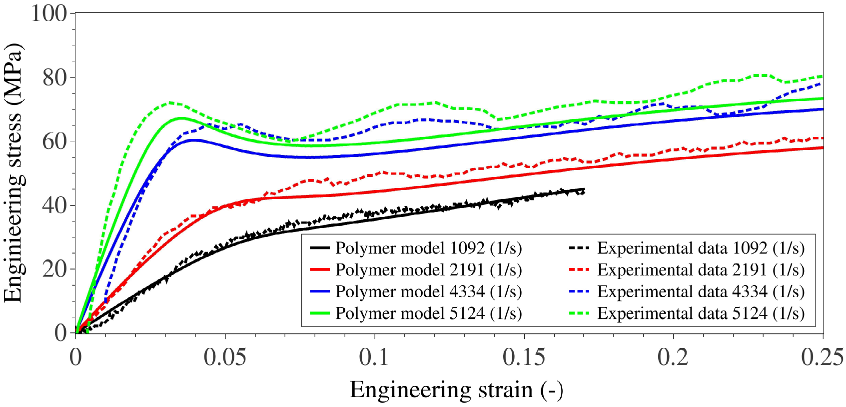

Figure 6.5: Numerical and experimental stress-strain curve for compression test at different strain rates

6.4. Failure mechanisms in glassy polymer materials

Two types of failure can be observed in the glassy polymers. Shear yielding and crazing. The competition between these two failure mechanisms determines the ductility or brittleness of the response of the polymer material. Under compression loading, the material undergoes large plastic deformations and localized shear yielding (formation of shear bands) occurs in a direction of 45° from the direction of maximum tensile stress. Under tension, limited shear yielding occurs and at a specific stress level crazing occurs due to the nucleation of micro voids in the direction normal to the maximum principle stress. Crazes can further widen and eventually break down which results in brittle fracture of the polymer material. From the experiments it has been observed that craze initiation is stress dependent [1, 76]. It has also been observed that craze initiation depends on the hydrostatic stress and the maximum principal stress. In the present work, craze initiation criteria developed by Sternstein et. al. [74] are utilized. For the plane stress state, these criteria can be expressed as:

$$\begin{cases} \frac{3}{2}S_m - \frac{1}{2}A + \frac{B}{6S_m} - S_1 \leq 0 \\ 0 < S_m < \frac{3}{2}S_1 \end{cases} \tag{6.8}$$

in which S_1 and S_m denote the maximum principle stress and the hydrostatic stress, respectively. A and B are temperature dependent material parameters. In the present work, the temperature is assumed to be constant during loading.
Material parameters A and B for the craze initiation criteria can be estimated using experiments. In [28], a intact bar and a notched-bar tension tests are used to

estimate the craze initiation parameters for PMMA. In the experimental tests it is observed that crazing initiates just prior to the peak load. In the present work due to the lack of experimental data for the CF 75, numerical analysis with the same geometries as in [28] are analyzed using the finite element method. Material properties for CF 75 are given in table 6.1. It has been assumed that at strain rate 600 (1/s), crazing initiates at the peak load. The intact bar and the notched bar are shown in figure 6.6. A constant velocity $\bar{V}$ is applied on the right edge. For the notched-bar, crazing initiates at the notch tip. In order to enforce the strain rate 600 (1/s) at the tip element for the notched-bar test, a constant velocity $\bar{V}$=3.11 (m/s) (which refers to a strain rate 490 (1/s)) is applied on the right edge of the notched-bar. The force-displacement curves for the intact bar tension test and the notched-bar tension test are shown in figure 6.7. The set of maximum principle stress and hydrostatic stress (S_1, S_m) at peak load for the intact bar test and the notched-bar test are (4.38, 13.13) (MPa) and (4.96, 11.38) (MPa), respectively. Inserting these sets of data in equations (6.8) and solving for A and B gives A=16.74 (MPa) and B=366.25 (MPa^2). These parameters can be used in equations (6.8) to evaluate craze initiation for CF 75 polymer material.

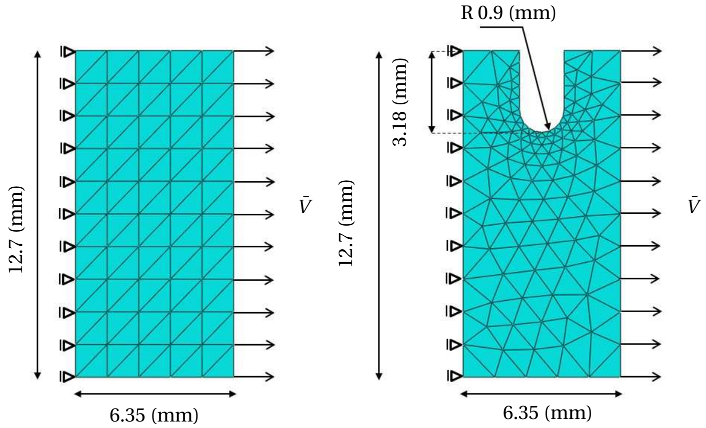

Figure 6.6: The intact bar (left) and the notched-bar (right) tension tests

In order to verify the calculated values for A and B, equation (6.8) is used to determine the initiation of crazing in the quasi-static tension test performed on the CF 75 polymer material in [19]. The quasi-static test has been conducted at a strain rate of 0.01/s using a servo-hydraulic Instron 8810 testing machine. In this experiment, it has been observed that fracture occurs at maximum stress 14 (MPa). In fact, the first crazes initiate at a stress value lower than 14 (MPa) and after craze widening fracture occurs. Since a uniaxial test is performed the specimen used is a intact bar, the hydrostatic stress can be estimated as $S_m=\frac{1}{3}\times 14=4.67$ (MPa). Figure 6.8 shows the craze initiation criteria for CF 75 polymer using the numerically calculated values for A and B. The set (S_1=14, S_m=4.57) (MPa) for the static test is also shown in figure 6.8 which is inside the crazing zone. This means that crazing initiates at a maximum stress lower than 14 (MPa) and after that fracture occurs which is consistent with the experimental test.

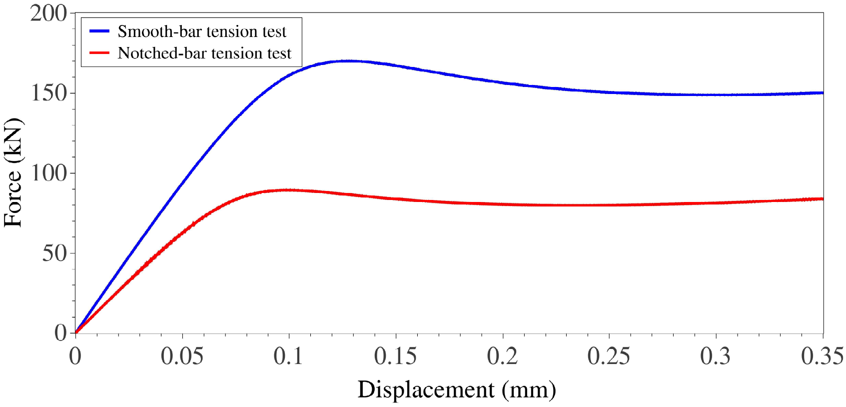

Figure 6.7: Reaction force for the intact bar and notched-bar tension tests

6.5. Verification of the polymer model: a glass particle-polymer tension test

In order to verify the proposed polymer material model, the numerical results obtained from the model are compared to experimental results in this section. Fan et. al. [18] performed a dynamic tensile test on a CF 75 polymer matrix with a single glass particle at various strain rates using a split Hopkinson bar apparatus. The test has been conducted on dogbone specimens with gauge length 10 (mm) and a circular cross section with a diameter of 6 (mm). A glass particle with a diameter of 3 (mm) is embedded in the polymer matrix. In the stress-strain curves reported in [18] for the polymer and the polymer with a single glass particle at strain rate 2700 (1/s), it has been observed that the glass particle does not affect the initial stiffness and for the polymer with the glass particle, yielding occurs at lower stress values compared to the single-phase polymer specimen. From these observations it can be concluded that debonding occurs between the glass particle and the polymer matrix at the first loading steps. The finite element model for the specimen is shown in figure 6.9. A cylindrical specimen is modeled and a axisymmetric state is assumed in the numerical analysis. The sample consists of a CF 75 polymer matrix (yellow), glass particle (green) and the interface (blue). The glass particle is modeled using a linear elastic material with Young's modulus $E^{particle}$=70 (GPa) and Poisson ratio ν=0.23. Debonding at the interface of the glass particle and the polymer matrix is modeled using a thin linear elastic layer (thickness=0.1 (mm)) with small Young's modulus compared to the polymer ($E^{interface}$=1e-9$\times E^{I}$). The experimental and numerical stress-strain curves for the tensile dynamic test at strain rate 2700 (1/s) for the glass particle-polymer

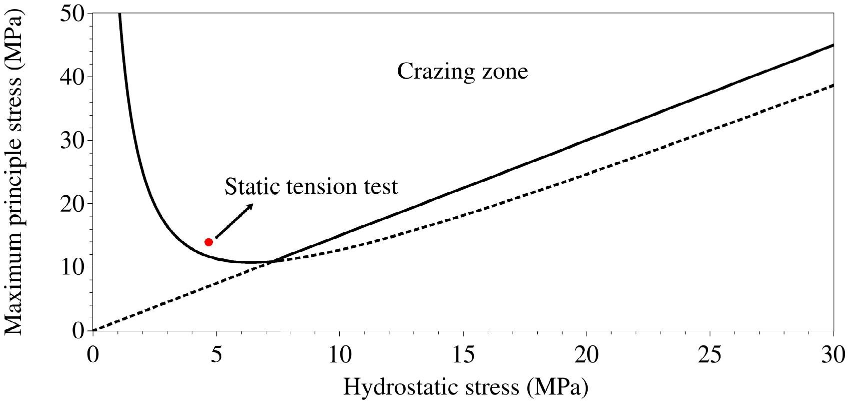

Figure 6.8: Craze initiation criteria

sample and the single-phase polymer sample are shown in figure 6.10. A comparison between the experimental and numerical stress-strain curves for the glass particle-polymer sample at different strain rates is depicted in figure 6.11. Good agreement between the numerical and the experimental results can be observed for strain rates from 700 (1/s) to 2700 (1/s). However, for the higher strain rates 3300(1/s) and 3800(1/s) the difference between the numerical and experimental results increases. This can be explained from the results in figure 6.12 which show the potential craze initiation zone for different strain rates at right edge displacement 0.07 (mm). The craze initiation zone increases with strain rate which means that the brittle response due to crazing (craze initiation, widening and final fracture) increases with strain rate. Therefore, at higher strain rates the deformation due to crazing contributes more to the total deformation. However, in the present polymer model only plastic deformations are taken into account and the deformations due to craze widening and final fracture are not considered. As a result, the present model overestimates the experimental test results at high strain rates.

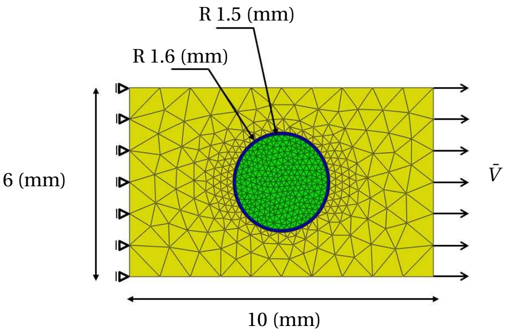

Figure 6.9: The glass particle-polymer tension test specimen

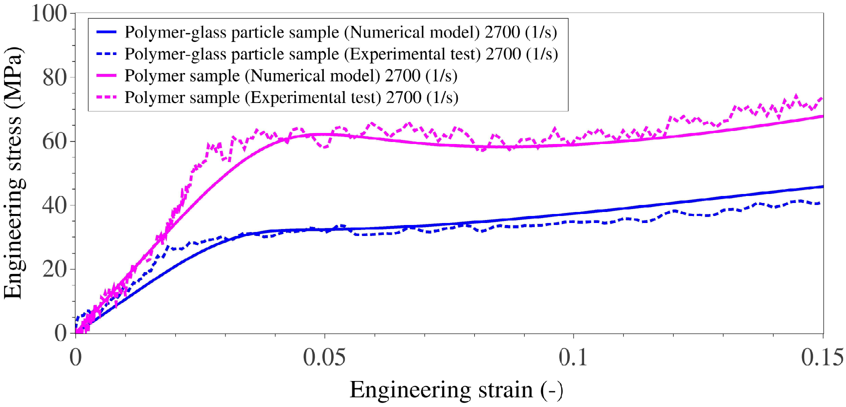

Figure 6.10: The glass particle-polymer sample and the single-phase sample tension tests

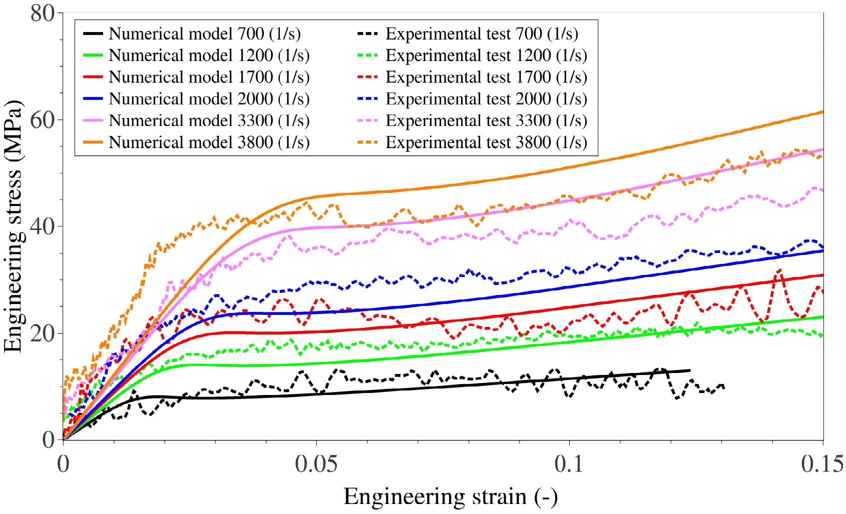

Figure 6.11: The glass particle-polymer tension tests at various strain rates

6.6. Numerical homogenization scheme

In a standard computational homogenization method, the macroscopic strain is assumed to be constant over the RVE. For the glass particle toughened polymers, strain localization can occur due to shear banding and/or cracking in the polymer matrix and as a result the assumption of constant strain is not valid. Therefore, the standard computational homogenization scheme cannot directly be used. In the

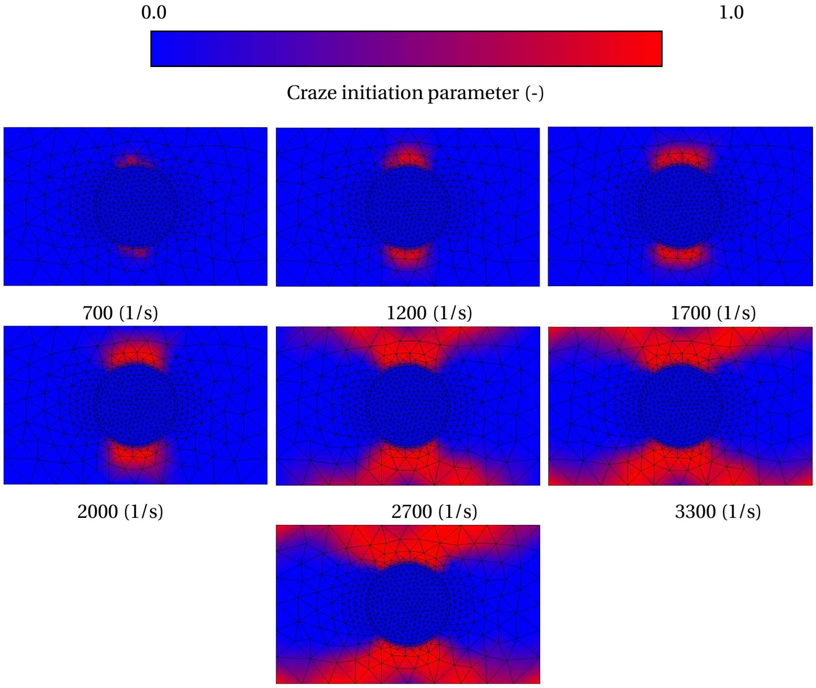

700 (1/s) 1200 (1/s) 1700 (1/s)

2000 (1/s) 2700 (1/s) 3300 (1/s)

3800 (1/s)

Figure 6.12: Craze initiation zone at different strain rates (no crazing: craze initiation parameter=0.0, crazing occurs: craze initiation parameter=1.0)

proposed numerical homogenization scheme, we assume that the macroscopic behavior of the glass particle-toughened polymer is governed by a similar constitutive law as the polymer material (see (6.3.1)). This constitutive law includes unknown parameters which can be obtained by solving an RVE problem. Therefore, the glass particle-toughened polymer constitutive law can be written as (see equations (6.2), (6.4) and (6.6)):

$$\begin{aligned}
&\dot{\overline{\boldsymbol{S}}} = \dot{\overline{\boldsymbol{S}}}^{I} + \dot{\overline{\boldsymbol{S}}}^{II}\\
&\dot{\overline{\boldsymbol{S}}}^{I} = \overline{\boldsymbol{C}}^{I} : \dot{\boldsymbol{e}}\\
&\dot{\overline{\boldsymbol{S}}}^{II} = \overline{\boldsymbol{C}}^{II} : \dot{\boldsymbol{e}}\\
&\overline{\boldsymbol{d}}_{p} = \frac{\overline{\boldsymbol{\tau}}_{d}^{I}}{\overline{\eta}}\\
&\overline{\eta} = \eta_{0} \frac{\overline{\tau}/\overline{\tau}_{0}}{\sinh\left(\overline{\tau}/\overline{\tau}_{0}\right)} exp\left(\frac{\mu \overline{p}}{\overline{\tau}_{0}}\right)
\end{aligned} \tag{6.9}$$

in which overbar denotes macroscopic quantities. In equation (6.9) parameters η_0 and μ are taken equal to the values of the plain polymer material. $\overline{\boldsymbol{C}}^{I}$, $\overline{\boldsymbol{C}}^{II}$ and $\overline{\tau}_0$ should now be computed from the RVE problem. Similar to the plain polymer material, the response of the particle/polymer system can be decomposed into an elasto-visco plastic response and the linear hardening response (see figure 6.1 and equations (6.9)). $\overline{\boldsymbol{C}}^{I}$ and $\overline{\tau}_0$ are the homogenized elastic tangent modulus and the homogenized yield strength for the elasto-visco plastic response, respectively. $\overline{\boldsymbol{C}}^{II}$ is the elastic tangent modulus for the hardening response. It should be noted that all three material parameters (and $\overline{\boldsymbol{C}}^{I}$, $\overline{\boldsymbol{C}}^{II}$ and $\overline{\tau}_0$) govern the response before the peak load (figure 6.1). On the other hand, as mentioned before, the standard computational homogenization scheme is valid before the softening part. $\overline{\boldsymbol{C}}^{I}$ and $\overline{\boldsymbol{C}}^{II}$ can now be computed from the RVE problem using the standard computational homogenization scheme as follows (see H). Two RVE problems should be solved:

I. RVE with linear elastic matrix with Young's modulus E^{I}

II. RVE with linear elastic matrix with Young's modulus E^{II}

At the converged state, the linearized form of RVE problems (I) and (II) can be written as $\boldsymbol{K}_{ii}^{(\alpha)}\delta\boldsymbol{u}_{ii}^{(\alpha)} = \delta\boldsymbol{f}_{ii}^{(\alpha)}$ (α=I, II). $\overline{\boldsymbol{C}}^{I}$ and $\overline{\boldsymbol{C}}^{II}$ can be obtained via (see (2.4.1)):

$$\overline{\boldsymbol{C}}^{\alpha} = \begin{bmatrix}\boldsymbol{H}_1 & \boldsymbol{H}_2 & \boldsymbol{H}_4\end{bmatrix}\left(\boldsymbol{K}_{bb}^{(\alpha)} - \boldsymbol{K}_{ba}^{(\alpha)}\left(\boldsymbol{K}_{aa}^{(\alpha)}\right)^{-1}\boldsymbol{K}_{ab}^{(\alpha)}\right)\begin{bmatrix}\boldsymbol{H}_1\\ \boldsymbol{H}_2\\ \boldsymbol{H}_4\end{bmatrix} \qquad (\alpha = I, II) \tag{6.10}$$

$\overline{\tau}_0$ can be computed from the RVE problem as follows: first, one can relate the peak stress σ_{max} (the stress value just before softening takes place in the stress-strain curve) to τ_0 for the polymer material as $\tau_0 = C_1\sigma_{max}^{C_2}$ in which C_1 and C_2 can be obtained using the stress-strain curves at different strain rates. Then, it can be assumed that the glass particle-toughened polymer obeys the same relation. The peak stress for the glass particle-toughened polymer $\overline{\sigma}_{max}$ can be obtained from the RVE problem solution. $\overline{\tau}_0$ can then be computed as $\overline{\tau}_0 = C_1\overline{\sigma}_{max}^{C_2}$. In the standard computational homogenization scheme, the constitutive law for the macro-scale model is taken as $\dot{\overline{\boldsymbol{S}}} = \overline{\boldsymbol{C}} : \dot{\overline{\boldsymbol{e}}}$ in which $\overline{\boldsymbol{C}}$ is computed via equation (6.10). Algorithms for the standard computational homogenization scheme and the proposed numerical homogenization scheme are given in boxes 1 and 2, respectively.

Box 1: The standard computational homogenization scheme.

1. Calculate $\dot{e}_{eq} = \sqrt{\frac{2}{3}\dot{\boldsymbol{e}}:\dot{\boldsymbol{e}}}$
2. Calculate E^{I}, E^{II} and τ_0 using equations (6.7)
3. Solving RVE problem
   3-1. Set matrix as a polymer material (section (6.3.1))
   3-2. Solve BVP for RVE: $\boldsymbol{K}_{ii}\delta\boldsymbol{u}_{ii} = \delta\boldsymbol{f}_{ii}$
   3-3. Compute macroscopic tangent moduli using equation (6.10)
4. Calculate macroscopic stress tensor as $\dot{\overline{\boldsymbol{S}}} = \overline{\boldsymbol{C}}:\dot{\overline{\boldsymbol{e}}}$

Box 2: The numerical homogenization scheme.

1. Calculate $\dot{e}_{eq} = \sqrt{\frac{2}{3}\dot{\boldsymbol{e}}:\dot{\boldsymbol{e}}}$
2. Calculate E^{I}, E^{II} and τ_0 using equations (6.7)
3. Solving two RVE problems (α=I, II)
   3-1. Set matrix as a elastic material with Young's modulus E^{α}
   3-2. Solve BVP for RVE: $\boldsymbol{K}^{(\alpha)}_{ii}\delta\boldsymbol{u}^{(\alpha)}_{ii} = \delta\boldsymbol{f}^{(\alpha)}_{ii}$
   3-3. Compute macroscopic tangent moduli using equation (6.10)
4. Obtain $\overline{\sigma}_{max}$ and calculate $\overline{\tau}_0 = C_1\overline{\sigma}^{C_2}_{max}$
5. Calculate macroscopic stress tensor using equations (6.9)

6.7. Verification of the numerical homogenization scheme

In this section two numerical examples are given in order to verify the proposed numerical homogenization scheme. In the first example a heterogeneous intact structure composed of glass particles and a CF 75 polymer matrix under dynamic loading is analyzed and the proposed numerical homogenization scheme is compared to the standard computational homogenization scheme and the DNS model. In the second example, the numerical homogenization scheme is used to model a notched heterogeneous structure.

6.7.1. Glass particle-polymer intact structure under dynamic loading

Figure 6.13 shows a heterogeneous structure consisting of glass particles (green) and a CF 75 polymer matrix (yellow). The material properties of the glass particle and the polymer material are the same as in the example given in section (6.5). A perfectly bonded interface between the particle and the polymer matrix is assumed. A constant velocity $\bar{V}$ is applied on the right edge. The multi-scale model is shown in Figure 6.14. The problem is solved using the proposed numerical homogenization scheme, the standard computational homogenization scheme and a DNS model.

Figure 6.15 shows the force versus displacement diagram for the DNS model, the standard computational homogenization scheme and the numerical homogenization scheme at strain rate 700 (1/s). As it can be observed in figure 6.15, all three models give similar results before softening occurs. After the peak load, in the softening part, the results obtained from the standard computational homogenization scheme are more ductile than those of the DNS model. However, the results obtained from the numerical homogenization scheme are in a good agreement with the DNS model results. The averaged plastic strain in x direction for the DNS model, the numerical homogenization model (over the whole area) and the homogenization model (over the RVE area) are plotted in figure 6.16. As it can be observed in this figure, the curves for the DNS model and the numerical homogenization scheme are the same which leads to the same overall stress tensor and reaction forces (figure 6.15). However these curves are below that of the standard computational homogenization method. Figure 6.17 depicts the distribution of the plastic strain for the DNS model and the standard computational homogenization scheme (over the RVE). It can be observed that for the DNS model, the plastic strain is localized over a smaller area compared to the standard homogenization method. Therefore, in the softening part, the results obtained with the standard homogenization method are more ductile compared to those of the DNS model.

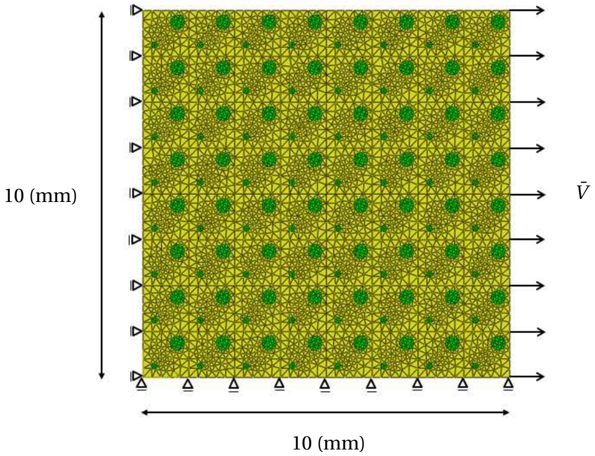

Figure 6.13: DNS model for the glass particle-polymer intact structure

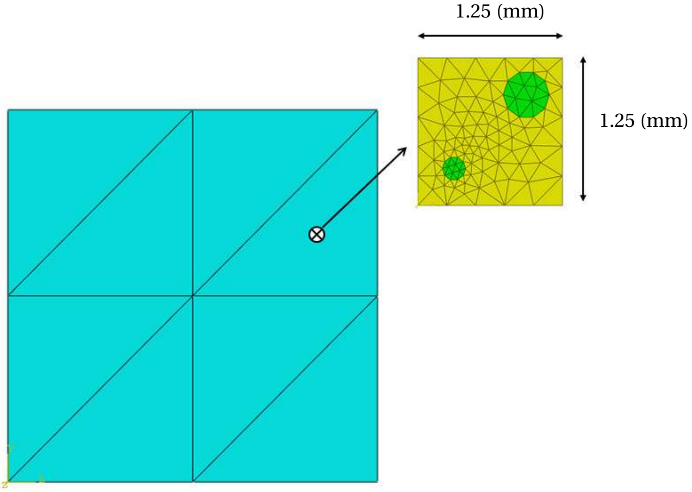

Figure 6.14: Multi-scale model for the glass particle-polymer intact structure

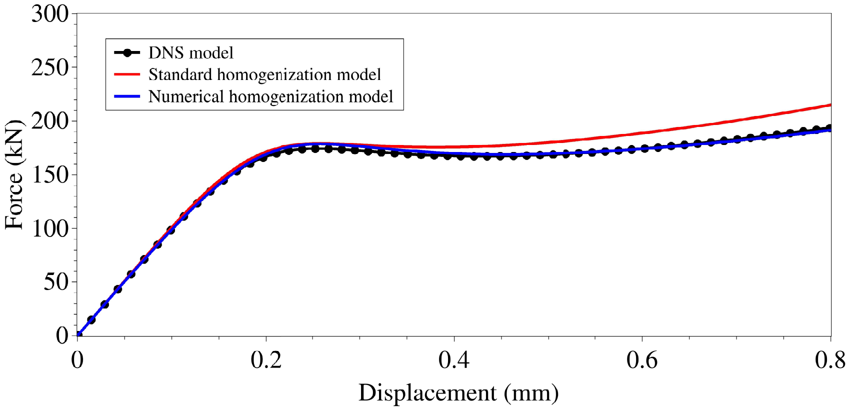

Figure 6.15: Force-displacement curves for the DNS model, the standard computational homogenization scheme and the numerical homogenization scheme at strain rate 700 (1/s)

6.7.2. Glass particle-polymer notched structure under dynamic loading

Figure 6.18 depicts a heterogeneous notched structure which is composed of similar glass particle-polymer material as in section (6.7.1). Figure 6.19 shows the multi-scale model for the problem. The force-displacement curves obtained from the DNS model and the numerical homogenization scheme are shown in figure 6.20 for different rates. A good agreement can be observed between the results.

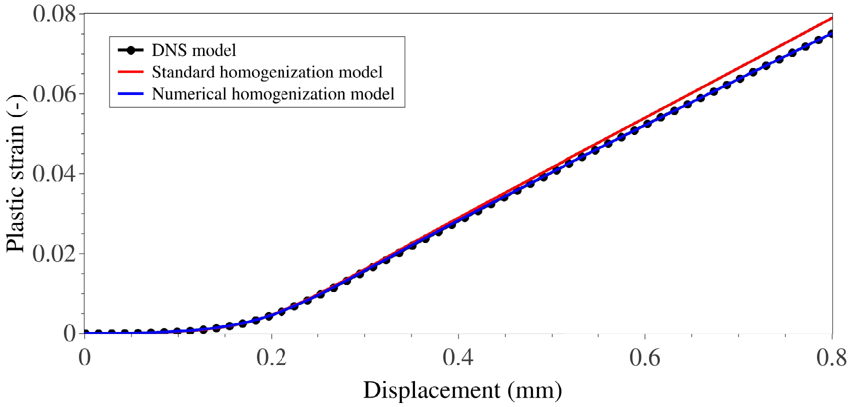

Figure 6.16: Plastic strain in x direction for the DNS, the standard computational homogenization scheme and the numerical homogenization scheme

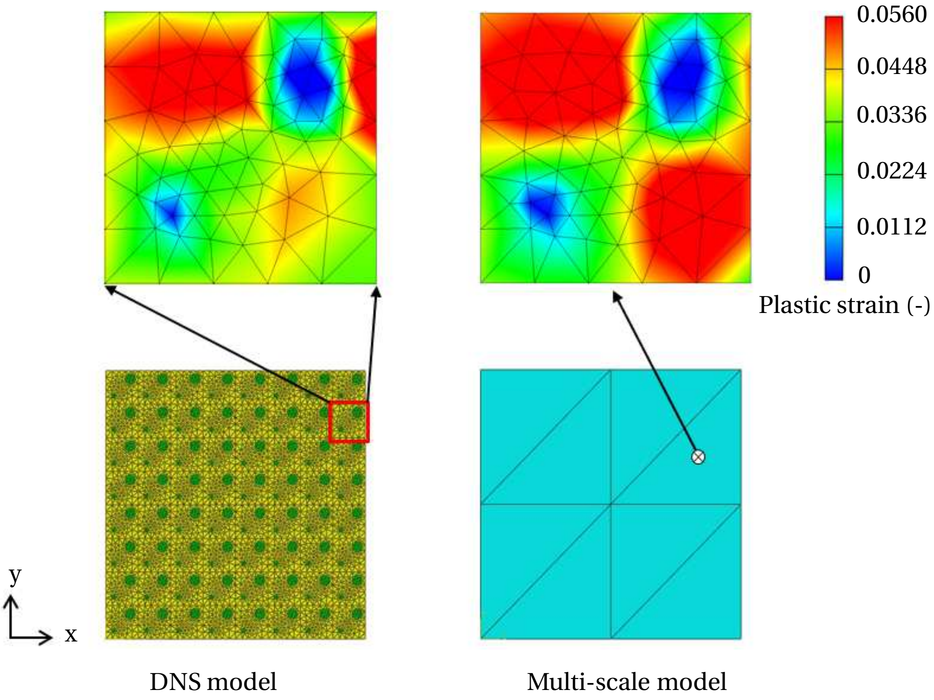

Figure 6.17: Distribution of the plastic strain in x direction for the DNS and the standard computational homogenization scheme

Craze initiation and direction in the macro-scale model element can be determined from the RVE problem and the craze initiation criteria (equation (6.8)).

However, in order to reduce the computational costs, macroscopic craze parameters can be obtained by solving the RVE problem once a priori. It is assumed that the macroscopic craze initiation criteria can be written as:

$$\frac{3}{2}\overline{S}_m - \frac{1}{2}A + \frac{B}{6\overline{S}_m} + d - \overline{S}_1 \leq 0 \tag{6.11}$$

in which A and B have the same values as the polymer material. d is a parameter which represents a shift in the craze initiation curve in y (S_1) direction (see figure 6.8). Parameter d can be computed using a set of $(\overline{S}_m, \overline{S}_1)$ which can be obtained from the RVE problem solution a priori. For the present problem, this set is calculated when 50% of the RVE area meets the craze initiation criteria [4]. For the strain rate 700 (1/s), these values can be obtained as ($\overline{S}_m$=4.46, $\overline{S}_1$=12.11) (MPa). By substituting these values in equation (6.11), parameter d can be obtained as 0.1035 (MPa).

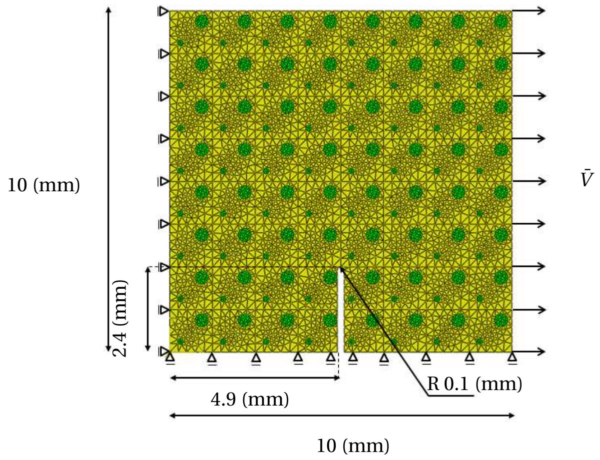

Figure 6.18: DNS model for the glass particle-polymer notched structure

---

[4] This value is arbitrary. However, since crazing occurs in the polymer matrix, one can use the volume fraction of particles as a minimum value. In order to have a better estimate of this value, one can compare a DNS model and multi-scale model for a very simple example and use the obtained value for more complex problems. For the present example, the particle volume fraction is 10% and a value of 50% is used.

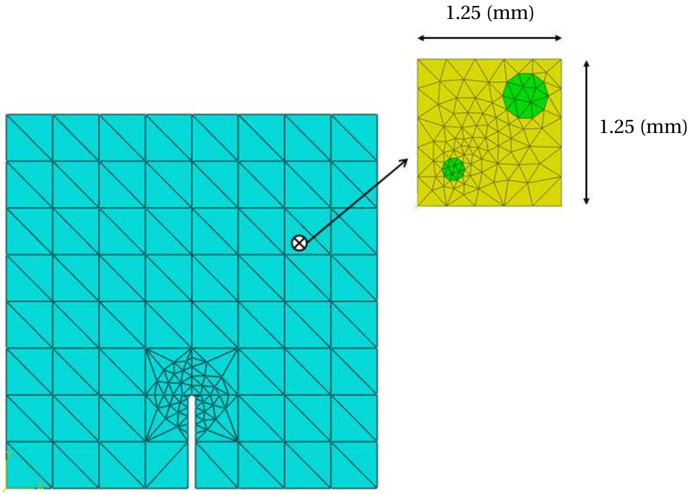

Figure 6.19: Multi-scale model for the glass particle-polymer notched structure

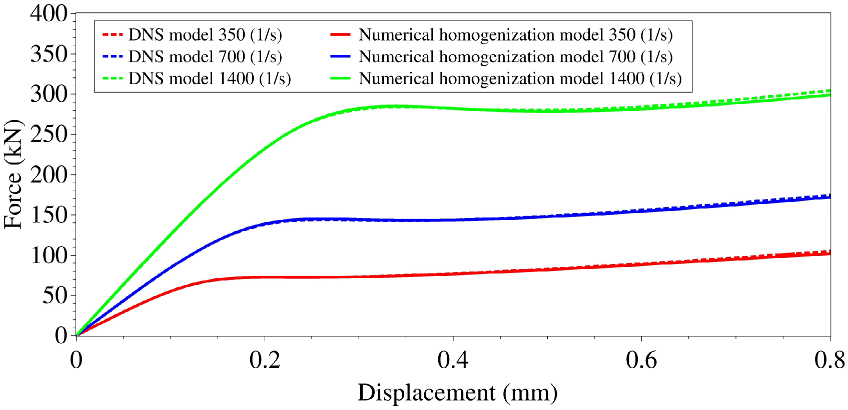

Figure 6.20: Force-displacement curves for the DNS model and the numerical homogenization scheme at different strain rates

Figures 6.21 and 6.22 show the development of the plastic shear strain and the craze initiation zone obtained from the DNS model and the numerical homogenization scheme at different times for strain rate 700 (1/s). The time step for this problem is 0.1 (μs). A good agreement between the multi-scale and DNS results can be observed in both figures. It can also be observed that crazing initiates before yielding in the polymer matrix.

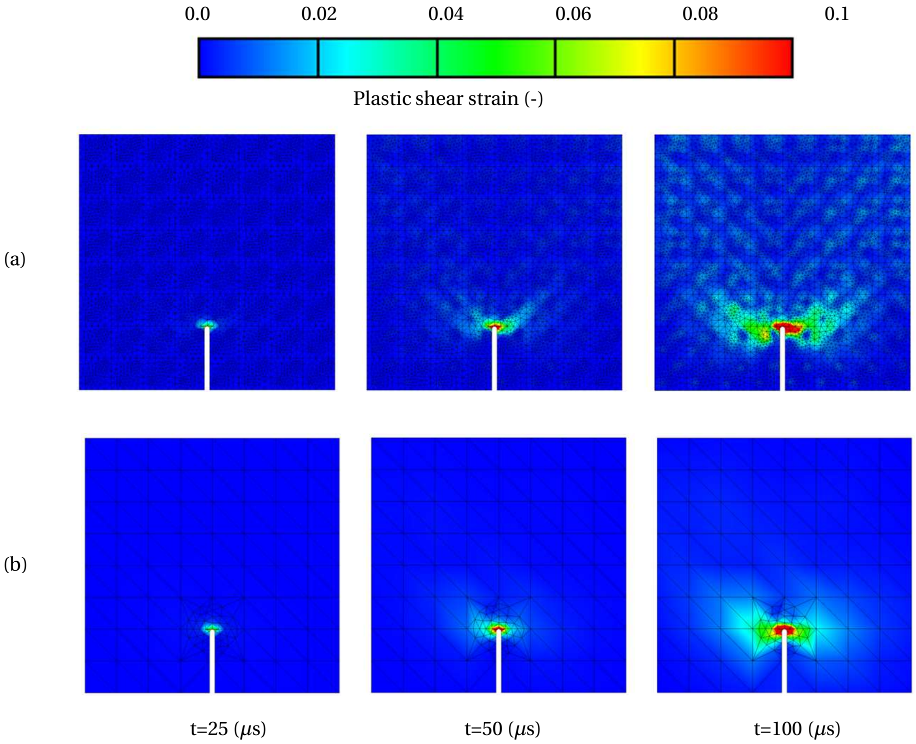

Figure 6.21: Plastic shear strain for (a) the DNS model and (b) the numerical homogenization scheme for strain rate 700 (1/s)

6.8. Conclusion

In this chapter, glass particle-toughened polymer materials are modeled using a numerical homogenization scheme. A constitutive law is formulated for the polymer material under high rate dynamic loading. The material model is validated using the experimental results for CF 75 polymer. The craze initiation criterion given in [74] is used to detect initiation of crazing and the corresponding craze initiation parameters for CF 75 are determined using numerical tests. The proposed numerical homogenization scheme is verified against the DNS model at different rates and a good agreement between the results is observed. It is also shown that when strain localization occurs, unlike the proposed numerical homogenization scheme, the standard computational homogenization scheme results in different plastic strain values and distribution compared to the DNS model which leads to an incorrect macroscopic response.

It should be mentioned that the proposed numerical homogenization scheme can be used as long as the assumption of similar behavior of the mixture and the plain polymer is valid. However, by adding large particles with high volume fractions to the polymer matrix, this assumption may be violated and the present numerical homogenization scheme cannot be used. In most practical applications, small

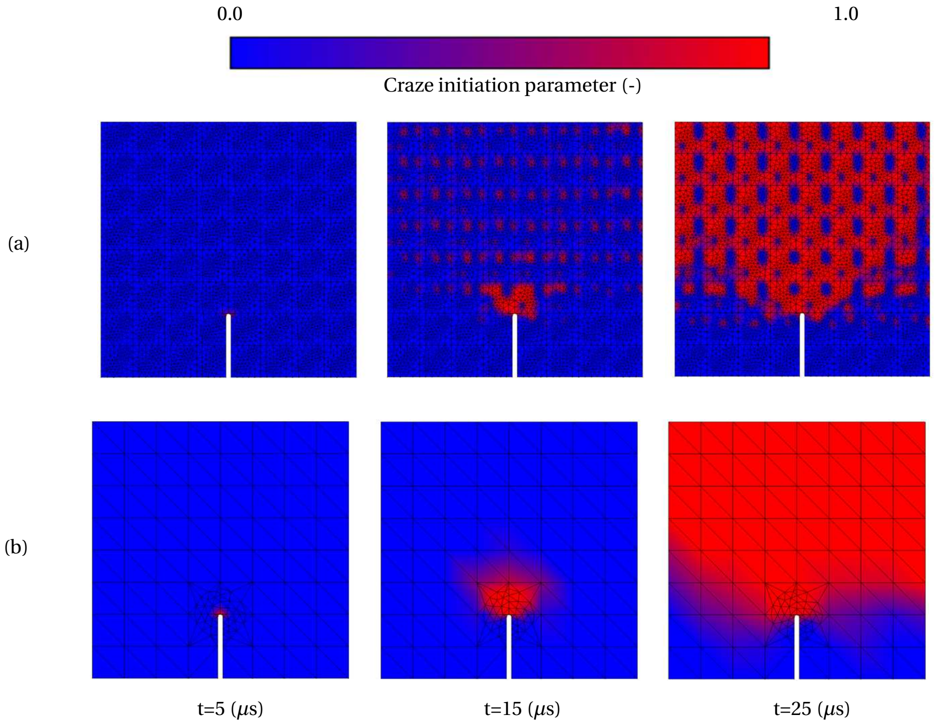

Figure 6.22: Craze initiation zone for (a) the DNS model and (b) the numerical homogenization scheme for strain rate 700 (1/s)

particles are used to enhance the fracture toughness of the polymer in which case the aforementioned assumption is valid.

7

Conclusions and recommendations

7.1. Concluding remarks

The macroscopic response of heterogeneous materials is to a large extent determined by the behavior of their micro-structure. Under dynamic loading conditions, a material undergoes large deformations and strains and complex damage processes occur at different length scales and time scales. Under these conditions, the macroscopic behavior depends not only on the material responses of the micro-structures but also on their local-scale inertia forces.

Homogenization-based multi-scale methods can be used to link the local-scale behavior to the macroscopic response. In order to model the macroscopic behavior properly in dynamic problems, the homogenization scheme should account for strain localizations (e.g., cracking and shear bands), rate effects, local-scale dynamic effects and large deformations and strains.

In this dissertation, homogenization methods have been developed for brittle and ductile materials under dynamic loading conditions considering aforementioned issues. The main contributions and conclusions of this thesis are:

- The continuous-discontinuous computational homogenization scheme is extended for dynamic problems to account for rate effects and local-scale dynamic effects (chapters (3) and (4)). It is shown that (1) a multi-scale dynamic problem can be solved by performing a dynamic analysis at the macro-scale while solving the RVE model as a quasi-static problem, (2) the effect of crack opening rate on the macro cohesive law can be taken into account by relating the material properties of the meso-scale model to the macro crack opening rate, (3) the dispersion effects due to local-scale inertia forces can be taken into account by introducing an additional body force into the macro-scale model problem, (4) the local-scale dynamic effects are negligible when the macroscopic wave length is significantly larger than the characteristic length of the RVE and (5) the results obtained from the multi-scale models are objective with respect to the RVE size.

- The computational efficiency of the computational homogenization schemes is improved using a computational continua model which requires no higher-order boundary conditions and extra degrees of freedom (chapter (5)). It is shown that (1) using this homogenization scheme, the reference solution (solution obtained using the DNS model) can be achieved by a significantly coarser macroscopic mesh compared to the standard computational homogenization scheme which leads to much lower computational cost and (2) the required homogenized properties for the computational continua can be obtained using computational procedures similar to the standard homogenization scheme.
- Finally, in chapter (6), a numerical homogenization scheme is developed for glass-particle/polymer systems. The advantages of this model are that (1) unlike the standard computational homogenization scheme, it is valid after localization occurs in the polymer matrix and (2) the required homogenized properties can be obtained a priori by solving two separate RVE problems (using a standard computational homogenization scheme) which makes the model computationally more effective than the continuous-discontinuous homogenization scheme.

In chapters (3) and (4), the developed multi-scale methods have been used for quasi-brittle materials. However, it should be noted that these multi-scale models can also be used in combination with other material models. For instance, the continuous-discontin-uous computational homogenization scheme can be used for modeling shear bands in ductile materials and the same formulation can be used to account for dispersion effects. The derived computational continua formulation which is used for hyperelastic materials in chapter (5) can also be used for other materials to reduce the computational cost. Furthermore, the numerical homogenization scheme developed in chapter (6) is based on the fact that the composite system and the plain matrix show similar behavior. Therefore, in order to use this scheme for other material models it is important to have experimental evidences (as exist for glass particle-polymer systems) which show this similarity.

7.2. Future work

In this thesis, the standard and the continuous-discontinuous computational homogenization schemes are extended for dynamic problems and an numerical homogenization scheme is also developed for glass particle-toughened polymer materials under dynamic loading. The proposed models in this dissertation can further be developed. A few suggestions for future work based on the presented models in this thesis are:

- All problems solved in this dissertation are two-dimensional multi-scale problems. The models can be formulated in general form for three-dimensional problems. However, in order to extend the multi-scale models for three-dimensional problems a few issues should be considered: (1) the choice of the boundary conditions imposed on the RVE is very important and affects the homogenized properties. Complex localization patterns may occur in a three-dimensional RVE which may require the modification of the boundary conditions shown in figure 2.1 in chapter (2) and the computational costs of three-dimensional problems are significantly higher than two-dimensional problems. Therefore, using computational cost reduction techniques for three-dimensional multi-scale problems is essential.

- In the rate-dependent multi-scale crack models (chapters (3) and (4)), only mode I is considered. However, the rate-dependent multi-scale models can be used for mode II and can also be modified for mixed mode loading. In order to generalize the rate-dependent crack model for the mixed mode, one can modify equation (3.13) as:

  $$t^M_{eff}\left([[u]]^M_{eff}, [[\dot{u}]]^M_{eff}\right) = \left[1 + c_1^* \,\mathrm{asinh}\left(\frac{[[\dot{u}]]^M_{eff}}{c_0^*}\right)\right] t^M_{0eff} \tag{7.1}$$

  where $[[u]]^M_{eff} = \sqrt{\beta^2 [[u]]^{M^2}_s + [[u]]^{M^2}_n}$ and $t^M_{eff} = \sqrt{\beta^{-2} t^{M^2}_s + t^{M^2}_n}$. In these equations subscripts n and s denote normal and shear components of macro crack opening (or traction), respectively. Equation (3.14) can be rewritten as:

  $$\kappa_I\left([[\dot{u}]]^M_{eff}\right) = \left[1 + c_1 \,\mathrm{asinh}\left(\frac{[[\dot{u}]]^M_{eff}}{c_0}\right)\right] \kappa_I^0 \tag{7.2}$$

  Then, the same analysis as given in figure 3.14 for different combinations of $[[u]]^M_s$ and $[[u]]^M_n$ can be used to relate c_0 and c_1 to c_0^* and c_1^*. The boundary conditions which are imposed on the RVE should also be modified for model II and mixed mode loading. For instance, as suggested in [54], one can apply a shear displacement at the right edge of the RVE (see figure 2.1) for mode II and a combination of mode I and mode II boundary conditions for the mixed mode problem.

- In chapter (6), only craze initiation is considered. After craze initiation, the contin-uous-discontinuous computational homogenization scheme which is based on the failure zone averaging method can be modified to obtain the cohesive law for craze widening. The cohesive law for crazing (initiation, widening and breakdown) is shown in figure 7.1. In order to obtain the cohesive law from the RVE problem, one needs to provide proper local-scale models for the widening process which can be an interesting topic for future research.

- The multi-scale models can also be extended to multi-physics problems. For example, to perform thermo-hydro-mechanical analysis in geomechanical materials. The concepts of failure zone averaging and treating the RVE model as a quasi-static problem in transient analysis are still valid. However, issues such as boundary conditions imposed on the RVE and the homogenization procedures should be properly modified.

- Computational efficiency of the multi-scale models can be more improved using computational cost reduction methods. For example, using parallel computing, applying model order reduction techniques [8] for both the macro-scale model and the RVE problem, precomputation of the RVE, applying the multi-scale methods only for the critical regions and using multi-time stepping (subcycling on RVE scale) [68].

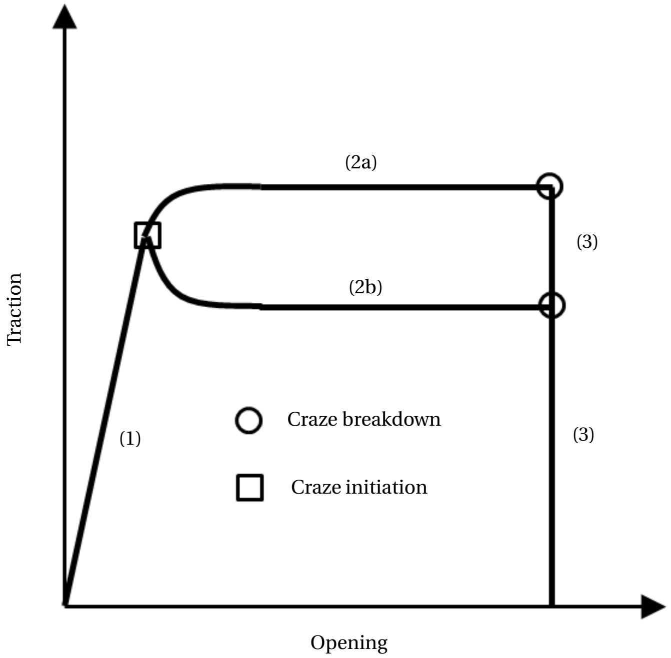

Figure 7.1: The cohesive law for crazing: (1) no crazing, (2) craze widening ((a) hardening response, (b) softening response)), (3) craze breakdown [16]

Appendices

A

Relations for obtaining K_{ij}^{pq} and f_{i}^{pq}

For anisotropic materials in plane stress, the constitutive law can be written in compact form $\sigma_i^m = C_{ij}^m \varepsilon_j^m (i, j = 1,2,6)$ and equation (4.13b) for a 2D problem can be written as follow:

$$\left\{\begin{aligned}
&\frac{\partial}{\partial x}\left(C_{11}^m\left(\frac{\rho^m}{\rho^M}+\frac{\partial h_1^{11}}{\partial x}\right)+C_{11}^m\frac{\partial h_2^{11}}{\partial y}\right)+\frac{\partial}{\partial y}\left(C_{66}^m\left(\frac{\partial h_1^{11}}{\partial y}+\frac{\partial h_2^{11}}{\partial x}\right)\right)=0\\
&\frac{\partial}{\partial x}\left(C_{66}^m\left(\frac{\partial h_1^{11}}{\partial y}+\frac{\partial h_2^{11}}{\partial x}\right)\right)+\frac{\partial}{\partial y}\left(C_{21}^m\left(\frac{\rho^m}{\rho^M}+\frac{\partial h_1^{11}}{\partial x}\right)+C_{22}^m\frac{\partial h_2^{11}}{\partial y}\right)=0
\end{aligned}\right. \tag{A.1a}$$

$$\left\{\begin{aligned}
&\frac{\partial}{\partial x}\left(C_{11}^m\frac{\partial h_1^{12}}{\partial x}+C_{12}^m\frac{\partial h_2^{12}}{\partial y}\right)+\frac{\partial}{\partial y}\left(C_{66}^m\left(\frac{\rho^m}{\rho^M}+\frac{\partial h_1^{12}}{\partial y}+\frac{\partial h_2^{12}}{\partial x}\right)\right)=0\\
&\frac{\partial}{\partial x}\left(C_{66}^m\left(\frac{\rho^m}{\rho^M}+\frac{\partial h_1^{12}}{\partial y}+\frac{\partial h_2^{12}}{\partial x}\right)\right)+\frac{\partial}{\partial y}\left(C_{12}^m\frac{\partial h_1^{12}}{\partial x}+C_{22}^m\frac{\partial h_2^{12}}{\partial y}\right)=0
\end{aligned}\right. \tag{A.1b}$$

$$\left\{\begin{aligned}
&\frac{\partial}{\partial x}\left(C_{12}^m\left(\frac{\rho^m}{\rho^M}+\frac{\partial h_2^{22}}{\partial y}\right)+C_{11}^m\frac{\partial h_1^{22}}{\partial x}\right)+\frac{\partial}{\partial y}\left(C_{66}^m\left(\frac{\partial h_1^{22}}{\partial y}+\frac{\partial h_2^{22}}{\partial x}\right)\right)=0\\
&\frac{\partial}{\partial x}\left(C_{66}^m\left(\frac{\partial h_1^{22}}{\partial y}+\frac{\partial h_2^{22}}{\partial x}\right)\right)+\frac{\partial}{\partial y}\left(C_{22}^m\left(\frac{\rho^m}{\rho^M}+\frac{\partial h_2^{22}}{\partial y}\right)+C_{12}^m\frac{\partial h_1^{22}}{\partial x}\right)=0
\end{aligned}\right. \tag{A.1c}$$

Inserting the discretized form $h_i^{pq} = \boldsymbol{N}\bar{\boldsymbol{h}}_i^{pq}$ into weak form (4.15), yields $\boldsymbol{K}_{\boldsymbol{ij}}^{\boldsymbol{pq}}$

and $\boldsymbol{f_i^{pq}}$ in equations (4.16):

$$\boldsymbol{K_{11}^{pq}}(p,q=1,2) = \int_{\Omega^m} \left(\frac{\partial \boldsymbol{N}^T}{\partial x} C_{11}^m \frac{\partial \boldsymbol{N}}{\partial x} + \frac{\partial \boldsymbol{N}^T}{\partial y} C_{66}^m \frac{\partial \boldsymbol{N}}{\partial y} \right) d\Omega^m - \int_{\Gamma^m} \left(\boldsymbol{N}^T C_{11}^m \frac{\partial \boldsymbol{N}}{\partial x} n_x + \boldsymbol{N}^T C_{66}^m \frac{\partial \boldsymbol{N}}{\partial y} n_y \right) d\Gamma^m \tag{A.2a}$$

$$\boldsymbol{K_{12}^{pq}}(p,q=1,2) = \int_{\Omega^m} \left(\frac{\partial \boldsymbol{N}^T}{\partial x} C_{12}^m \frac{\partial \boldsymbol{N}}{\partial y} + \frac{\partial \boldsymbol{N}^T}{\partial y} C_{66}^m \frac{\partial \boldsymbol{N}}{\partial x} \right) d\Omega^m - \int_{\Gamma^m} \left(\boldsymbol{N}^T C_{12}^m \frac{\partial \boldsymbol{N}}{\partial y} n_x + \boldsymbol{N}^T C_{66}^m \frac{\partial \boldsymbol{N}}{\partial x} n_y \right) d\Gamma^m \tag{A.2b}$$

$$\boldsymbol{K_{21}^{pq}}(p,q=1,2) = \int_{\Omega^m} \left(\frac{\partial \boldsymbol{N}^T}{\partial x} C_{66}^m \frac{\partial \boldsymbol{N}}{\partial y} + \frac{\partial \boldsymbol{N}^T}{\partial y} C_{21}^m \frac{\partial \boldsymbol{N}}{\partial x} \right) d\Omega^m - \int_{\Gamma^m} \left(\boldsymbol{N}^T C_{66}^m \frac{\partial \boldsymbol{N}}{\partial y} n_x + \boldsymbol{N}^T C_{21}^m \frac{\partial \boldsymbol{N}}{\partial x} n_y \right) d\Gamma^m \tag{A.2c}$$

$$\boldsymbol{K_{22}^{pq}}(p,q=1,2) = \int_{\Omega^m} \left(\frac{\partial \boldsymbol{N}^T}{\partial x} C_{66}^m \frac{\partial \boldsymbol{N}}{\partial x} + \frac{\partial \boldsymbol{N}^T}{\partial y} C_{22}^m \frac{\partial \boldsymbol{N}}{\partial y} \right) d\Omega^m - \int_{\Gamma^m} \left(\boldsymbol{N}^T C_{66}^m \frac{\partial \boldsymbol{N}}{\partial x} n_x + \boldsymbol{N}^T C_{22}^m \frac{\partial \boldsymbol{N}}{\partial y} n_y \right) d\Gamma^m \tag{A.2d}$$

$$\boldsymbol{f_1^{11}} = -\int_{\Omega^m} \frac{\partial \boldsymbol{N}^T}{\partial x} C_{11}^m \frac{\rho^m}{\rho^M} d\Omega^m + \int_{\Gamma^m} \boldsymbol{N}^T C_{11}^m \frac{\rho^m}{\rho^M} n_x d\Gamma^m \tag{A.2e}$$

$$\boldsymbol{f_2^{11}} = -\int_{\Omega^m} \frac{\partial \boldsymbol{N}^T}{\partial y} C_{21}^m \frac{\rho^m}{\rho^M} d\Omega^m + \int_{\Gamma^m} \boldsymbol{N}^T C_{21}^m \frac{\rho^m}{\rho^M} n_y d\Gamma^m \tag{A.2f}$$

$$\boldsymbol{f_1^{12}} = \boldsymbol{f_1^{21}} = -\int_{\Omega^m} \frac{\partial \boldsymbol{N}^T}{\partial y} C_{66}^m \frac{\rho^m}{\rho^M} d\Omega^m + \int_{\Gamma^m} \boldsymbol{N}^T C_{66}^m \frac{\rho^m}{\rho^M} n_y d\Gamma^m \tag{A.2g}$$

$$\boldsymbol{f_2^{12}} = \boldsymbol{f_2^{21}} = -\int_{\Omega^m} \frac{\partial \boldsymbol{N}^T}{\partial x} C_{66}^m \frac{\rho^m}{\rho^M} d\Omega^m + \int_{\Gamma^m} \boldsymbol{N}^T C_{66}^m \frac{\rho^m}{\rho^M} n_x d\Gamma^m \tag{A.2h}$$

$$\boldsymbol{f_1^{22}} = -\int_{\Omega^m} \frac{\partial \boldsymbol{N}^T}{\partial x} C_{12}^m \frac{\rho^m}{\rho^M} d\Omega^m + \int_{\Gamma^m} \boldsymbol{N}^T C_{12}^m \frac{\rho^m}{\rho^M} n_x d\Gamma^m \tag{A.2i}$$

$$\boldsymbol{f_2^{22}} = -\int_{\Omega^m} \frac{\partial \boldsymbol{N}^T}{\partial y} C_{22}^m \frac{\rho^m}{\rho^M} d\Omega^m + \int_{\Gamma^m} \boldsymbol{N}^T C_{22}^m \frac{\rho^m}{\rho^M} n_y d\Gamma^m \tag{A.2j}$$

B

Relations for obtaining dispersive curves

For a one-dimensional macro-scale problem, the equation of motion reads:

$$C_{11}^M \frac{d^2 u^M}{dx^2} + D \frac{d^2 \ddot{u}^M}{dx^2} = \rho^M \ddot{u}^M \tag{B.1}$$

Considering a harmonic wave $u^M = u_0^M e^{ik(x-vt)}$ (k is the wave number), one obtains:

$$-C_{11}^M + Dk^2 v^2 = -\rho^M v^2 \tag{B.2}$$

By solving (B.2) for v:

$$v = \sqrt{\frac{C_{11}^M}{\rho^M + k^2 D}} \tag{B.3}$$

The exact dispersion equation is given in [23]:

$$\cos(kl) = \cos(k_1 l_1)\cos(k_2 l_2) - \frac{1}{2}\left(\frac{z_1}{z_2} + \frac{z_2}{z_1}\right)\sin(k_1 l_1)\sin(k_2 l_2) \tag{B.4}$$

where $l_i = \alpha_i l$, $z_i = \sqrt{C_{11(i)}^M \rho_i}$, $k_i = \sqrt{\rho_i / C_{11(i)}^M}\omega^M$. ω^M and ω_0^M are angular frequencies for the dispersive model and the non-dispersive model, respectively. α_i denotes the volume fraction of material i.

For a two-dimensional problem, before the crack initiation, the discretized equation of motion reads:

$$(\boldsymbol{M}^M + \boldsymbol{m}_D^M)\ddot{\boldsymbol{u}}^M + \boldsymbol{K}^M \boldsymbol{u} = \boldsymbol{f}_{ext}^M \tag{B.5}$$

where $\boldsymbol{K^M}$ is the stiffness matrix for the macro-scale problem. Considering a free vibration ($\boldsymbol{f}^M_{ext} = 0$) and assuming a solution of the form $\boldsymbol{u}^M = \boldsymbol{u}^M_0 e^{i\omega t}$ results in:

$$(-\omega^2(\boldsymbol{M}^M + \boldsymbol{m}^M_D) + \boldsymbol{K})\boldsymbol{u}^M_0 = 0 \tag{B.6}$$

and ω can be found by solving this eigenvalue problem (B.6) and dispersive curves can be produced.

C

Stiffness matrices and force vectors for the updated Lagrangian finite element formulation

The stiffness matrices and the internal force vector can be obtained via:

$$\boldsymbol{K}_L^M = \int_{\Omega^M} \boldsymbol{B}_L^T \boldsymbol{C}^M \boldsymbol{B}_L d\Omega^M \tag{C.1}$$

$$\boldsymbol{K}_{NL}^M = \int_{\Omega^M} \boldsymbol{B}_{NL}^T \boldsymbol{S}^M \boldsymbol{B}_{NL} d\Omega^M \tag{C.2}$$

$$\boldsymbol{f}_{int}^M = \int_{\Omega^M} \boldsymbol{B}_L^T \boldsymbol{\sigma}^M d\Omega^M \tag{C.3}$$

where $\boldsymbol{B}_L$, $\boldsymbol{B}_{NL}$, $\boldsymbol{S}^M$ and $\boldsymbol{\sigma}^M$ are defined as:

$$\boldsymbol{B}_L = \begin{bmatrix} \frac{\partial \boldsymbol{N}_1}{\partial x} & 0 & \ldots & \frac{\partial \boldsymbol{N}_k}{\partial x} & 0 \\ 0 & \frac{\partial \boldsymbol{N}_1}{\partial y} & \ldots & 0 & \frac{\partial \boldsymbol{N}_k}{\partial y} \\ \frac{\partial \boldsymbol{N}_1}{\partial y} & \frac{\partial \boldsymbol{N}_1}{\partial x} & \ldots & \frac{\partial \boldsymbol{N}_k}{\partial y} & \frac{\partial \boldsymbol{N}_k}{\partial x} \end{bmatrix} \quad k = 1 \quad to \quad n \tag{C.4}$$

$$\boldsymbol{B}_{NL} = \begin{bmatrix} \frac{\partial \boldsymbol{N}_1}{\partial x} & 0 & \ldots & \frac{\partial \boldsymbol{N}_k}{\partial x} & 0 \\ \frac{\partial \boldsymbol{N}_1}{\partial y} & 0 & \ldots & \frac{\partial \boldsymbol{N}_k}{\partial y} & 0 \\ 0 & \frac{\partial \boldsymbol{N}_1}{\partial x} & \ldots & 0 & \frac{\partial \boldsymbol{N}_k}{\partial x} \\ 0 & \frac{\partial \boldsymbol{N}_1}{\partial y} & \ldots & 0 & \frac{\partial \boldsymbol{N}_k}{\partial y} \end{bmatrix} \quad k = 1 \quad to \quad n \tag{C.5}$$

$$\boldsymbol{S}^M = \begin{bmatrix} \sigma_{11}^M & \sigma_{12}^M & 0 & 0 \\ \sigma_{12}^M & \sigma_{22}^M & 0 & 0 \\ 0 & 0 & \sigma_{11}^M & \sigma_{12}^M \\ 0 & 0 & \sigma_{12}^M & \sigma_{22}^M \end{bmatrix} \tag{C.6}$$

$$\boldsymbol{\sigma}^M = \begin{bmatrix} \sigma_{11}^M \\ \sigma_{22}^M \\ \sigma_{12}^M \end{bmatrix} \tag{C.7}$$

in which n is the number of nodes per element.

D

Stiffness matrices and force vectors for the hybrid FE formulation

The stiffness matrices and the force vectors can be obtained via:

$$\boldsymbol{K}_{uu} = \int_{\Omega^m} \boldsymbol{B}_L^T \left(\boldsymbol{C}^m + P^m \left(\boldsymbol{I} \otimes \boldsymbol{I} - 2\mathbb{I} \right) \right) \boldsymbol{B}_L d\Omega^m + \int_{\Omega^m} \boldsymbol{B}_{NL}^T \boldsymbol{S}^m \boldsymbol{B}_{NL} d\Omega^m \tag{D.1}$$

$$\boldsymbol{K}_{uP} = \int_{\Omega^m} \boldsymbol{D} \boldsymbol{N}_P^T d\Omega^m \tag{D.2}$$

$$\boldsymbol{K}_{\theta\theta} = \int_{\Omega^m} \frac{d^2 \Psi^m_{vol}(\theta^m)}{d(\theta^m)^2} \boldsymbol{N}_P \boldsymbol{N}_P^T d\Omega^m \tag{D.3}$$

$$\boldsymbol{K}_{\theta P} = \int_{\Omega^m} \boldsymbol{N}_P \boldsymbol{N}_P^T d\Omega^m \tag{D.4}$$

$$\boldsymbol{K}_{Pu} = \int_{\Omega^m} \boldsymbol{N}_P \boldsymbol{D}^T d\Omega^m \tag{D.5}$$

$$\boldsymbol{K}_{P\theta} = \int_{\Omega^m} \frac{1}{J} \mathbf{N}_P \boldsymbol{N}_P^T d\Omega^m \tag{D.6}$$

$$\boldsymbol{F}_u = \boldsymbol{F}^m_{ext} - \int_{\Omega^m} \boldsymbol{B}_L^T \boldsymbol{\sigma}^m d\Omega^m \tag{D.7}$$

$$\boldsymbol{F}_\theta = \int_{\Omega^m} \boldsymbol{N}_P \left(\frac{d\Psi^m_{vol}(\theta)}{d\theta^m} - P^m \right) d\Omega^m \tag{D.8}$$

$$\boldsymbol{F}_P = \int_{\Omega^m} \boldsymbol{N}_P \left(J - \theta^m \right) d\Omega^m \tag{D.9}$$

$\boldsymbol{N}_P$ is a matrix of shape functions and matrix $\boldsymbol{D}$ is defined as:

$$\boldsymbol{D} = \begin{bmatrix} \frac{\partial \boldsymbol{N}_1}{\partial x} & \frac{\partial \boldsymbol{N}_2}{\partial x} & \cdots & \frac{\partial \boldsymbol{N}_k}{\partial x} \\ \frac{\partial \boldsymbol{N}_1}{\partial y} & \frac{\partial \boldsymbol{N}_2}{\partial y} & \cdots & \frac{\partial \boldsymbol{N}_k}{\partial y} \end{bmatrix} \qquad k = 1 \quad to \quad n \tag{D.10}$$

where n is the number of nodes of each element.

E

Deriving the macro-scale stress tensors

The weak form of the macro-scale problem can be written as:

$$\int_{\Omega^\zeta} w_i^M \frac{\partial P^\zeta_{ik}}{\partial X^M_k} d\Omega^\zeta = \sum_{I=1}^{k} \int_{\Omega^m} \hat{w} \frac{\partial w_i^M}{\partial X^m_k} P^\zeta_{ik} d\Omega^m = 0 \tag{E.1}$$

where w_i^M is the macroscopic test function. After inserting equation (5.27) into (E.1) and assuming $\hat{w}\frac{\partial w_i^M}{\partial X_j^m} = \alpha_{ij} + \beta^x_{ij} X^m + \beta^y_{ij} Y^m$, condition $\int_{\Omega^m} \hat{w}\frac{\partial w_i^M}{\partial X_k^m} P^*_{ik} d\Omega^m = 0$ is enforced which gives:

$$\int_{\Omega^m} \left(\alpha_{ij} + \beta^x_{ij} X^m + \beta^y_{ij} Y^m\right)\left(P^\zeta_{ij} - \bar{P}^M_{ij} - Q^M_{xij} X^m - Q^M_{yij} Y^m\right) d\Omega^m = 0 \tag{E.2}$$

Equation (E.2) leads to the system of equations below:

$$\begin{cases} a_0 \bar{\boldsymbol{P}}^M + b_x \boldsymbol{Q}^M_x + b_y \boldsymbol{Q}^M_y = \int_{\Omega^m} \boldsymbol{P}^\zeta d\Omega^m \\ b_x \bar{\boldsymbol{P}}^M + c_{xx} \boldsymbol{Q}^M_x + c_{xy} \boldsymbol{Q}^M_y = \int_{\Omega^m} X^m \boldsymbol{P}^\zeta d\Omega^m \\ b_y \bar{\boldsymbol{P}}^M + c_{xy} \boldsymbol{Q}^M_x + c_{yy} \boldsymbol{Q}^M_y = \int_{\Omega^m} Y^m \boldsymbol{P}^\zeta d\Omega^m \end{cases} \tag{E.3}$$

where

$$\begin{gathered} a_0 = \int_{\Omega^m} d\Omega^m = |\Omega^m|, b_x = \int_{\Omega^m} X^m d\Omega^m = 0, b_y = \int_{\Omega^m} Y^m d\Omega^m = 0 \\ c_{xx} = \int_{\Omega^m} \left(X^m\right)^2 \Omega^m = \frac{l_x^2 |\Omega^m|}{12}, c_{yy} = \int_{\Omega^m} \left(Y^m\right)^2 d\Omega^m = \frac{l_y^2 |\Omega^m|}{12}, c_{xy} = \int_{\Omega^m} X^m Y^m d\Omega^m = 0 \end{gathered} \tag{E.4}$$

Inserting (E.4) into (E.3), $\bar{\boldsymbol{P}}^M$, $\boldsymbol{Q}^M_x$ and $\boldsymbol{Q}^M_y$ can be obtained as given in equation (5.28).

F

Calculation of matrices used for computing macroscopic tensors

Matrices $\tilde{\boldsymbol{P}}^M$, $\tilde{\boldsymbol{Q}}_x^M$, $\tilde{\boldsymbol{Q}}_y^M$, $\boldsymbol{G1}$, $\boldsymbol{G2}$, $\boldsymbol{G3}$ and $\boldsymbol{G4}$ can be obtained via:

$$\tilde{\boldsymbol{P}}^M = \boldsymbol{H}_i \boldsymbol{f}_i \tag{F.1}$$

$$\tilde{\boldsymbol{Q}}_x^M = \boldsymbol{X}\boldsymbol{H}_i \boldsymbol{f}_i \tag{F.2}$$

$$\tilde{\boldsymbol{Q}}_y^M = \boldsymbol{Y}\boldsymbol{H}_i \boldsymbol{f}_i \tag{F.3}$$

$$\begin{aligned}
\boldsymbol{G}_1 &= \begin{bmatrix} 1 & 0 & 0 & 0 \\ 0 & 2 & 0 & 0 \\ 0 & 0 & 0 & 1 \\ 0 & 0 & 0 & 1 \end{bmatrix} \qquad \boldsymbol{G}_2 = \begin{bmatrix} 0 & 0 & 0 & 0 \\ 0 & 0 & -1 & 0 \\ 0 & 0 & 0 & 0 \\ 0 & 0 & 0 & 0 \end{bmatrix} \\
\boldsymbol{G}_3 &= \begin{bmatrix} 0 & 0 & 0 & -1 \\ 0 & 0 & 0 & 0 \\ 0 & 0 & 0 & 0 \\ 0 & 0 & 0 & 0 \end{bmatrix} \qquad \boldsymbol{G}_4 = \begin{bmatrix} 2 & 0 & 0 & 0 \\ 0 & 1 & 0 & 0 \\ 0 & 0 & 1 & 0 \\ 0 & 0 & 1 & 0 \end{bmatrix}
\end{aligned} \tag{F.4}$$

In equations (F.1)-(F.3), i denotes the boundary nodes. For the RVE shown in figure 5.1, the periodic boundary condition can be written as:

$$\begin{aligned}
\boldsymbol{u}_{\Gamma_T}^m - \boldsymbol{u}_{\Gamma_B}^m &= \boldsymbol{u}_4^m - \boldsymbol{u}_1^m \\
\boldsymbol{u}_{\Gamma_R}^m - \boldsymbol{u}_{\Gamma_L}^m &= \boldsymbol{u}_2^m - \boldsymbol{u}_1^m
\end{aligned} \tag{F.5}$$

Nodes (1), (2) and (4) are called controlling nodes. Using the equations given in (F.5) for the periodic boundary condition, matrices $\boldsymbol{H}_i$, $\boldsymbol{XH}_i$, $\boldsymbol{YH}_i$ and $\boldsymbol{f}_i$ are calculated only for the controlling nodes that is i=1, 2, and 4. Matrices $\boldsymbol{H}_i$, $\boldsymbol{XH}_i$ and $\boldsymbol{YH}_i$ are defined as:

$$\boldsymbol{H}_i = \begin{bmatrix} X_i^m & 0 \\ 0 & Y_i^m \\ Y_i^m & 0 \\ 0 & X_i^m \end{bmatrix}, \ \boldsymbol{XH}_i = \begin{bmatrix} (X_i^m)^2 & 0 \\ 0 & X_i^m Y_i^m \\ X_i^m Y_i^m & 0 \\ 0 & (X_i^m)^2 \end{bmatrix}, \ \boldsymbol{YH}_i = \begin{bmatrix} X_i^m Y_i^m & 0 \\ 0 & (Y_i^m)^2 \\ (Y_i^m)^2 & 0 \\ 0 & X_i^m Y_i^m \end{bmatrix} \tag{F.6}$$

G

Integration of the flow rule

Integration of the flow rule given in (6.4) and development of a return mapping algorithm can be carried out following the work of [64]. The inelastic rate of deformation, $\boldsymbol{d}_p$ can be defined as the Lie derivative of elastic Finger deformation $\boldsymbol{b}^e(=\boldsymbol{F}^e(\boldsymbol{F}^e)^T)$ ([63, 65]). Equation (6.4) can be written as

$$-\frac{1}{2}\mathscr{L}_v\boldsymbol{b}^e.\boldsymbol{b}^{e-1}=\frac{\boldsymbol{\tau}_d^I}{\eta} \tag{G.1}$$

in which $\mathscr{L}_v$ is the Lie derivative. In order to obtain the time-discrete solution of the above equation, a typical time sub-interval $[t_n,\ t_{n+1}]$ is considered. The integration of the flow rule is performed by an algorithm which involves an operator split of the material time derivative of $\boldsymbol{b}^e$ into an elastic predictor and an inelastic corrector

$$\dot{\boldsymbol{b}}_t^e=\underbrace{\boldsymbol{l}_t\boldsymbol{b}_t^e+\boldsymbol{b}_t^e\boldsymbol{l}_t^T}_{elastic}+\underbrace{\mathscr{L}_v\boldsymbol{b}_t^e}_{inelastic}\qquad\forall\,t\in[t_n,t_{n+1}] \tag{G.2}$$

where $\boldsymbol{l}=\dot{\boldsymbol{F}}\boldsymbol{F}^{-1}$ is the spatial velocity gradient. Inserting the value of $\mathscr{L}_v\boldsymbol{b}^e$ from (G.1) into (G.2), one obtains

$$\dot{\boldsymbol{b}}_t^e=\boldsymbol{l}_t\boldsymbol{b}_t^e+\boldsymbol{b}_t^e\boldsymbol{l}_t^T-\frac{\boldsymbol{\tau}_d^I}{\eta}\boldsymbol{b}_t^e \tag{G.3}$$

In the elastic trial state, plastic flow is frozen. Therefore we have $\mathscr{L}_v\boldsymbol{b}^{e\ tr}=\boldsymbol{0}$. Superscript tr denotes trial solution. In the inelastic corrector step, the current configuration is fixed at the position updated in the trial state. Therefore, the spatial velocity gradient is zero and equation (G.3) becomes

$$\dot{\boldsymbol{b}}_t^e=-\frac{\boldsymbol{\tau}_d^I}{\eta}\boldsymbol{b}^{e\ tr} \tag{G.4}$$

The differential equation (G.4) can be solved as

$$\boldsymbol{b}^{e\ tr} = exp\left(\frac{\boldsymbol{\tau}_d^I}{\eta}\Delta t\right)\boldsymbol{b}^e \tag{G.5}$$

in which Δt is the time step. The spectral decomposition of $\boldsymbol{b}^e$ and $\boldsymbol{\tau}_d^I$ are given as

$$\begin{aligned} \boldsymbol{b}^e &= \sum_a b_a^e \boldsymbol{n}^a \otimes \boldsymbol{n}^a \\ \boldsymbol{\tau}_d^I &= \sum_a \tau_{da}^I \boldsymbol{n}^a \otimes \boldsymbol{n}^a \end{aligned} \tag{G.6}$$

in which b_a^e=$(\lambda_a^e)^2$. λ_a^e and $\boldsymbol{n}^a$ are the principal elastic stretch values and directions of the principal axes. Due to isotropy, $\boldsymbol{b}^e$ and $\boldsymbol{\tau}_d$ share the same eigenspace. Inserting equations (G.6) into (G.5) gives

$$\boldsymbol{b}^{e\ tr} = \sum_a \left[exp\left(\frac{\tau_{ad}^I}{\eta}\Delta t\right)\left(\lambda_a^e\right)^2\right]\boldsymbol{n}^a \otimes \boldsymbol{n}^a \tag{G.7}$$

On the other hand, spectral decomposition of $\boldsymbol{b}^{e\ tr}$ is given as

$$\boldsymbol{b}^{e\ tr} = \sum_a \left(\lambda_a^{e\ tr}\right)^2 \boldsymbol{n}^{a\ tr} \otimes \boldsymbol{n}^{a\ tr} \tag{G.8}$$

Comparing (G.7) and (G.8) gives

$$\begin{aligned} &\left(\lambda_a^{e\ tr}\right)^2 = exp\left(-\Delta t\frac{\tau_{ad}^I}{\eta}\right)\left(\lambda_a^e\right)^2 \\ &\boldsymbol{n}^a = \boldsymbol{n}^{a\ tr} \end{aligned} \tag{G.9}$$

Taking logarithms of both sides of (G.9), one obtains

$$\epsilon_a^e = -\Delta t\left(\frac{\tau_{ad}^I}{2\eta}\right) + \epsilon_a^{e\ tr} \tag{G.10}$$

in which ϵ_a^e=$ln\lambda_a^e$. Equation (G.1) can be solved using local Newton-Raphson iteration. The stress-update algorithm is shown in box 3. In box 3, K denotes the bulk modulus.

Box 3: The stress-update algorithm for polymer model.

```
1. Calculate trial principal stretch values
   $d\boldsymbol{F}=\boldsymbol{F}_{n+1}\boldsymbol{F}_n^{-1}$
   $\boldsymbol{b}^{e\ tr}_{n+1}=d\boldsymbol{F}\boldsymbol{b}^{e\ tr}_n d\boldsymbol{F}^T$
   Find $\lambda_a^{e\ tr}$ and $\boldsymbol{n}^{a\ tr}$ from (G.8)
   $\epsilon_a^{e\ tr}=ln\lambda_a^{e\ tr}$
   $\lambda_a^{(0)}=\lambda_a^{e\ tr}$

2. Calculate residual
   $\epsilon_a^{e(i)}=ln\lambda_a^{(i)}$
   $J=\lambda_1^{(i)}\lambda_2^{(i)}\lambda_3^{(i)}$
   $e_a^p=\frac{1}{2}\left(\left(\lambda_a^{(i)}\right)^2-1\right)$ (principal Green-Lagrangian strain)
   $S_a^p=C_{ab}e_b^p$ (principal 2nd Piola-Kirchhoff stress)
   $S_{ad}^p=S_a^p\text{-}K(J-1)$
   Find $\tau^I_{ad}$ using (6.5)
   $r^{(i)}=\epsilon_a^e+\Delta t\left(\frac{\tau^I_{ad}}{2\eta}\right)-\epsilon_a^{e\ tr}$
   IF $|r|<TOL$ GOTO (4)

3. Update principal stretch values
   $\Delta\lambda_a=-r^{(i)}/\left(\frac{dr}{d\lambda_a}\right)^{(i)}$
   $\lambda_a^{(i+1)}=\lambda_a^{(i)}+\Delta\lambda_a$
   $i=i+1$ GOTO (2)

4. Calculate 2nd Piola-Kirchhoff stress
   Find $\boldsymbol{\tau}^I_d$ using (G.6b)
   $\boldsymbol{S}^I=\boldsymbol{F}^{-1}\boldsymbol{\tau}^I_d\boldsymbol{F}^{-T}+K(J-1)\boldsymbol{I}$
```

H

Calculation of the homogenized elastic tangent moduli from two RVE problems

Figure H.1a shows a one dimensional description of the problem. E^0 is the Young's modulus for the particle. The aim is to find homogenized stiffness values $\overline{C}^I$ and $\overline{C}^{II}$ (figure H.1c). For the model shown in figure H.1b, the equivalent stiffness can be written as

$$\overline{C} = \frac{E^0\left(E^I + E^{II}\right)}{E^I + E^{II} + E^0} \tag{H.1}$$

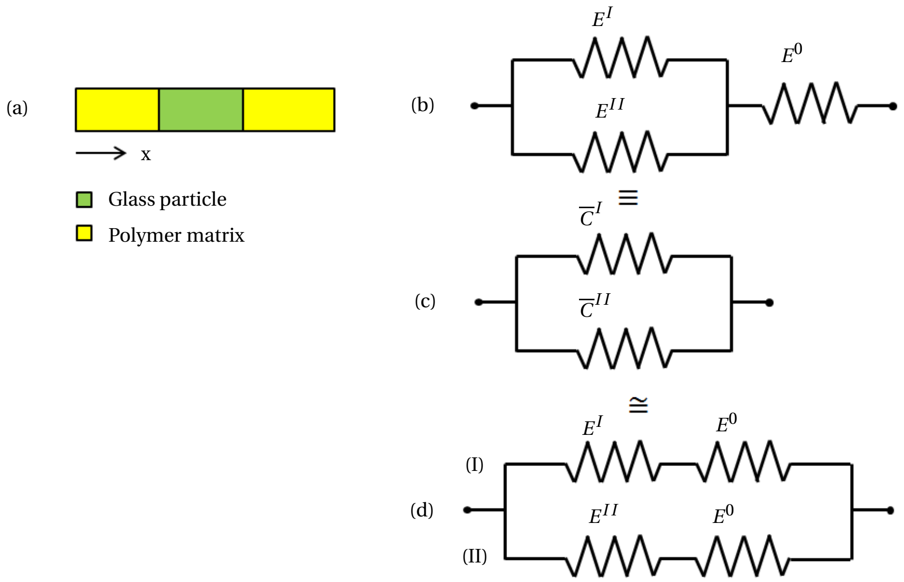

Figure H.1: One dimensional model for glass particle-toughened polymer matrix

Since the stiffness of the particle, E^0, is much larger than that of polymer matrix, $\frac{E^I E^{II}}{E^0}$ becomes orders of magnitude smaller than the stiffness values[1]. Therefore, equation (H.1) can be written as

$$\begin{aligned}\overline{C} &= \frac{E^0\left(E^I + E^{II} + 2\frac{E^I E^{II}}{E^0}\right)}{E^I + E^{II} + E^0 + \frac{E^I E^{II}}{E^0}} = \frac{E^I E^0\left(E^{II} + E^0\right) + E^{II} E^0\left(E^I + E^0\right)}{\left(E^T + E^0\right) + \left(E^{II} + E^0\right)} \\ &= \underbrace{\frac{E^I E^0}{E^I + E^0}}_{\overline{C}^I} + \underbrace{\frac{E^{II} E^0}{E^{II} + E^0}}_{\overline{C}^{II}}\end{aligned} \tag{H.2}$$

Equation (H.2) can also be obtained from the model shown in figure H.1d which means that the models shown in figures H.1b and H.1d are equivalent if $\frac{E^I E^{II}}{E^0}$ is much smaller than the stiffness values. In the model shown in figure H.1d, branches (I) and (II) represent two RVE problems: one RVE with linear elastic matrix with stiffness E^I and one with stiffness E^{II}. For two (or three) dimensional problems, the computational homogenization scheme can be used to solve these RVE problems.

---

[1] For the material properties used in this paper, at strain rate 3800 (1/s), $\frac{E^I E^{II}}{E^0}$=0.00147 (GPa). $\overline{C}$ can be calculated using equations (H.1) and (H.2) as 2.273 and 2.276 (GPa), respectively.

References

[1] A.S. Argon, J.G. Hannoosh, Initiation of crazes in polystyrene, Philos. Mag. 36 (1977) 1195–1216.

[2] H. Askes, A.H. Metrikine, A.V. Pichugin, T. Bennett, Four simplified gradient elasticity theories for the simulation of dispersive wave propagation, Philosophical magazine 88 (2008) 3415–3443.

[3] J.L. Auriault, Upscaling heterogeneous media by asymptotic expansions, J. Eng. Mech. 128(8) (2002) 817–822.

[4] K.J. Bathe, E. Ramm, E.L. Wilson, Finite element formulations for large deformation dynamic analysis, Int. J. Numer. Meth. Engng. 9 (1975) 353–386.

[5] Z. Bažant, Creep and damage in concrete, Materials science of concrete IV (1995) 355–389.

[6] T. Belytschko, H. Chen, J. Xu, G. Zi, Dynamic crack propagation based on loss of hyperbolicity and a new discontinuous enrichment, Int. J. Numer. Meth. Engng. 58 (2003) 1873–1905.

[7] T. Belytschko, S. Loehnert, J.H. Song, Multiscale aggregating discontinuities: A method for circumventing loss of material stability, Int. J. Numer. Meth. Engng 73 (2008) 869–894.

[8] B. Besselink, U. Tabak, A. Lutowska, N. Van de Wouw, H. Nijmeijer, D.J. Rixen, M.E. Hochstenbach, W.H.A. Schilders, A comparison of model reduction techniques from structural dynamics, numerical mathematics and systems and control, J. Sound Vibration 332(19) (2013) 4403–4422.

[9] G. Bolzon, R. Vitaliani, The blatz-ko material model and homogenization, Arch. Appl. Mech. 63 (1993) 228–241.

[10] V. Bouchart, M. Brieu, D. Kondo, M. Naït Abdelaziz, Implementation and numerical verification of a non-linear homogenization method applied to hyperelastic composites, Comput. Mater. Sci. 43 (2008) 670–680.

[11] C. Boutin, J.L. Auriault, Dynamic behavior of porous media saturated by a viscoelastic fluid. Application to bituminous concretes, Int. J. Engng Sci. 28(11) (1990) 1157–1181.

[12] W. Chen, J. Fish, A dispersive model for wave propagation in periodic heterogeneous media based on homogenization with multiple spatial and temporal scales, J. Appl. Mech. 68 (2001) 153–161.

[13] G. Cusatis, Strain-rate effects on concrete behavior, Int. J. Impact Eng. 38 (2011) 162–170.

[14] S. Eckardt, C. Konke, Adaptive damage simulation of concrete using heterogeneous multi-scale models, Journal of Algorithms and Computational Technology 2 (2008) 275–297.

[15] V.I. Erofeyev, Wave process in Solids with microstructure, Wolrd Scientific, 2003.

[16] R. Estevez, M.G.A. Tijssens, E. Van der Giessen, Modeling of the competition between shear yielding and crazing in glassy polymers, J. Mech. Phys. Solids 48 (2000) 2585–2617.

[17] J.T. Fan, J. Weerheijm, L.J. Sluys, Dynamic compressive mechanical response of a soft polymer material, Mater. Des. 79 (2015) 73–85.

[18] J.T. Fan, J. Weerheijm, L.J. Sluys, Glass interface effect on high-strain-rate tensile response of a soft polyurethane elastometric polymer material, Compos. Sci. Technol. 118 (2015) 55–62.

[19] J.T. Fan, J. Weerheijm, L.J. Sluys, High-strain-rate tensile mechanical response of a polyurethane elastomeric material, Polymer 65 (2015) 72–80.

[20] F. Feyel, J.L.D. Chaboche, Fe2 multiscale approach for modelling the elastoviscoplastic behaviour of long fibre sic/ti composite materials, Comput. Methods Appl. Mech. Engrg 183 (2000) 309–330.

[21] J. Fish, W. Chen, Higher-order homogenization of initial/boundary-value problem, J. Eng. Mech. 127(12) (2001) 1223–1230.

[22] J. Fish, W. Chen, N. Gakuji, Non-local dispersive model for wave propagation in heterogeneous media: one-dimensional case, Int. J. Numer. Meth. Engng. 54 (2002) 331–346.

[23] J. Fish, V. Filonova, S. Kuznetsov, Micro-inertia effects in nonlinear heterogeneous media, Int. J. Numer. Meth. Engng. 91 (2012) 1406–1426.

[24] J. Fish, S. Kuznetsov, Computational continua, Int. J. Numer. Meth. Engng. 84 (2010) 774–802.

[25] S. Forest, K. Sab, Cosserat overall modeling of heterogeneous materials, Mech. Res. Comm. 25(4) (1998) 449–454.

[26] L.B. Freund, Dynamic fracture mechanics. Cambridge Monographs on Mechanics and Applied Mathematics., Cambridge University Press, 1990.

[27] S.Y. Fu, X.Q. Feng, B. Lauke, Y.W. Mai, Effects of particle size, particle/matrix interface adhesion and particle loading on mechanical properties of particulate-polymer composites, Composites: Part B: engineering 39 (2008) 933–961.

[28] B.P. Gearing, L. Anand, On modeling the deformation and fracture response of glassy polymers due to shear-yieling and crazing, Int. J. Solids Struct. 41 (2004) 3125–3150.

[29] I.M. Gitman, H. Askes, E.C. Aifantis, Gradient elasticity with internal length and internal inertiabased on the homogenisation of a representative volume element, J. Mech. Behav. Mater. 18(1) (2007) 1–16.

[30] I.M. Gitman, H. Askes, L. Sluys, Coupled-volume multi-scale modelling of quasi-brittle material, Eur. J. Mech. – A/Solids 27(3) (2007) 302–327.

[31] I.M. Gitman, H. Askes, L. Sluys, Representative volume: Existence and size determination, Eng. Fract. Mech. 74(16) (2007) 2518–2534.

[32] P.A. Guidault, C. Allix, L. Champaney, J.P. Navarro, A two-scale approach with homogenization for the computation of cracked structures, Comput. Struct. 85(17-18) (2007) 1360–1371.

[33] R.N. Haward, G. Thackray, The use of a mathematical model to describe isothermal stress-strain curves in glassy thermoplastics, Proc. R. Soc. London A 302 (1968) 453–472.

[34] R. Hill, On constitutive macro-variables for heterogeneous solids at finite strain, Proc. R. Soc. Lond. 326 (1972) 131–147.

[35] A. Karamnejad, A. Ahmed, L.J. Sluys, A numerical homogenization scheme for glass particle-toughened polymers under dynamic loading, Journal of Multiscale Modelling (2016) (In press).

[36] A. Karamnejad, V.P. Nguyen, L.J. Sluys, A multi-scale rate dependent crack model for quasi-brittle heterogeneous materials, Eng. Fract. Mech. 104 (2013) 96–113.

[37] A. Karamnejad, L.J. Sluys, A dispersive multi-scale crack model for quasi-brittle heterogeneous materials under impact loading, Comput. Methods Appl. Mech. Engrg. 278 (2014) 423–444.

[38] A. Karamnejad, L.J. Sluys, A multi-scale scheme for modelling fracture under dynamic loading conditions, Key Eng. Mater. 627 (2014) 37–40.

[39] A. Karamnejad, L.J. Sluys, A new multi-scale scheme for modeling heterogeneous incompressible hyperelastic materials, Int. J. Numer. Meth. Engng (2015) (In press).

[40] V. Kouznetsova, W.A.M. Brekelmans, F.P.T. Baaijens, An approach to micro-macro modeling of heterogeneous materials, Comput. Mech. 27(1) (2001) 37–48.

[41] V.G. Kouznetsova, M.G.D. Geers, W.A.M. Brekelmans, Multi-scale second-order computational homogenization of multi-phase materials: a nested finite element solution strategy, Comput. Methods Appl. Mech. Engrg 193 (2004) 5525–5550.

[42] P. Ladevéze, A. Nouy, On a multiscale computational strategy with time and space homogenization for structural mechanics, Comput. Methods Appl. Mech. Engrg. 192 (2003) 3061–3087.

[43] P. Ladevéze, J.C. Passieux, D. Néron, The latin multiscale computational method and the proper generalized decomposition, Comput. Methods Appl. Mech. Engrg. 199 (2010) 1287–1296.

[44] J. Lemaitre, A Course on Damage Mechanics, Springer-Verlag, 1996.

[45] C.H. Liu, H. G., H.A. Mang, 3d finite element analysis of rubber-like materials at finite strains, Eng. Computations 11 (1994) 111–128.

[46] O. Lloberas-Valls, D.J. Rixen, A. Simone, L.J. Sluys, Multiscale domain decomposition analysis of quasi-brittle heterogeneous materials, Int. J. Numer. Meth. Engng 89(11) (2012) 1337–1366.

[47] S. Loehnert, T. Belytschko, A multiscale projection method for macro/microcrack simulations, Int. J. Numer. Meth. Engng 71 (2007) 1466–1482.

[48] J. Mazars, G. Pijaudier-Cabot, Continuum damage theory-application to concrete, J. Engng. Mech. Div. ASCE 115 (1989) 345–365.

[49] J. Mergheim, E. Kuhl, P. Steinmann, A finite element method for cohesive crack modelling, PMMA 4(1) (2004) 350–351.

[50] N. Moës, J. Dolbow, T. Belytschko, A finite element method for crack growth without remeshing, Int. J. Numer. Methods Engng. 46(1) (1999) 131–150.

[51] J. Moraleda, J. Segurado, J. Llorca, Finite deformation of porous elastomers: a computational micromechanics approach, Philos. Mag. 87(35) (2007) 5607–5627.

[52] S. Nemat-Nasser, M. Hori, Micromechanics: Overall properties of heterogeneous materials., Elsevier, 1999.

[53] V.P. Nguyen, O. Lloberas-Valls, M. Stroeven, L.J. Sluys, On the existence of representative volumes for softening quasi-brittle materials-a failure zone averaging scheme, Comput. Methods Appl. Mech. Engrg. 199 (2010) 3028–3038.

[54] V.P. Nguyen, O. Lloberas-Valls, M. Stroeven, L.J. Sluys, Homogenization-based multiscale crack modelling: From micro-diffusive damage to macro-cracks, Comput. Methods Appl. Mech. Engrg. 200 (2011) 1220–1236.

[55] V.P. Nguyen, M. Stroeven, L.J. Sluys, An enhanced continuous-discontinuous multiscale method for modeling mode-I cohesive failure in random heterogeneous quasi-brittle materials, Engrg. Fract. Mech. 79 (2012) 78–102.

[56] J. Oliver, M. Caicedo, E. Roubin, A.E. Huespe, J.A. Hernandez, Continuum approach to computational multiscale modeling of propagating fracture, Comput. Methods Appl. Mech. Engrg. 294 (2015) 384–427.

[57] R. Peerlings, R. De Borst, W. Brekelmans, J. De Vree, Gradient enhanced damage for quasi-brittle materials, Int. J. Numer. Methods Engrg. 39 (1996) 3391–3403.

[58] F. Perales, S. Bourgeois, A. Chrysochoos, Y. Monerie, Two field multi-body method for periodic homogenization in fracture mechanics of nonlinear heterogeneous materials, Eng. Fract. Mech. 75(11) (2008) 3378–3398.

[59] K. Pham, V.G. Kouznetsova, M.G.D. Geers, Transient computational homogenization for heterogeneous materials under dynamic excitation, J. Mech. Phys. Solids 61 (2013) 2125–2146.

[60] P. Ponte Castañeda, E. Tiberio, A second-order homogenization method in finite elesticity and applications to black-filled elastomers, Journal of the mechanics and physics of solids 48 (2000) 1389–1411.

[61] E. Samaniego, T. Belytschko, Continuum–discontinuum modelling of shear bands, Int. J. Numer. Methods Engng. 62 (2005) 1857–1872.

[62] E. Sanchez-Palencia, Non-homogeneous media and vibration theory. Lecture notes in physics 127, Springer-Verlag, Berlin, 1980.

[63] J.C. Simo, A framework for finite strain elastoplsticity based on maximum plastic dissipation and the multiplicative decomposition: part i. continuum formulation, Comput. Meth. Appl. Mech. Eng. 66 (1988) 199–219.

[64] J.C. Simo, Algorithms for static and dynamic multiplicative plasticity that preserve the classical return mapping schemes of the inifitesmal theory, Comput. Meth. Appl. Mech. Eng. 99 (1992) 61–112.

[65] J.C. Simo, M. Ortiz, A unified approach to finite deformation elastoplasticity based in the use of hyperelastic constitutive equations, Comput. Meth. Appl. Mech. Eng. 49 (1985) 222–235.

[66] J.C. Simo, R.L. Taylor, Quasi-incompressible finite elasticity in principal stretches. continuum basis and numerical algorithms, Comput. Methods Appl. Mech. Engrg. 85 (1991) 273–310.

[67] O. Van der Sluis, P. Schreurs, W. Brekelmans, H. Meijer, Overall behaviour of heterogeneous elastoviscoplastic materials: effect of microstructural modelling, Mech. Mater. 32(8) (2000) 449–462.

[68] P. Smolinski, S. Sleith, T. Belytschko, Stability of an explicit multi-time step integration algorithm for linear structural dynamics equations, Comput. Mech. 18(3) (1996) 236–244.

[69] J.H. Song, P.M.A. Areias, T. Belytschko, A method for dynamic crack and shear band propagation with phantom nodes, Int. J. Numer. Meth. Engng. 67(6) (2006) 868–893.

[70] F.V. Souza, D.H. Allen, Modeling failure of heterogeneous viscoelastic solids under dynamic/impact loading due to multiple evolving cracks using a two-way coupled multiscale model, Mech. Time-Depend. Mater. 14 (2010) 125–151.

[71] F.V. Souza, D.H. Allen, Multiscale modeling of impact on heterogeneous viscoelastic solids containing evolving microcracks, Int. J. Numer. Meth. Engng. 82 (2010) 464–504.

[72] F.V. Souza, D.H. Allen, Modeling the transition of microcracks into macrocracks in heterogeneous viscoelastic media using a two-way coupled multiscale model, Int. J. Solids. Struct. 48 (2011) 3160–3175.

[73] F.V. Souza, D.H. Allen, M.R. Kim, Multiscale model for predicting damage evolution in composites due to impact loading, Compos. Sci. Technol. 68 (2008) 2624–2634.

[74] S.S. Sternstein, L. Ongchin, A. Silverman, Inhomogeneous deformation and yielding og glasslike high polymers, Appl. Polym. Symp. 7 (1968) 175–199.

[75] P. Suquet, Local and global aspects in the mathematical theory of plasticity, Plasticity Today: Modelling, Methods and Applications (1985) 279–310.

[76] M.G.A. Tijssens, E. van der Giessen, L.J. Sluys, Modeling of crazing using a cohesive surface methodology, Mech. Mater. 32 (2000) 19–35.

[77] Z.P. Wang, C.T. Sun, Modeling micro-inertia in heterogeneous materials under dynamic loading, Wave Motion 36 (2002) 473–485.

[78] J. Yvonnet, E. Monteiro, Q. He, Computational homogenization method and reduced database model for hyperelastic heterogeneous structures, Int. J. Multiscale. Com. 11(3) (2013) 201–225.

[79] F. Zhou, J.F. Molinari, S. Tadashi, A rate-dependent cohesive model for simulating dynamic crack propagation in brittle materials, Eng. Fract. Mech. 72 (2005) 1383–1410.

Acknowledgements

The financial support provided by Netherlands Technology Foundation (STW) is gratefully acknowledged.

Foremost, I would like express my most sincere gratitude and appreciation to my supervisor Prof. Bert Sluys for giving me this wonderful opportunity to join this group and his commitment, involvement , guidance, encouragement and support during this research and all the things I learned from him.

I would also like to thank my thesis committee: Prof. Tom Scarpas, Prof. Akke S. J. Suiker Prof. Ludovic Noels, Dr. Jaap Weerheijm, Dr. Frans P. van der Meer and Dr. Varvara Kouznetsova for taking time to read my thesis and their valuable comments and suggestions.

I must express my very special thanks to Vinh Phu Nguyen who introduced me to multi-scale methods and provided me with a lot of useful documents and codes. I would also like to thank Awais Ahmed for his guidance, support and valuable discussions and collaborations on modeling polymer materials.

I would like to thank Erik Jan Lingen for his support and valuable advices in using Jem/Jive library. I would also like to thank Frank Everdij for his help and support on the computer related issues.

I specially thank Martijn van den Ende and Erik Simons who helped me translating my thesis summary into Dutch. I would also like to thank our kind and nice secretary Anneke Meijer for her help in administrative works. I would like to express my sincere gratitude to Mojtaba Talebian and Mehdi Nikbakht who have been great friends and I will never forget their help and supports when I first arrived in the Netherlands. My sincere thanks go to Mehdi Musivand Arzanfudi and Salar Mostofizadeh for being genuine friends and supportive and for all the scientific and non-scientific discussions we had in their office!. I would also like to thank my kind officemates Mohammad Latifi, Jure Zlopasa and Oriol Lloberas-Valls for their support and friendship. I thank my former and current colleagues including Angelo Simone, Rafid Al-Khoury, Zahid Shabir, Prithvi Mandapalli, Adriaan Sillem, Jitang Fan, Sanaz Saeed, Noori, Luis Magalhaes Pereira, Marcello Malagu, Ali Paknahad, Behrouz Arash, Fariborz Ghavamian, Kai Li, Jafar Amani Dashlejeh, Lars Voormeeren, Liting Qui, Mohsen Goudarzi, Nghi Le, Osvalds Verners, Prashanth Srinivasan and Tiziano Li Piani.

My special appreciation goes to my wonderful and nice neighbors and friends Vahid Kamyab and Alieh Alipour who have been genuine and supportive friends especially in difficulties. I specially thank my kind and terrific friends Hadi Jamali-Rad, Hamid Ramazani, Nader Sadeghi and Mehdi Salarpour for their friendship and all the fun we have had together. I would also like to thank all my friends Davood Karimi, Dara Ghasimi, Vahid Arbabi, Firoozeh Farokhzad, Mohi Ahmadnia, Somi Lotfi, Mostafa Zahmatkesh, Maryam Khodadadian and Fatima Anisi for

their support and friendship which made living far from homeland much easier for me.
Last but not least, I would like to express my greatest gratitude to my parents Heydar and Tayebeh, my brother Hamed, my sister Narjes and my sister-in-law Somayeh for their unconditional love and support.

Curriculum Vitæ

Amin KARAMNEJAD

02-03-1985	Born in Larestan, Iran.

Education

2003 - 2007	B.Sc. in Mechanical Engineering Faculty of Mechanical Engineering Iran University of Science and Technology Tehran, Iran
2007 - 2009	M.Sc. in Mechanical Engineering Faculty of Mechanical Engineering Iran University of Science and Technology Tehran, Iran
2011 - 2016	Ph.D. candidate Faculty of Civil Engineering and Geosciences Delft University of Technology Delft, the Netherlands

List of Publications

Journal papers

1. A. Karamnejad, V.P. Nguyen, L.J. Sluys, A multi-scale rate dependent crack model for quasi-brittle heterogeneous materials, Eng. Fract. Mech. 104 (2013) 96–113.
2. A. Karamnejad, L.J. Sluys, A dispersive multi-scale crack model for quasi-brittle heterogeneous materials under impact loading, Comput. Methods Appl. Mech. Engrg. 278 (2014) 423–444.
3. A. Karamnejad, L.J. Sluys, A multi-scale scheme for modelling fracture under dynamic loading conditions, Key Eng. Mater. 627 (2014) 37–40.
4. A. Karamnejad, L.J. Sluys, A new multi-scale scheme for modeling heterogeneous incompressible hyperelastic materials, Int. J. Numer. Meth. Engng (2015) (In press).
5. A. Karamnejad, A. Ahmed, L.J. Sluys, A numerical homogenization scheme for glass particle-toughened polymers under dynamic loading, Journal of Multiscale Modelling (2016) (In press).

Conferences

1. A. Karamnejad, V. P. Nguyen, L. J. Sluys, Multi-scale crack modeling for heterogeneous quasi-brittle materials under dynamic loading using a discontinuous homogenization scheme , Euromech 537, Paris, France, (2012).
2. A. Karamnejad, V. P. Nguyen, L. J. Sluys, A two-scale rate dependent crack model for quasi-brittle materials under dynamic loading , WCCM 2012, Sao Paulo, Brazil, (2012).
3. A. Karamnejad, V. P. Nguyen, L. J. Sluys, Modeling crack propagation in heterogeneous materials using a computational homogenization method, CFRAC 2013, Prague, Czech Republic, (2013).
4. A. Karamnejad, V. P. Nguyen, L. J. Sluys, A rate-dependent multi-scale crack model for concrete , Proceedings of the 8th International Conference on Fracture Mechanics of Concrete and Concrete Structures, Toledo, Spain, (2013) 919-929.
5. A. Karamnejad, V. P. Nguyen, L. J. Sluys, Modeling concrete under high frequency loading using a multi-scale method, Euro-C 2014, St. Anton am Arlberg, Austria, (2014).

6. A. Karamnejad, L. J. Sluys, Modeling concrete under high frequency loading using a multi-scale method , WCCM 2014, Barcelona, Spain, (2014).
7. A. Karamnejad, L. J. Sluys, Multiscale schemes for modelling fracture in soft and brittle materials under impact , CFRAC 2015, Cachan, France, (2015).
8. A. Karamnejad, L. J. Sluys, Multiscale Schemes for Modelling Impact on Soft and Brittle Materials , European Solid Mechanics Conference, Madrid, Spain, (2015).